solvent engineering for high-efficiency lead-free perovskite solar cells

---

Mahmoud Hussein

Univ.-Diss.

zur Erlangung des akademischen Grades

"doctor rerum naturalium"

(Dr. rer. nat.)

in der Wissenschaftsdisziplin " physikalische Chemie"

eingereicht an der

Mathematisch-Naturwissenschaftlichen Fakultät

Institut für Chemie

der Universität Potsdam

und

Helmholtz-zentrum Berlin für Materialien und Energie

Ort und Tag der Disputation: Potsdam, den 01.02.2024

Hauptbetreuer: Prof. Dr. Antonio Abate
Prof. Dr. AndreasTaubert

Betreuer: Dr. Titan Hartono

Reviewers: Prof. Dr. Dieter Neher

Published online on the
Publication Server of the University of Potsdam:
https://doi.org/10.25932/publishup-63037
https://nbn-resolving.org/urn:nbn:de:kobv:517-opus4-630375

Abstract

Tin is one of the most promising alternatives to lead to make lead-free halide perovskites for optoelectronics. However, the stability of tin-based perovskites is hindered by the oxidation of Sn(II) to Sn(IV). Recent works established that dimethylsulfoxide, which is one of the best performing solvents for processing perovskite, is the primary source of tin oxidation. The quest for a stable solvent could be the gamechanger in the stability of tin-based perovskites. Starting from a database of over 2000 solvents, we identified a series of 12 new solvents suitable for the processing of formamidinium tin iodide perovskite (FASnI3) experimentally by investigating 1) the solubility of the precursor chemicals FAI and SnI_2, 2) the thermal stability of the precursor solution and 3) the possibility to form perovskite. Finally, we demonstrate a new solvent system to produce solar cells outperforming those based on DMSO. Our work provides guidelines for further identification of new solvents or solvent mixtures for preparing stable tin-based perovskites.

Precisely regulating the crystallization of perovskite precursor within a thin film is crucial for efficient solar cell efficiency and production. The deposition of tin-based perovskite films from a solution poses challenges due to the rapid crystallization of tin compared to the commonly used lead perovskite. The most effective method to achieve high efficiencies involves depositing perovskite from dimethyl sulfoxide (DMSO), which hinders the rapid assembly of the tin-iodine network responsible for perovskite formation. However, this approach has a drawback, as dimethyl sulfoxide causes tin oxidation during processing. This study introduces a promising alternative where 4-(tert-butyl) pyridine can replace dimethyl sulfoxide in controlling crystallization without inducing tin oxidation. Perovskite films deposited from pyridine demonstrate a significantly lower defect density, leading to enhanced charge mobility and improved photovoltaic performance, making it a favorable choice for tin perovskite film deposition.

Tin perovskites have emerged as a highly promising environmentally sustainable substitute for lead perovskites, primarily owing to their superior optoelectronic characteristics and reduced bioavailability. Nevertheless, there are several reasons why the performance of tin perovskites cannot be compared to lead perovskites. One such reason is the energy band mismatch between the perovskite absorber film and the charge transporting layers (CTLs). Nevertheless, the band diagrams presented in the existing literature exhibit inconsistencies, thereby leading to a lack of consensus. Furthermore, the understanding of the dynamics associated with charge extraction remains inadequate. This study aims to determine the energy band positions of tin perovskites through the utilization of kelvin probe (KP) and Photoelectron yield spectroscopy (PYS) techniques. The objective is to establish an accurate band diagram for the commonly employed device stack. Furthermore, we conduct a diagnosis of the energetic deficiencies present in the existing energetic framework of tin halide perovskites. We aim to elucidate BCP's impact

on the enhancement of electron extraction in C_{60}/BCP systems, focusing on the energetic aspects. In addition, we employed transient surface photovoltage (tr-SPV) to gain insights into the charge extraction kinetics of commonly reported CTLs, including NiOx and PEDOT as hole transport layers (HTLs), and C_{60}, ICBA, and PCBM as electron transport layers (ETLs). In this Chapter, we employ the hall effect, KP, and TRPL techniques to determine the precise p-doping concentration in $FASnI_3$. Our findings consistently revealed a value of $1.5 * 10^{17}$ cm^{-3}. The results of our study demonstrate the necessity of independently developing the charge extraction layers of tin halide perovskites, independently from lead perovskites.

Kurzfassung

Zinn ist eine der vielversprechendsten Alternativen zu Blei, um bleifreie Halogenidperowskite für die Optoelektronik herzustellen. Die Stabilität von Perowskiten auf Zinnbasis wird jedoch durch die Oxidation von Sn(II) zu Sn(IV) beeinträchtigt. Jüngste Arbeiten haben ergeben, dass Dimethylsulfoxid, eines der besten Lösungsmittel für die Verarbeitung von Perowskiten, die Hauptquelle für die Oxidation von Zinn ist. Die Suche nach einem stabilen Lösungsmittel könnte den Ausschlag für die Stabilität von Perowskiten auf Zinnbasis geben. Ausgehend von einer Datenbank mit über 2000 Lösungsmitteln haben wir eine Reihe von 12 neuen Lösungsmitteln identifiziert, die für die Verarbeitung von Formamidinium-Zinniodid-Perowskit ($FASnI_3$) geeignet sind, indem wir 1) die Löslichkeit der Vorläuferchemikalien FAI und SnI_2, 2) die thermische Stabilität der Vorläuferlösung und 3) die Möglichkeit zur Bildung von Perowskit experimentell untersucht haben. Schließlich demonstrieren wir ein neues Lösungsmittelsystem zur Herstellung von Solarzellen, das die auf DMSO basierenden Zellen übertrifft. Unsere Arbeit liefert Leitlinien für die weitere Identifizierung neuer Lösungsmittel oder Lösungsmittelmischungen zur Herstellung stabiler Perowskite auf Zinnbasis.

Die genaue Steuerung der Kristallisation des Perowskit-Vorläufers in einer Dünnschicht ist entscheidend für die Effizienz und Produktion von Solarzellen. Die Abscheidung von Perowskit-Filmen auf Zinnbasis aus einer Lösung stellt aufgrund der schnellen Kristallisation von Zinn im Vergleich zu dem üblicherweise verwendeten Bleiperowskit eine Herausforderung dar. Die effektivste Methode zur Erzielung hoher Wirkungsgrade ist die Abscheidung von Perowskit aus Dimethylsulfoxid (DMSO), das den schnellen Aufbau des für die Perowskitbildung verantwortlichen Zinn-Jod-Netzwerks behindert. Dieser Ansatz hat jedoch einen Nachteil, da Dimethylsulfoxid während der Verarbeitung eine Zinnoxidation verursacht. In dieser Studie wird eine vielversprechende Alternative vorgestellt, bei der 4-(tert-Butyl)-pyridin Dimethylsulfoxid bei der Steuerung der Kristallisation ersetzen kann, ohne eine Zinnoxidation zu verursachen. Aus Pyridin abgeschiedene Perowskit-Filme weisen eine deutlich geringere Defektdichte auf, was zu einer erhöhten Ladungsbeweglichkeit und einer verbesserten photovoltaischen Leistung führt und es zu einer günstigen Wahl für die Abscheidung von Zinn-Perowskit-Filmen macht.

Zinnperowskite haben sich als vielversprechender, umweltverträglicher Ersatz für Bleiperowskite erwiesen, vor allem wegen ihrer besseren optoelektronischen Eigenschaften und ihrer geringeren Bioverfügbarkeit. Dennoch gibt es mehrere Gründe, warum die Leistung von Zinnperowskiten nicht mit der von Bleiperowskiten verglichen werden kann. Einer dieser Gründe ist die Nichtübereinstimmung der Energiebänder zwischen dem Perowskit-Absorberfilm und den ladungstransportierenden Schichten

(CTLs). Die in der vorhandenen Literatur dargestellten Banddiagramme sind jedoch uneinheitlich, was zu einem Mangel an Konsens führt. Außerdem ist das Verständnis der mit der Ladungsextraktion verbundenen Dynamik noch unzureichend. In dieser Studie sollen die Energiebandpositionen von Zinnperowskiten mit Hilfe der Kelvinsonde (KP) und der Photoelektronenausbeutespektroskopie (PYS) bestimmt werden. Ziel ist es, ein genaues Banddiagramm für den üblicherweise verwendeten Bauelementestapel zu erstellen. Darüber hinaus führen wir eine Diagnose der energetischen Unzulänglichkeiten durch, die im bestehenden energetischen Rahmen von Zinnhalogenid-Perowskiten vorhanden sind. Unser Ziel ist es, Folgendes zu klären den Einfluss von BCP auf die Verbesserung der Elektronenextraktion in C_{60}/BCP-Systemen, wobei der Schwerpunkt auf den energetischen Aspekten liegt. Darüber hinaus haben wir die transiente Oberflächenphotospannung (tr-SPV) eingesetzt, um Einblicke in die Ladungsextraktionskinetik von allgemein bekannten CTLs zu gewinnen, einschließlich NiOx und PEDOT als Lochtransportschichten (HTLs) und C_{60}, ICBA und PCBM als Elektronentransportschichten (ETLs). In diesem Kapitel verwenden wir den Halleffekt, KP- und TRPL-Techniken, um die genaue p-Dotierungskonzentration in $FASnI_3$ zu bestimmen. Unsere Ergebnisse ergaben durchweg einen Wert von $1.5 * 10^{17}$ cm^{-3}. Die Ergebnisse unserer Studie zeigen, dass es notwendig ist, die Ladungsextraktionsschichten von Zinnhalogenidperowskiten unabhängig von den Bleiperowskiten zu entwickeln.

List of abbreviations

PSC	Perovskite solar cell	ELA	Energy level alignment
THP	Tin halide perovskite	TCO	Transparent conductive oxide
PCE	Power conversion efficiency	E_g	band gap
CTL	Charge transport layer	DSSC	dye-sensitized solar cell
NP	Nano Particle		
SEM	Scanning electron microscopy		
FWHH	Full width at half height		
KP	Kelvin Probe		
PYS	photoelectron yield spectroscopy		
HTL	Hole Transport Layer		
ETL	Electron Transport Layer		
CBM	conduction band minimum		
VBM	valence band maximum		
PL	photoluminescence		
WF	work function		
E_i	Ionization potential		
E_{vac}	Vacuum level		
E_F	Fermi level		
LED	Light emitting diode		
QD	Quantum Dot		

1. Introduction:

1.1 The big picture: Fighting against climate change

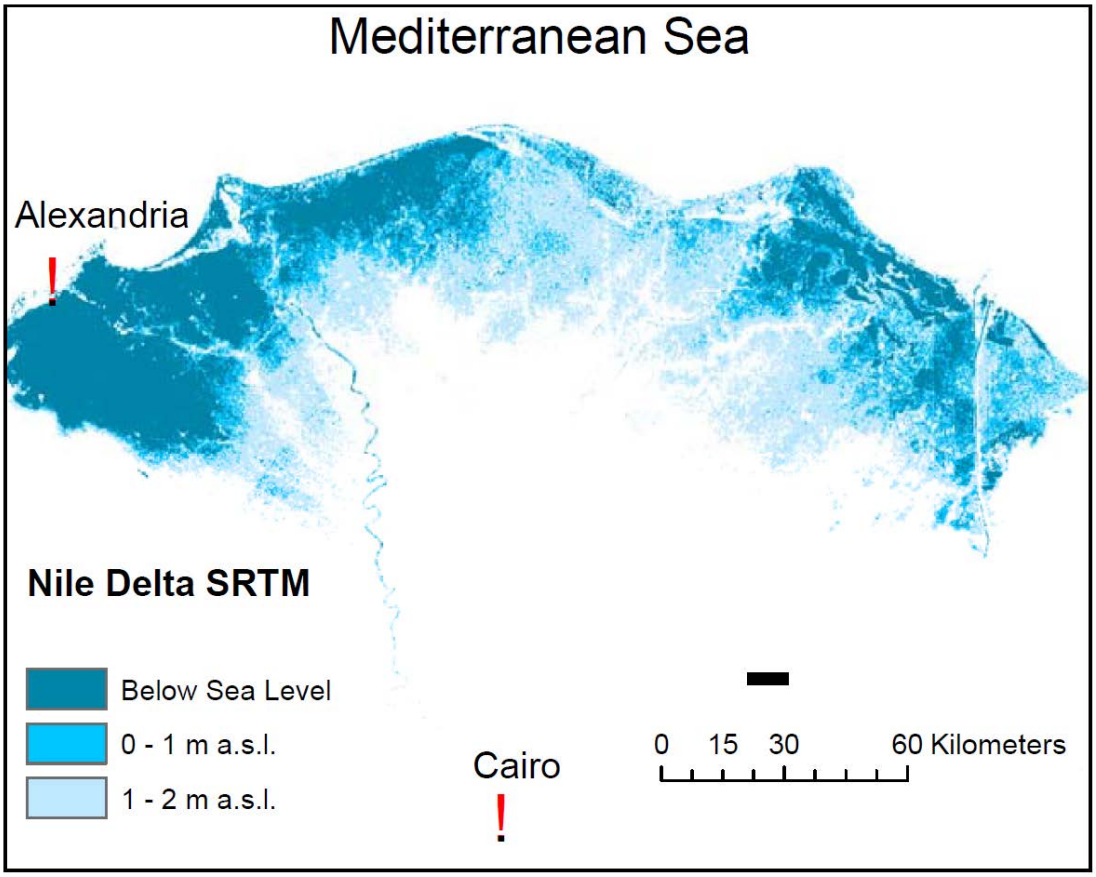

Figure 1: The possible impact of seal level rise on the Egyptian Nile delta. Light blue areas will be the new costs while the deep blue areas will be totally submerged under the Mediterranean[1].

The rising sea levels due to global warming and climate change is expected to flood thousands of square kilometers in the Nile Delta at the very north of Egypt[2]. This will lead to an immigration wave inside Egypt for more than 30 million citizens and will immensely harm the Egyptian economy. The potential consequences will pose a significant threat to agricultural land and property in the Nile Delta region. Elevated temperatures can potentially diminish agricultural productivity, a circumstance that diminished water resources can exacerbate. Consequently, the escalation of unemployment and food prices poses a potential threat of exacerbating malnutrition rates. The escalation of particulate matter and heat stress in Cairo has the potential to have detrimental effects on human health, resulting in a significant number of fatalities valued at a substantial economic cost of tens of billions of Egyptian pounds annually[1]. It is projected that there will be a decline in annual tourist revenues. The projected aggregate financial losses for the aforementioned sectors are anticipated to range between approximately 200 to 350 billion

Egyptian pounds (EGP; equivalent to US $36-64 billion). This estimate represents a proportion of 2-6% of the anticipated future gross domestic product[3].

At the same time, Egypt is one of the sunniest countries in the world. It possesses a high capacity for solar energy, a vital factor in fighting global warming. For example, Cairo receives an average of 3450 hours of annual sunshine. For comparison, Berlin has 1712 hours of sunshine/year. This contradictory situation motivated us to work to fight climate change by reducing greenhouse gas (GHGs) emissions. The energy sector is one of the main contributors to GHGs globally, so if we could increase the resilience on solar cells for energy generation, we would decrease the GHGs to the extent that keep global warming at bearable limits[4].

Climate change has become a prominent and pressing issue in contemporary times, exerting a transformative influence on the Earth's climate system and yielding substantial and enduring consequences. Climate change is characterized by enduring alterations in weather patterns, temperatures, and climatic conditions that occur worldwide. Although climate has been influenced by natural factors over the course of Earth's history, it is widely recognized that human activity is the primary catalyst for contemporary climate change. The combustion of fossil fuels, the clearing of forests, and diverse industrial activities contribute to the emission of greenhouse gases (GHGs) into the Earth's atmosphere, amplifying the greenhouse effect and resulting in global warming. The increase in temperatures associated with climate change has been observed to significantly impact ecosystems, leading to disruptions in their functioning. Furthermore, climate change has been found to induce alterations in weather patterns, thereby affecting the regularity and intensity of various meteorological phenomena. These changes in ecosystems and weather patterns have been identified as having substantial economic implications, resulting in severe consequences for various sectors of the economy. Nevertheless, through the implementation of collective efforts and the adoption of comprehensive strategies, humankind has the capacity to effectively tackle the climate crisis and construct a sustainable future that can endure for future generations.

Although natural factors have played a role in historical climate fluctuations, it is widely acknowledged that the contemporary era of climate change is predominantly influenced by human activities, particularly since the commencement of the Industrial Revolution. The combustion of fossil fuels, such as coal, oil, and natural gas, for the purpose of energy generation, transportation, and industrial activities, results in the emission of significant quantities of carbon dioxide (CO_2) into the Earth's atmosphere. CO_2 is a significant greenhouse gas that effectively absorbs and retains solar radiation, thereby intensifying the greenhouse effect and ultimately resulting in the phenomenon of global warming.

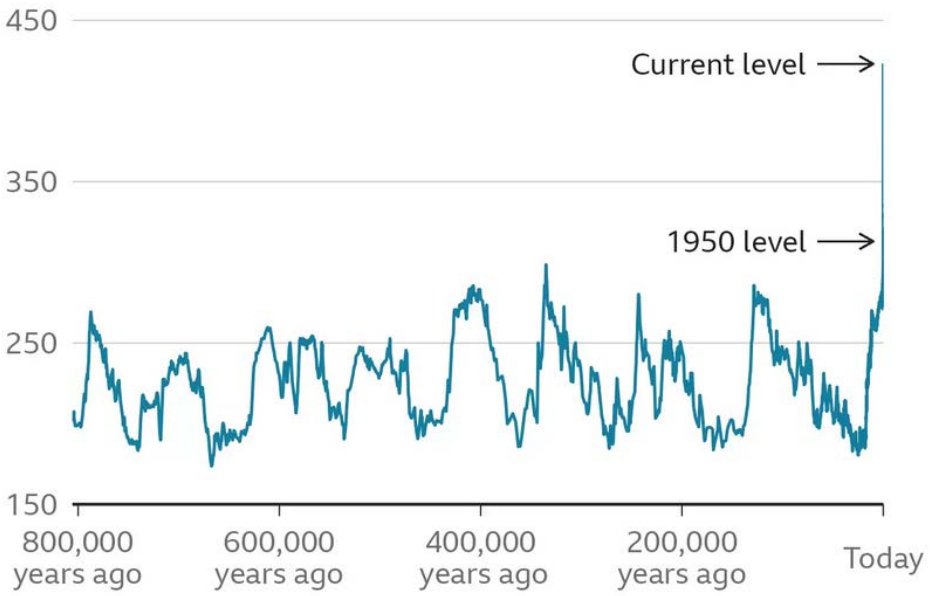

Figure 1.2: Carbon dioxide levels in the atmosphere since 800,000 years as recorded from ancient fossil samples[5].

The global impacts of climate change are observable, influencing diverse facets of the natural environment and human society. The increase in temperatures is a prominent outcome of the phenomenon known as global warming. The frequency and intensity of heatwaves and extreme weather events, including hurricanes, droughts, floods, and wildfires, are observed to escalate in tandem with the Earth's rising average surface temperature. The melting of polar ice caps and glaciers is regarded as one of the most alarming repercussions of global warming. Increasing temperatures have led to a significant reduction in the ice cover in polar regions, namely Greenland and Antarctica, resulting in a notable elevation of sea levels. The aforementioned phenomenon presents a substantial peril to coastal communities and regions situated at low altitudes, resulting in the occurrence of flooding, coastal erosion, and the displacement of a considerable number of individuals.

The increase in ocean temperatures is an additional outcome of climate change. As the Earth's atmosphere experiences an increase in temperature, the resulting heat is transferred to the Earth's oceans, thereby inducing thermal expansion. The process of expansion discussed herein has been found to significantly impact the increase in sea levels, as well as exerting notable effects on various marine ecosystems. The process of ocean acidification, resulting from the uptake of CO_2 from the atmosphere, poses significant harm to marine ecosystems, with particular implications for coral reefs and organisms that rely on shell formation. The impacts of climate change extend to ecosystems and biodiversity as

well. Numerous plant and animal species encounter challenges in their ability to acclimate to the swiftly evolving climate, resulting in alterations to their geographical range and migration patterns. Certain species are at risk of extinction due to their limited capacity to adapt to shifting environmental conditions. This susceptibility can potentially disrupt entire ecosystems and create imbalances within natural communities. In conjunction with its ecological consequences, climate change substantially impacts human well-being. Extreme heat waves have the potential to give rise to heat-related ailments and fatalities. In contrast, alterations in weather patterns can exert an influence on the transmission of infectious diseases such as malaria and dengue fever. The adverse effects of air pollution on respiratory and cardiovascular health are further intensified in urban regions, primarily due to the amplifying impact of elevated temperatures.

In order to mitigate the effects of climate change, it is imperative to prioritize expanding renewable energy production, with a specific emphasis on solar energy. Solar energy, which is captured by means of photovoltaic cells, presents a multitude of benefits. The resource in question is both renewable and abundant, and it exhibits minimal greenhouse gas emissions during its operational phase. Solar panels can be installed in diverse locations, facilitating the decentralization of energy generation.

The case of the Nile´s delta in Egypt serves as a limited illustration of the consequences of the persistent climate change, while more severe occurrences are presently unfolding globally. The phenomenon of glacier melting, forest fires, and the collapse of ocean currents is observed in contemporary times. The publication of the new assessment report by the Intergovernmental Panel on Climate Change (IPCC), the United Nations' authoritative body responsible for evaluating climate change, occurred on August 9th, 2021[6]. The findings are not unexpected, yet they evoke a sense of apprehension, and convey a distinct message: anthropogenic activities have caused a rise in global temperatures, resulting in unparalleled alterations to the Earth's climate. There remains a viable possibility of constraining global warming to a maximum of 1.5 °C. However, in order to achieve this objective, it is imperative to promptly initiate substantial and extensive reductions in greenhouse gas emissions. The upcoming United Nations Climate Change Conference is scheduled to be held in November in the city of Glasgow. In light of the recent IPCC report, there is a need to re-evaluate the objectives of the Paris Agreement in order to strengthen the endeavors to combat global warming and ensure the attainment of the net-zero2 target by the year 2050[7].

It is evident that in the present circumstances, the research pertaining to the advancement of renewable energies holds heightened significance. At present, hydroelectric, wind, photovoltaic, and bioenergy are the primary sources of environmentally friendly power, collectively accounting for only 25% of electricity generation. In order to maintain the global temperature, increase below 1.5 °C, it is imperative to achieve a near-total elimination of carbon emissions from the electricity industry by the year 2050. The objective is to increase the existing generation capacity of renewable power from 2800 GW to more

than 27700 GW within the next three decades. This expansion aims to ensure that renewable energy sources contribute to 90% of the total electricity demand, while the remaining 10% is shared between natural gas and nuclear power. Wind and solar energy is anticipated to assume a prominent role within this context, accounting for 63% of the aggregate electricity demands[8].

Currently, the majority (95%) of photovoltaic energy is generated using crystalline silicon (Si) solar modules. These modules have the capability to achieve efficiencies of up to 24.4%3 and are certified to maintain stability for a period exceeding 25 years[9]. However, despite its notable achievements, silicon (Si) is not considered an optimal candidate for light absorption due to its low absorption coefficient, indirect bandgap, and the necessity for high-temperature manufacturing processes. Consequently, there is a current shift in research focus towards alternative semiconductors, particularly thin-film solar cells. The nomenclature inherently emphasizes a distinguishing characteristic of these solar cells, namely their diminished thickness compared to silicon counterparts, measuring only a few micrometers instead of hundreds of micrometers. This particular characteristic is intriguing as it enables the broadening of applications for such devices. For instance, it facilitates the creation of lightweight and flexible modules that can be seamlessly incorporated into architectural structures or utilized within the Internet of Things (IoT) framework. Thin-film solar cells encompass various materials, such as cadmium telluride (CdTe), copper indium gallium selenide (CIGS), organic semiconductors or dyes, and halide perovskites. The latter has garnered significant interest from the scientific community in the past decade, emerging as a highly promising alternative to silicon solar cells[10].

1.2 Halide perovskite solar cells – a concise overview

Perovskite solar cells (PSCs) represent a promising and relatively new technology in the field of photovoltaics. They are named after the perovskite crystal structure, which was first described by German mineralogist Gustav Rose in 1839. Perovskite solar cells have attracted significant attention due to their high efficiency, low-cost materials, and ease of fabrication. The perovskite crystal structure was first identified in the mineral perovskite (calcium titanium oxide) in the Ural Mountains of Russia. The structure is characterized by a cubic arrangement of metal cations surrounded by oxygen anions in the chemical formula ABX_3 where A represents a monovalent cation, B represents a divalent metal, and X represents a monovalent anion. As long as the structure is not compromised in any way, the sites are free to be inhabited by a wide variety of atoms and molecules. This is something that is governed by a quantity known as the Goldschmidt tolerance factor, and it is dependent on the size of the ions. For instance, A is frequently methylammonium (MA^+), formamidinium (FA^+), or cesium (Cs^+), B is typically lead or tin, and X is a halide, most frequently iodine, bromine, or chlorine. It is mostly dependent on the energy levels of the metal and halide ions, whereas the A cation has orbitals with energies that are deeper inside

the bands. The electronic structure is dictated by the choice of ions that form the ABX_3 structure. Because there are so many different ways that A, B, and X may be combined, the bandgaps that can be achieved span a wide range—approximately 1.2 eV to 3.5 eV. As a result, perovskites are an exceptionally diverse family of materials, both in terms of their optoelectronic capabilities and their stoichiometry[11].

The perovskite material family started gaining interest in the scientific community for its potential applications in various fields, including solar cells, photodetectors, quantum dots (QDs), and light emitting diodes (LEDs)[12]. The first report on the use of perovskite materials in photovoltaic applications was published by Tsutomu Miyasaka and his team. They demonstrated a perovskite-based solar cell with a structure similar to dye-sensitized solar cells (DSSCs). Over the next few years, researchers continued to refine the PSCs design, leading to rapid efficiency improvements. The efficiency of PSCs increased from around 3-4% in 2009 [13] to over 26% in 2023[14], making them comparable to established solar cell technologies like silicon-based solar cells and thin-film solar cells. PSCs witnessed an explosion in research and development activities globally. Researchers explored various materials, device architectures, and fabrication methods to improve efficiency, stability, and scalability.

The popularity of perovskite-based devices can be attributed to their combination of direct and configurable bandgap, high absorption coefficient, and long diffusion length with low-cost and simple production processes[15]. While each of these characteristics is seen in semiconductors before, they have never before been combined into a single class of material. The perovskite ionic nature, the huge lattice constant, and the anti-bonding interaction between Pb s orbitals and I p orbitals are the origins of these characteristics[16]. Some of the perovskite defects have very low energy levels, meaning their energy is very near to the band edges. Trapped charges can quickly escape if thermally or optically aroused, making these flaws harmless. As a result, perovskite is often understood to be defect-tolerant, and PSCs are able to achieve high efficiencies despite the presence of a significant number of defects[17]. However, ion migration is a major cause of losses in perovskite solar cells, and this is also due to the perovskite's ionic composition[18]. Light and bias cause the perovskite material's highly mobile ions to travel through the device, where they deposit faults and build up at interfaces. This leads to increased hysteresis and other phenomena associated with non-radiative recombination.

1.3 Motivation and Thesis Outline

Perovskite solar cells should go lead free

Despite the photovoltaic ultrperformance of lead perovskites, it still faces two main challenges to be commercialized: stability and lead toxicity. The later challenge arose from the toxicity and the bio availability of lead. To market adoption of PSCs could be slowed down or, in the worst-case scenario, completely inhibited. The toxicity of lead and the ease with which it may seep into the environment, which is referred to as its bioavailability[19,20], are two possible concerns that might constitute a threat to the environment in the event that the cell ruptures or cleaves. Given the circumstances, due to the

structural similarity between the two elements[21], it would seem that tin would be the most logical replacement for lead. Despite this, the efficiency of THPs, which show the maximum performance, is only about 14%, which is 10% lower than their lead equivalents. This is because THPs have a more complex structure. Additionally, the stability and repeatability of these THPs is much worse to that of their competitors. It has been determined that the misalignment of energy bands is a significant component that contributes to this regression[22].

The concentration of lead in the presently operational PSCs is below the threshold established by all countries that enforce regulations on heavy metal usage in electronic devices. As an illustration, the European Union abides by the "Directive on the restriction of the use of certain hazardous substances in electrical and electronic equipment," commonly referred to as RoHS1, enacted in 2003, and its subsequent iteration RoHS2, established in 2011. These directives are commonly known as the "lead-free directives."[23]. The Restriction of Hazardous Substances (RoHS) directive incorporates contemporary knowledge regarding the prolonged hazards linked to persistent exposure to low concentrations of toxic heavy metals[24]. More precisely, it imposes a limitation of 0.1% by weight on the highest permissible level of lead in every uniform substance present in electronic devices, such as the perovskite material found in a PSCs. Regrettably, all the halide perovskites that have been hitherto showcased as efficacious photovoltaic materials exhibit a lead content exceeding 10% by weight.

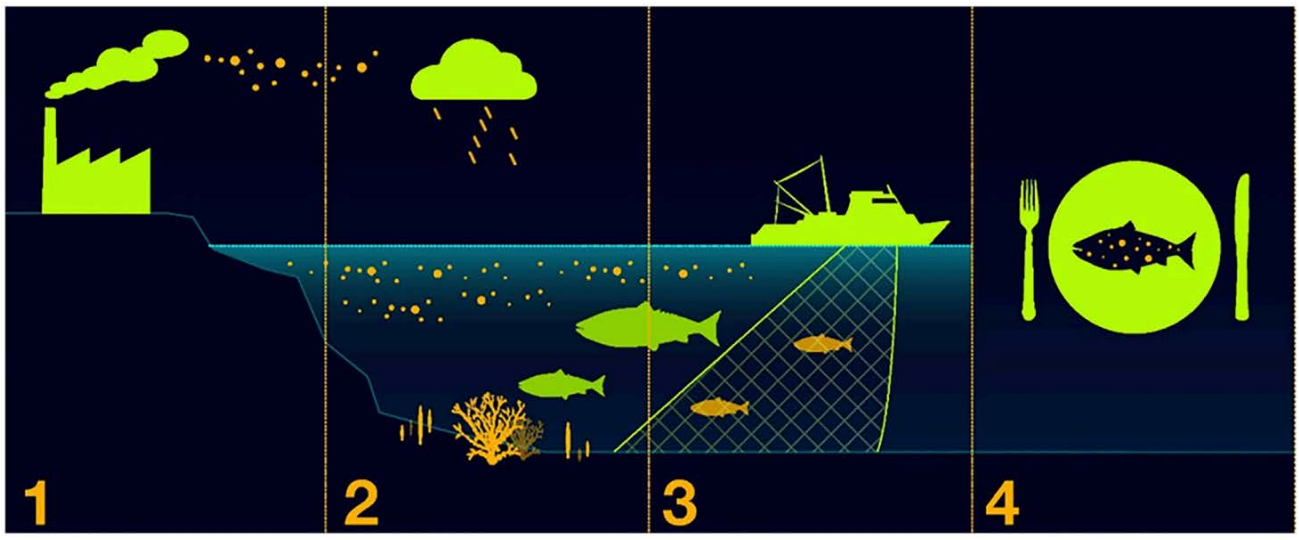

Figure 1.3: (1) Metals get into the world because of industrial activities. (2) Metals are carried by water into plants, which small fish eat. (3) Bigger fish eat small fish that are dirty. (4) People eat fish that has been tainted. Heavy metals build up as they move up the food chain. Because of this, humans have more heavy metals than any other species lower on the chain. US Environmental Protection Agency is the source. Copyright © 2017 Wily.

Based on the regulations outlined in the RoHS, the substantial presence of cadmium in CdTe should likewise render it ineligible for inclusion within the European energy market. Nevertheless, CdTe, like

other solar cell technologies, enjoys an exemption from the RoHS directive, which is scheduled for reevaluation in 2018. The potential expansion of this exemption could potentially render PSCs eligible for the market. However, this prospect appears unwise due to the significantly greater water solubility exhibited by lead halide perovskites in comparison to CdTe[25]. The effective risk of toxicity of a chemical is influenced by numerous factors, among which the solubility in water stands out as particularly hazardous. When lead halide perovskites come into contact with water or humid air, they undergo a reaction that results in the formation of water-soluble lead compounds. These compounds have the potential to gradually accumulate within the food chain and ultimately enter the human body. This process is illustrated in Figure 1.3. Numerous comprehensive investigations have extensively documented the profound and detrimental consequences, particularly on the well-being of children, resulting from the accumulation of merely a few micrograms of heavy metals within the human body[26]. Consequently, we have comprehensively examined all potential risks pertaining to lead contamination, surpassing both regulatory requirements and economic considerations. By implementing a meticulous design of the PSC life cycle, the potential for lead contamination can be mitigated. However, our overarching objective is to achieve a definitive resolution by completely eradicating lead from PSCs.

1.4 Thesis Structure:

Part I provides a background overview necessary to understand the studies presented in this thesis. Particularly, Chapter 2 which provides fundamental knowledge about the solvation process of perovskite precursors. It explains the basic theory of perovskite solvation, solvent interaction, and nucleation. Moreover, it illustrates the mechanism of antisolvent crystallization. Chapter 3 explains the fundamentals charge transport layers in perovskite solar cells, including the differences between the energetic landscape of tin and lead perovskites. In addition, it illustrates the basics of band alignment in perovskite solar cells. Chapter 4 explains the methods behind samples preparation and the theories behind characterization techniques used in our thesis.

Part II presents the results obtained through my doctoral research and the corresponding interpretations as follows:

Chapter 5 shows new potential solvents to replace DMSO after it was found to oxidize Sn^{2+} to Sn^{4+}. In this study, we scanned over 2000 solvents, filtered them then screened over 80 molecules in the lab and found 12 solvents are able to form 1M solution of FASnI3. Moreover, the study verified the thermal stability of such solvents in addition to the chemical safety to Sn^{2+}, i.e., not oxidizing Sn^{2+} to Sn^{4+}. Finally, we demonstrate the ability of the working solvents to form a perovskite film, and we show a tin perovskite FASnI3 device with a PCE of 6.2%, while the perovskite film was deposited from a solvent mixture DMF:DMPU (6:1).

Chapter 6 shows a viable approach to enhance the crystallization dynamics of DMSO-free tin perovskite devices by the addition of 4-(*tert*-butyl) pyridine as a co-crystallization additive. It explains the mechanism of action of tBP additive which forms a stable complex with tin halide then it controls the crystallization dynamics including nucleation and growth. As a result, tBP produced a pinhole-free $FASnI_3$ films with high-quality microstructure. This chapter demonstrates that tBP can replace DMSO without oxidizing Sn^{2+} as it formed a device with a PCE of over 7%, it has also one order of magnitude less defect density compared to DMSO. This open doors to engineer the coordination between the solvent and the perovskite porecursor through additives with coordination abilities such as lewis acids and lewis basis.

Chapter 7 introduces a detailed study of the energetics situation of tin perovskites. It starts with an accurate measurement of the hole concentration in $FASnI_3$ which was found to $1.5 *10^{17}$. This result was confirmed by three different techniques KP, TRPL, and Hall effect. After that it provides a detailed investigation of the energy band positions of $FASnI_3$ and the most widely used CTLs such as ICBA, PCBM, C_{60}, BCP, PEDOT, and NiOx. This investigation uncovers the energetic deformation in tin perovskites. In addition, it illustrates the accurate role of BCP in enhancing charge extraction. Later, Chapter 7 provides an investigation of the charge extraction dynamics in tin perovskites supported with a theortical modelling for the extraction trends of electrons and holes which then helps to quantify the different loss mechanisms in tin perovskites.

2. Basic principles of perovskite solar cells.

2.1 Historical overview:

The efficiency of PSCs has experienced a significant enhancement, rising from 3% in 2009 to around 26% in the current period[14]. The first considerable advancement in functional perovskite-based solar cells was documented in a publication in 2009. This study demonstrated an efficiency of 3.8% by utilizing the $CH_3NH_3PbI_3$ perovskite material[13]. In this seminal study conducted by Kojima et al., the utilization of perovskites as a sensitizer in a device resembling a dye-sensitized solar cell (DSSC) was successfully proven[27]. In this representation, the perovskite material serves as a pigment that is adsorbed onto the surface of the mesoporous TiO_2[28] , in which a marginal increase in efficiency of 6.5% was seen during the subsequent two-year period. Nevertheless, this device's structural integrity was impaired due to the dissolving of the perovskite material in the liquid electrolyte configuration resembling a DSSC.

In 2012, a notable advancement was made by Lee et al. when they applied solid-state hole selective contacts instead of liquid electrolytes, leading to an efficiency surpassing 9%[29]. This transition was a pivotal moment in the improvement of stability and performance. Following that, there have been significant breakthroughs in the efficiency of PSCs. For example, Heo et al., developed a range of polymeric hole selective connections in $CH_3NH_3PbI_3$, resulting in a notable enhancement in the device's efficiency to 12%[30]. Burschka et al. produced an additional breakthrough by implementing a two-step strategy to modify the deposition procedure of the perovskite layer. This modification resulted in an impressive efficiency of 15.0%[31]. In the study published by Liu et al., an alternate deposition process using physical vapor deposition was investigated, resulting in an efficiency of 15.4%[32]. Furthermore, Zhou et al., demonstrated an improvement in the electrical conductivity of TiO_2 by using yttrium (Y) as a dopant. This enhancement significantly increased the efficiency of planar-structured PSCs, reaching a remarkable value of 19.3%[33]. In addition, Yang et al. successfully attained a certified efficiency of 20.2% in their study by employing intermolecular exchange for $FAPbI_3$-based PSCs[34]. Saliba et al. reported significant advancements in enhancing efficiency, achieving a notable efficiency of 21.6%, by employing a quadruple cation perovskite system[35]. In their continuous research endeavors, Yang et al. have documented a verified efficiency of 22.1% by proficient management of iodide inside a double cation perovskite system[34]. The latest developments in this field have demonstrated remarkable progress, as evidenced by achieving a peak efficiency of 26%. According to a report by NREL, this accomplishment exceeds the efficiency of multicrystalline silicon solar cells and matches that of monocrystalline silicon wafers. The achievements above underscore the significant advancements in PSCs technology, demonstrating its considerable promise as a prominent photovoltaic challenge.

2.2 Device Architecture of perovskite solar cells

The architectural aspects of the devices encompass the careful consideration of materials used for charge separation, the methodologies applied in the manufacturing process, and the compatibility of each constituent component. Generally, two main architectural designs are formulated for PSCs: mesoporous and planar-structured PSCs. Currently, the most significant recorded efficiency is 26.1% for planar structured PSCs[14], whereas planar structured PSCs have attained an efficiency of 20.8%[36]. In addition, PSCs may be classified into two structures, "n-i-p" and "p-i-n," based on the direction of electron transport within these devices.

In the context of "n-i-p" structured PSCs, the flow of electrons occurs from the perovskite layer towards the underlying electron-selective contact. Eventually, these electrons are gathered at the ETL. In contrast, in PSCs with a "p-i-n" structure, electrons move from the perovskite layer towards the top ETL, ultimately accumulating at the metal contact. Using several architectural strategies in perovskite solar cells contributes to their adaptability and potential for enhancing efficiency.

2.2.1 Mesoporous regular nip structure:

The mesoporous structured "n-i-p" PSCs are composed of many components, including a transparent conductive oxide, an ETL, the active perovskite layer, an HTL, and a metal contact electrode, as seen in Figure 2.1. In contrast to the configuration of planar structured PSCs, mesoporous structured PSCs have an extra layer of mesoporous inorganic material positioned on top of the planar ETL. In addition to the utilization of TiO_2 nanoparticles, many alternative configurations of TiO_2 nanocrystals, including nanorods, nanowires, nanofibers, nanoflowers, and nanocones, have been employed in previous studies[37,38]. Additional inorganic minerals that are utilized include Fe_2O_3[39], ZrO_2[40], SiO_2[41], and Zn_2SnO_4[42].

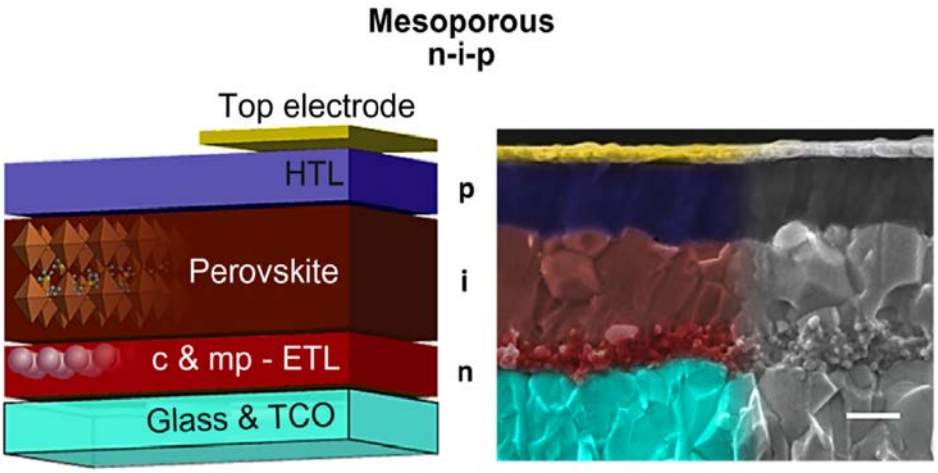

Figure 2.1. Schematic structure of mesoporous regular n-i-p structure (left). Cross-sectional Sem image of the same device architecture[43]. Copyright © 2019 Elsevier.

2.2.2 Planar perovskite structure:

The absence of a mesoporous inorganic layer does not always hinder attaining high PCE in perovskite solar cells (PSCs), owing to the advantageous charge transport properties and elevated absorption coefficient shown by halide perovskites. Indeed, a very effective architectural design known as planar structured PSCs was developed. Planar PSCs have similarities with mesoporous structured PSCs, as they both comprise key components, including a transparent conductive electrode, an active perovskite layer, an HTL, an ETL, and the top metal electrode. The primary differentiation between planar-structured PSCs and mesoporous-structured PSCs pertain to their inherent structures, which may be classified as either "n-i-p" or "p-i-n." The electron flow direction in the "n-i-p" structure is analogous to that observed in DSSCs, giving rise to its alternative designation as regular structured PSCs. In contrast, the "p-i-n" structure exhibits an electron flow direction analogous to that observed in organic photovoltaics, leading to its designation as inverted structured PSCs.

2.2.3 Regular Planar nip structure:

The regular planar structure, referred to as the "n-i-p" configuration, as seen in Figure 2.3, demonstrates a coherent advancement from the mesoscopic arrangement. In the experimental configuration, incident light initially traverses the ETL to access the perovskite layer. By implementing meticulous regulation of the perovskite absorber production and optimizing the interface between the perovskite and CTLs, remarkable levels of efficiency may now be achieved without needing a mesoporous electron selective layer. Although these PSCs offer significant efficiency, they frequently exhibit pronounced hysteresis in their JV characteristics. Concurrently, organic HTLs face obstacles due to their elevated expenses, constraining the economic feasibility of PSCs. In general, the electrochemical supercapacitor electrodes (ESLs) consist of dense layers of metal oxides with n-type conductivity, such as SnO_2[44] and TiO_2[33]. Two frequently utilized HTLs in the field are Spiro-OMeTAD and poly [bis(4-phenyl)(2,4,6-trimethylphenyl)amine] (PTAA)[45]. Additional high-surface-area light absorbers, such as cuprous thiocyanate (CuSCN) [46] and CuI[47], have exhibited notable efficacy in the context of PSCs.

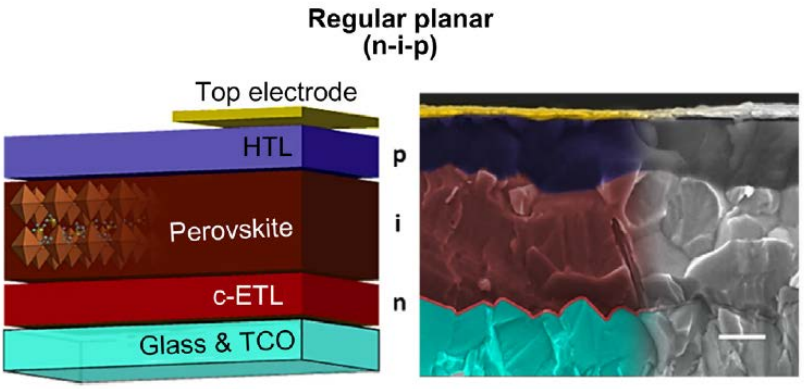

Figure 2.2. Schematic structure of regular planar n-i-p structure (left). Cross-sectional Sem image of the same device architecture. Copyright © 2019 Elsevier.

2.2.4 Inverted Planar pin structure:

In 2013 inverted planar ("p-i-n") device architecture was introduced. The design incorporates p-type and n-type materials as the HTL and ETL correspondingly, as seen in Figure 2.3. Jeng et al. introduced the first inverted planar ("p-i-n") PSCs in their inaugural study. The researchers utilized an anode composed of ITO and poly(3,4-ethylenedioxythiophene) poly(styrene-sulfonate) (PEDOT:PSS) as the substrate. The active layer consisted of a $CH_3NH_3PbI_3$/fullerene (C_{60}) layer, while a thin film of bathocuproine served as the hole-blocking layer[48]. Finally, aluminum was employed as the top cathode. The observed outcome of this particular arrangement resulted in a rather low PCE of 3.0%. Although the initial PCE of inverted planar PSCs was comparatively low, it represented a noteworthy advancement in realizing highly efficient PSCs.

In a very brief period, the PCE of PSCs with an inverted ("p-i-n") structure showed significant advancements, achieving a notable PCE of 16% accompanied by a high V_{oc} of 1.05 eV[49]. Zheng et al. attained a certified PCE of 20.59%[50]. The CTLs of inverted ("p-i-n") PSCs are typically fabricated using PEDOT:PSS and phenyl-C_{61}-butyric acid methyl ester (PCBM), respectively. Nevertheless, the hygroscopic and acidic nature of PEDOT:PSS presents significant obstacles in ensuring the long-term stability of devices. To mitigate this issue, planar devices have included PTAA and its analogs[51,52]. Encouragingly, tiny organic compounds have recently emerged that provide the potential to adjust the structure of hybrid solar cells. In their study, Huang et al. presented a truxene-based HTL. The truxene core, characterized by its planar and symmetrical structure, played a crucial role in promoting a well-organized molecular arrangement inside the film. This molecular arrangement ultimately resulted in a notable efficiency of 18.6%[53].

In addition to organic materials, there has been a change in focus toward inorganic alternatives. Park et al. effectively integrated NiOx as an HTL in PSCs, resulting in a PCE of 19.2%[54]. Additional p-type inorganic metal oxides, such as cuprous oxide (Cu_2O), copper oxide (CuO), copper-doped chromium

oxide (Cu-doped CrOx), molybdenum trioxide (MoO_3), and vanadium oxide (V_2O_5), have been examined as possible HTL materials in PSCs[55,56].

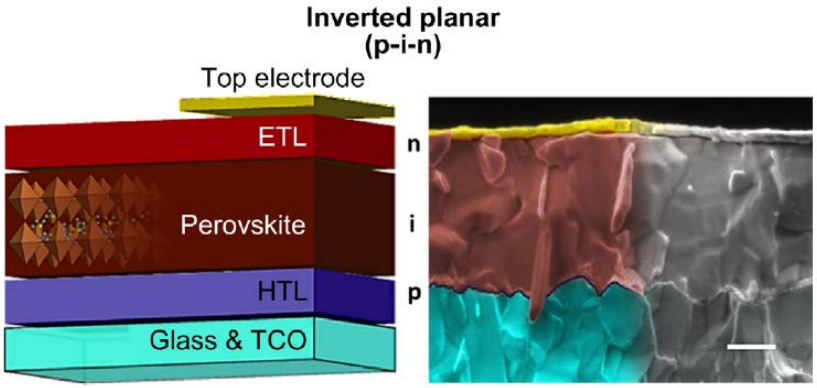

Figure 2.3. Schematic structure of inverted palanar p-i-n structure (left). Cross-sectional Sem image of the same device architecture. Copyright © 2019 Elsevier.

2.3 Perovskite Solar Cells:

Hybrid perovskite materials, characterized by mobile organic cations embedded in a stiff inorganic framework, have remarkable efficacy as light absorbers in photovoltaic systems[57]. This has resulted in significant accomplishments, including attaining an efficiency of 26% in single-cell arrangements and 32% in tandem designs within a relatively short period after introducing hybrid perovskite solar cells in 2009. In contrast to the intricate composition of solar cells such as silicon (Si)[58], gallium arsenide (GaAs)[59], and copper indium gallium selenide ($CuInGaSe_2$)[60], the architecture of hybrid perovskite solar cells exhibits a remarkable degree of simplicity. Efficiencies above 20% can be attained with the use of a perovskite absorber layer strategically positioned between ETL and HTL, therefore obviating the need for complex processing procedures[10]. Hybrid perovskite solar cells exhibit a notable characteristic of not necessitating deliberate doping but demonstrating efficient management of interface recombination, even in the presence of heterogeneous interfaces with CTLs.

Hybrid perovskite polycrystalline absorbers have the capacity to be synthesized by a solution-based approach, operating at a very modest temperature of around 100°C[61]. This attribute makes them exceptionally attractive for deployment in both extensive surface area and tandem photovoltaic systems. The hybrid perovskites, such as methylammonium lead iodide ($CH_3NH_3PbI_3$ or $MAPbI_3$) and formamidinium tin iodide ($HC(NH_2)_2SnI_3$ or $FASnI_3$), are classified under the distinctive ABX_3 perovskite classification. The composition of these materials consists of organic A-site cations (A = CH_3NH^{3+}, $HC(NH_2)^{2+}$), B-site cations (B = Pb^{2+}, Sn^{2+}), and X-site halide anions (X = I^-, Br^-, Cl^-). The word "hybrid" is used to describe the incorporation of both organic and inorganic constituents.

The crystal structure of hybrid perovskites involves the encapsulation of an organic cation within a cage-like arrangement constituted by a BX_6 octahedron as shown in Figure 2.4. This arrangement gives rise to a three-dimensional perovskite network that exhibits interconnectivity. The semiconducting properties of hybrid perovskites are derived from the inorganic BX_3 component. However, essential phenomena such as light absorption, carrier production, and carrier transport take place inside the inorganic framework. The presence of the organic cation plays a crucial role in determining the inherent stability of perovskite crystals.

A standard configuration for a hybrid perovskite device typically includes a glass substrate with a layer of transparent conductive oxide (TCO) on top. This is followed by a layer of TiO_2 acting as the ETL, and a mesoporous titanium dioxide (mp-TiO_2) layer. The perovskite layer, with a thickness of around 500 nanometers, is then deposited on top of the mp-TiO_2 layer. HTL and a layer of metal subsequently follow the perovskite layer. The mp-TiO_2, which refers to the mesoporous form of TiO_2 in the anatase phase, has significantly improved efficiency. This particular phase exhibits a considerable porosity of roughly 60%, contributing to its enhanced performance[62,63]. Various inorganic and organic layers have utilized ETLs and HTLs in these cells. The operating basis of the system entails gathering photo-generated electrons and holes in the ETL and HTL, respectively. Subsequently, the electrons pass via the external circuit and combine with holes at the junction between the HTL and the metal[64].

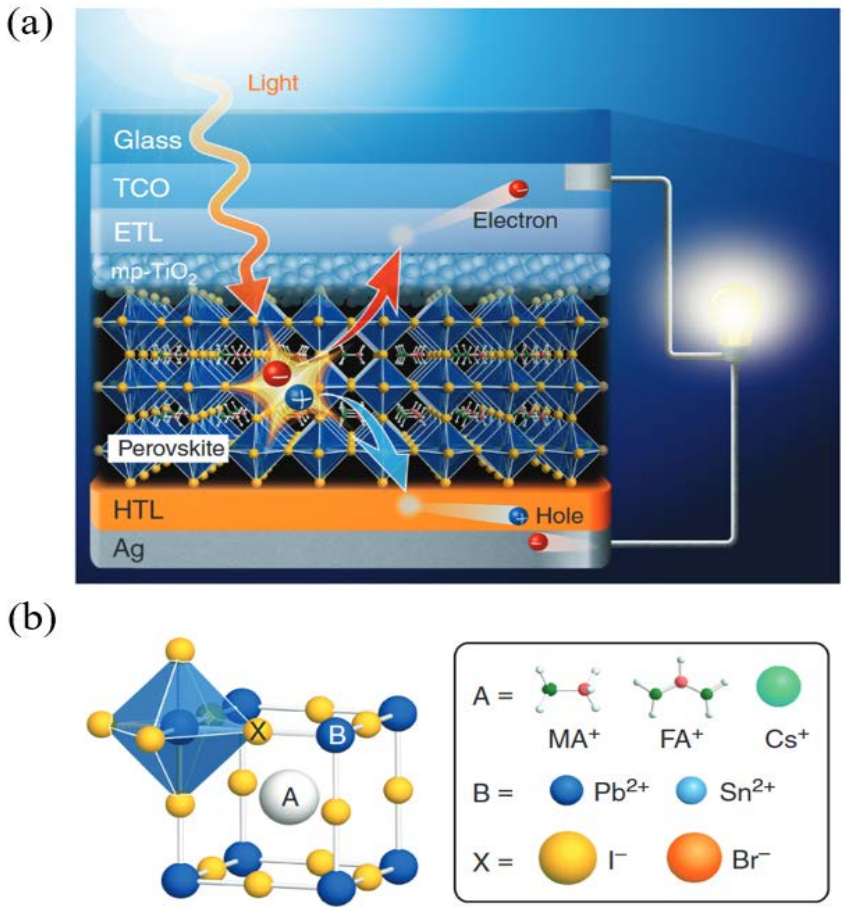

Figure 2.4. a) Graphical illustration of the operation mechanism of perovskite solar cells. b) The crystal structure and atomic structure of the perovskite crystal[65]. Copyright © 2022 Wiley.

2.4 Superior optoelectronic properties of perovskite materials:

Solar cells are inherently optical devices, and it is imperative for semiconducting absorbers to exhibit a high degree of light absorption. The absorption coefficient (α) spectra for several solar cell absorbers, including $MAPbI_3$[66], $CsFAPb(I,Br)_3$, and a Sn-based perovskite of $FAMASnI_3$, are summarized in Figure 2.4b. Fortunately, it is noteworthy that all hybrid perovskite materials demonstrate a significant absorption coefficient (α) value of 10^4 cm^{-1}. This value is equivalent to that of other solar cell absorbers such as GaAs, $CuInGaSe_2$ (CIGSe), CdTe, and Cu_2ZnSnS_4 (CZTS). Based on a comprehensive examination of theoretical and experimental data, it becomes apparent that hybrid perovskites exhibit characteristics of direct-transition semiconductors. Furthermore, the observed high α value in close proximity to the E_g can be attributed directly to the optical transition. The measured value of α at $2*10^4$ cm^{-1} in the vicinity of the E_g of hybrid perovskites demonstrates a constant trend. This trend leads to the determination of the light penetration depth (dp), which can be calculated as $dp=1/\alpha$, resulting in a value of 500 nm. This alignment with the experimental thicknesses of perovskite absorbers is noteworthy.

On the other hand, while considering indirect-transition Si, it is observed that the value of α is significantly lower in the vicinity of E_g, roughly 100 cm^{-1}. As a result, a Si wafer with a thickness of around 100 μm is required. For example, the bandgap energy of $MAPbI_3$ has been determined to be 1.61 eV, but this value may exhibit modest variations depending on the specific analytical and characterization techniques employed[67,68]. The combination of Sn and Pb can form a perovskite material with a narrow energy gap (about 1.2 eV). On the other hand, including lighter halide atoms leads to the production of perovskites with broader energy gaps. Furthermore, it should be noted that the type of A-site cation species leads to minor deviations in the E_g of $MAPbI_3$. According to the Shockley-Queisser theory, solar cells perform best when the E_g falls between 1.0 to 1.6 eV. Interestingly, this range of E_g values coincides well with the E_g range observed in hybrid perovskite materials.

2.5 Origin of high efficiency delivered by perovskite solar cells:

The significant efficiencies (η > 20%) commonly reported in hybrid perovskite solar cells can be attributed to a combination of many physical processes, as illustrated in Figure 2.5. Specific conditions facilitate the generation of photocarriers in hybrid perovskites. These conditions include (i) suitable E_g, (ii) high light absorption coefficient, and (iii) a low exciton binding energy. When these conditions are met, many carriers are generated within the absorber upon light absorption. Moreover, in traditional perovskite devices, the adverse light absorption occurring in the TiO_2 (ETL) and TCO layers is efficiently mitigated. The attainment of adequate carrier production inside the thin perovskite layer, around 500 nm in thickness, and minimum absorption losses in the front TCO and ETL are essential for achieving a substantial optical gain in the perovskite devices.

The carrier recombination rate within the perovskite layer is significantly reduced in carrier collection due to the low defect density, leading to a substantial increase in the values of τ and LD. In contrast to traditional solar cell materials, the electron and hole mobilities in the case of $MAPbI_3$ exhibit approximate equality. The LD values for both electrons and holes exhibit a comparable range. The aforementioned equality confers a considerable benefit in enhancing carrier collecting efficiency in solar systems. Notably, perovskite solar cells efficiently reduce the occurrence of defects at the interfaces of perovskite/ETL and perovskite/HTL. The achievement of high V_{oc} values in perovskite solar cells can be attributed to the restricted carrier recombination occurring inside the perovskite bulk layer and at the interfaces. However, it is essential to acknowledge that the current high-efficiency devices are predominantly limited by recombination occurring at the interfaces.

Hybrid perovskite devices have superior performance to other polycrystalline-based solar cells, despite the generally tiny grain size of perovskite materials. Observing longer τ and higher V_{oc} in small-grain polycrystalline perovskites proves that grain boundaries in hybrid perovskites do not significantly hinder electrical performance. The experimental validation of successful extraction of photocarriers inside the

grain boundary area has been seen, despite a little decrease in light diffusion within this region[69]. Nevertheless, it is observed that the fill factor (FF) exhibits a positive correlation with the average size of perovskite grains. This emphasizes the inclination towards bigger perovskite grains to get enhanced efficiency. As indicated earlier, the fabrication of polycrystalline hybrid perovskite layers is carried out at low temperatures, typically about 100°C, via a spin-coating technique through the use of solution-processed layers is very noteworthy.

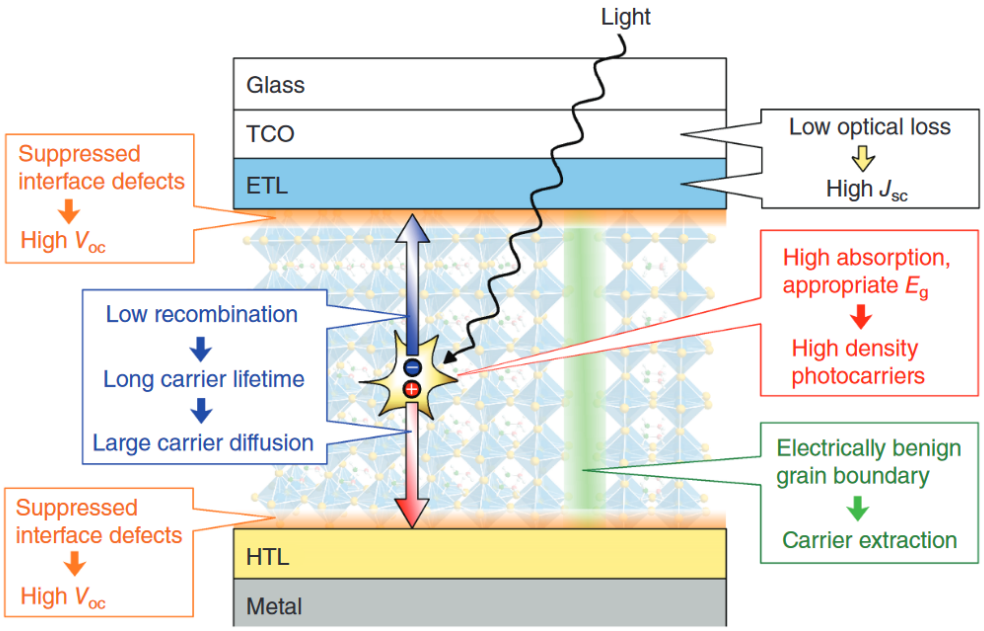

Figure 2.5. The process and traits behind the high performance of perovskite materials in photovoltaic applications, especially solar cells[65]. Copyright © 2022 Wiley.

2.6 Toxicity of perovskite solar cells:

The perovskite composition of $CH_3NH_3PbI_3$ consists of a lead content of over 30% in terms of mass ratio. Although PSCs use modest amounts of perovskites, there is still a possibility of negative impacts on human health and the environment due to probable long-term buildup. Lead halide perovskites generate lead-based compounds that exhibit solubility in water. These chemical substances have the potential to accumulate progressively throughout the food chain, eventually making their way into the human body[23]. The schematic representation of this event may be shown in Figure 2.6.

To tackle these challenges and advance the development of photovoltaic solar cells (PSCs) with reduced toxicity, much research has been conducted on lead-free metal halide perovskites[70,71]. Out of all the available options, tin has emerged as the most viable possibility to replace lead in the perovskite structure. The observed similarities between lead (Pb^{2+}) and tin (Sn^{2+}) can be attributed to their comparable electronic configurations and ionic radii (Pb^{2+}: 119 pm, Sn^{2+}: 110 pm). Tin-based perovskites

have lower bandgaps, ranging from 1.2 to 1.5 eV, due to the reduced ionic radius of tin[72,73]. As a result, tin-perovskites are anticipated to demonstrate greater J_{sc} than their lead counterparts[74,75].

The initial introduction of $CH_3NH_3SnI_3$-based PSCs with a mesoporous architecture was conducted by Noel et al. This study developed a leading device that exhibited a PCE of 6%[76]. Furthermore, the perovskite compound $CsSnI_3$, characterized by a small bandgap of 1.27 eV, has an outstandingly high J_{sc} reaching up to 27.67 mA cm^{-2}. Zhao et al. reported the most notable efficiency for tin-perovskite PSCs to date[77]. They employed a mixed cation tin perovskite [$(FA)_{0.75}(MA)_{0.25}SnI_3$] and achieved a power conversion efficiency (PCE) of around 8%[78]. Incorporating diverse cations into tin perovskites leads to forming a more homogeneous perovskite layer, hence enhancing the stability of Sn^{2+}.

One of the primary obstacles tin-based PSCs faces is tin's inherent propensity to undergo oxidation, namely from Sn^{2+} to Sn^{4+}. This oxidation process gives rise to the creation of Sn^{4+} defects, which can potentially compromise the overall efficiency of the PSCs. Various solutions have been investigated to minimize the occurrence of Sn^{4+}. In their study, Song et al. included hydrazine vapor in the tin-perovskite synthesis procedure, resulting in a notable reduction of 20% in the Sn^{4+} concentration[79]. The good photovoltaic performance for tin-based PSCs was seen in independent investigations done by Chung et al. and Kumar et al. when SnF_2 was added to the perovskite precursor solution[76,80].

3. Advanced concepts in Perovskite solar cells

3.1 Solvent engineering for high-quality perovskite thin films:

Fabricating perovskite films with a consistent and well-defined crystal structure poses a notable challenge in advancing perovskite solar cell technology. The formation of perovskite films is greatly influenced by the solvent and subsequent processing circumstances, leading to substantial fluctuations in the microstructure and quality of the films. Researchers have developed numerous solvent engineering approaches to address the challenges of producing high-quality perovskite films. Solvent tuning, a commonly employed technique, encompasses solvent engineering to enhance perovskite films' solubility, crystallization dynamics, and microstructure. Solvent engineering presents a highly advantageous and cost-effective approach for attaining a simple fabrication process and sustained operational durability of (PSCs)[81,82]. Hence, a comprehensive understanding of the chemical and physical properties of the precursor solution is imperative to utilize the essential trait of perovskite materials which is solution processability. This knowledge plays a crucial role in controlling the nucleation and crystal growth processes that govern the morphology of thin films, as well as the ultimate properties of the resulting devices[83]. The intermediate phase emerges from the precursor solution during the film formation process and can generate intermediate species within the precursor film. The intermediate phase governs grains' dimension and distribution and phase transitions' temperature and stability[84,85]. The binding of Sn^{2+} and the stability of the intermediate phase complex are influenced by the polarity of the solvent, thereby impacting the quality of the perovskite films. The field of solvent engineering involves investigating the interactions between strong polar solvents and Sn^{2+} ions, which subsequently prompts research into the intermediate phases of perovskite materials. To achieve perovskite films with minimal defects, high quality, and no pinholes. The fundamental investigation of solvent engineering in the development of surface provides a theoretical foundation for the fabrication and production of PSCs[86,87,88].

3.1.1 Crystal growth dynamics:

It is expected that a more thorough understanding of the nucleation and crystal formation mechanisms in solution will lead to the exploration of a broader spectrum of applications in the field of perovskite-based optoelectronics. The process of generating perovskite thin films from precursor solutions involves three distinct stages: solution phase, nucleation phase, and crystal formation phase. Among these stages, the nucleation phase holds significant importance in the production of high-quality thin films. This chapter aims to elucidate the fundamental principles underlying the nucleation process in perovskite

solutions. The consideration of surface energy facilitates the comprehension of nucleation, as the basic principles governing nucleation and crystal formation are predicated upon the surface energy exhibited by a solid immersed in a liquid medium. Measuring surface and interfacial energy is crucial in understanding the various stages of particle formation, such as nucleation, growth, Ostwald maturation, coalescence, etc[89]. The nucleation process represents a crucial step in the localized formation of a distinct thermodynamic phase[90]. The process of particle nucleation initiates when there is a rise in the concentration of the solution, particularly when the solubility of the solute significantly exceeds that of the solid[91]. In the context of nucleation, homogeneous nucleation refers to the phenomenon where the formation of a core occurs uniformly, leading to the growth of chalcocite crystals, as opposed to selectively nucleating at specific sites. The thermodynamic characterization of homogeneous nucleation entails the sum of the volume free energy (ΔG_v) and the surface free energy (ΔG_s) to yield the total free energy (ΔG), as depicted in Figure 3.1a. The magnitude of r^2 and the magnitude of r^3 exhibit a direct relationship with ΔG_s and ΔG_v, respectively, as demonstrated in Equation 3.1[92].

$$\Delta G = \Delta G_s + \Delta G_v = 4\pi r^2 \gamma + 4/3\ \pi r^3 \Delta G_v$$

Where r denotes the radius of a spherical particle and γ represents the interfacial energy between the crystalline surface and the supersaturated solution. The critical radius, denoted as (r*), substantially impacts the nucleation process in solutions. Nuclei with radii smaller than r* undergo redissolution, while those with radii exceeding r* exhibit thermodynamic stability and continue to grow.

The effective management of crystal growth is of paramount importance in enhancing the quality of perovskite. The LaMer model is frequently used to describe monodisperse hydrosols' formation mechanism[93]. Therefore, this particular theoretical framework serves as a fundamental cornerstone for comprehending the development of uniform colloidal particles. The provided diagram illustrates the three distinct stages of the LaMer process. During the initial phase of pre-nucleation, the aggregation of solute particles occurs as the solvent undergoes evaporation. These particles exist in a critical state of undersaturation, indicating a lack of nucleation sites. This phenomenon is illustrated in Figure 3.1b[94]. In the subsequent phase of critical supersaturation, as the solvent is progressively diminished, the particles experience an elevation in their concentration in relation to one another, reaching a state where core sites are being formed. At this stage, the nucleation sites commence their formation and subsequent growth. The enhanced formation and increased accumulation of core sites characterize the third growth phase. Nucleation ceases to occur beyond the second stage when the concentration of particles is insufficient for consumption[95].

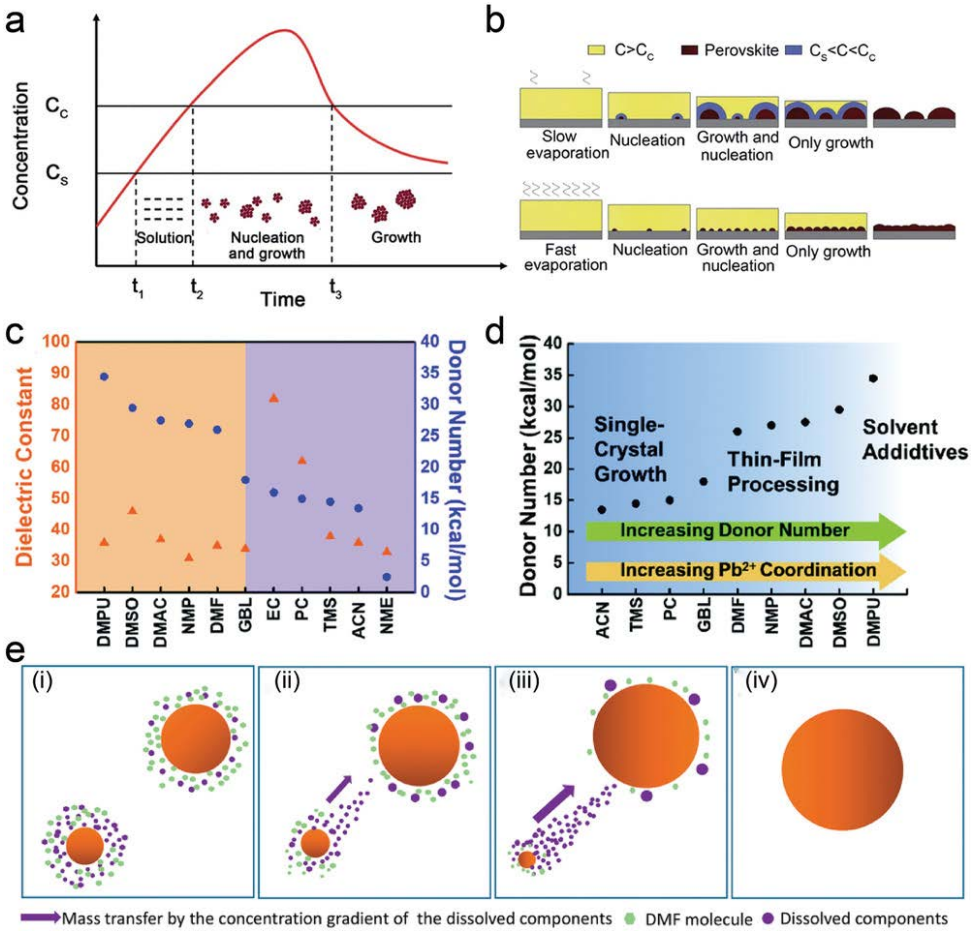

Figure 3.1. Crystallization dynamics of perovskite materials. Copyright © 2018, American Chemical Society.

Hence, It can be inferred that to prepare high-quality perovskite film, it is advisable to minimize the duration of the nucleation procedure and discourage re-nucleation during the growth process[96]. One significant concept that characterizes the mechanism of growth is Ostwald maturation. This phenomenon pertains to the dissolution of minute particles and the subsequent re-deposition of the dissolved components onto the surface of larger particles[97]. The Ostwald phenomenon can be attributed to the dissimilar solubility of nanoparticles characterized by varying particle sizes, as indicated by the Gibbs-Thomson relationship. This relationship establishes a positive correlation between the chemical potential and the particle radius, suggesting that smaller particles exhibit higher chemical potential. Nanoparticles characterized by a small radius tend to undergo re-decomposition and recombination when in proximity to nanoparticles possessing a larger particle size. This behavior can be attributed to the elevated surface energy associated with smaller particle sizes[98].

Consequently, as decomposition and recombination progress, the larger particles expand and grow while the smaller particles decompose until they ultimately vanish[99]. Hence, in the process of Ostwald

maturation, there is a continued reduction in the quantity of particles alongside a concurrent increase in particle size[100]. The Ostwald maturation process has been employed to elucidate the phenomenon of grain expansion through agglomeration in perovskite films. However, conflicting claims have suggested the differentiation between Ostwald maturation and agglomeration[101]. Fick's law describes the process of particle growth from a solution at the growth point through a diffusion mechanism, which involves the movement of particles from an area of higher concentration to an area of lower concentration. This process can be divided into two components: (1) the transportation of particles from the solution to the surface of the crystal, and (2) the reaction of the growing species at the crystal surface[102,102]. The Gibbs-Thomson effect posits that larger particles exhibit greater resistance to dissolution and experience accelerated growth compared to smaller particles. Surface reactions or diffusion mechanisms influence the increase in particle size. The enhancement of controlled crystal development can be achieved by attaining homogeneous particles, even though the monomer concentration at the particle's surface may approach that of a native solution due to a delayed surface reaction as a result of the steady-state diffusion of the solute.

3.1.2 Solvent-solute coordination regulation:

Regulating the coordination interaction between solvent and perovskite precursors in precursor solution has been recognized as the most effective strategy for controlling the nucleation and growth of perovskite crystals[103]. The coordination between specific functional groups of the solvent and the perovskite colloidal precursor largely influences the perovskite film's nucleation, crystal growth, and microstructure. For example, the interaction of DMF with metal halide is assigned to the coordination between C=O functional group of DMF and the metal cation such as Sn^{2+} or Pb^{2+}[104,105], while DMSO interacts with the metal halide through the sulphoxide (S=O) functional group[106,107]. Gutmann defined donor number (D_N) to determine the coordination ability of solvent with solute, where solvent with higher D_N shows higher ability to donate electrons for coordinating with electron acceptor[108,109]. For perovskite precursor solution, a solvent with high D_N tends to form a strong coordination complex with electron acceptor such as Pb^{2+} or Sn^{2+}. At the same time, those with low D_N exhibit a weak affinity to the metal cation. In this case, a solvent with high D_N will be evaporated more slowly during the annealing process of perovskite film, which retards the growth of perovskite crystal. While solvent with low D_N will be evaporated more quickly during the annealing process, which accelerates the nucleation of perovskite crystal[110,111]. Therefore, the coordination ability of solvent plays a critical role in determining the crystallization process of perovskite crystal from precursor solution. As discussed above, by incorporating different solvents with various D_N (Figure 3.2d), the coordination interaction between solvents and perovskite precursors could be adjusted, which provides a facile method to control the solvation, crystallization, and growth dynamics of the perovskite films (Figure 3.2e).

In addition to the LaMer model, the Ostwald ripening model is another important model often used to explain the process of crystal nucleation and grain growth. The Ostwald ripening model is a more effective and understandable method to describe small crystal growth into large one via a thermodynamically spontaneous process[99,112,113]. It demonstrates that small-sized crystal grains with higher surface energy and solubility will tend to dissolve and redeposit on the surface of adjacent large crystal grains with lower surface energy. Finally, the small-sized grain will coarsen with the large one. This process will decrease the concentration of crystal grains and solutes in the system and result in the enlarged average size of the large crystal grains (Figure 2f)[113]. Inorganic metal halide salts, a perovskite precursor material, are barely or even completely insoluble in most solvents commonly used in large-scale deposition techniques.

Therefore, to prepare a uniform perovskite precursor solution, solvent selection is largely limited. Currently, some polar and aprotic solvents with high D_N to coordinate with lead halide salts, such as DMF, DMSO, N-methyl-2-pyrrolidone (NMP), dimethylacetamide (DMA), and γ-butyrolactone (GBL), are widely used to prepare perovskite precursor solution[104,105,106,114,115,116,117]. These solvents are strong electron donors that could coordinate with electron acceptor Pb^{2+} or Sn^{2+} to form a uniform coordinated colloidal solution. Nevertheless, these solvents show different effects on perovskite precursor colloidal stability, film crystallization dynamics, and PSCs performance due to different physical and chemical properties[118]. For instance, DMSO is the universal solvent for tin perovskites. However, mixed DMF:DMSO is the most widely used solvent for lead perovskites. DMSO provides higher coordination strength than DMF, which is more suitable for the fast crystallizing tin perovskites. However, DMSO was found to oxidize Sn^{2+} to Sn^{4+}, which increases the hole concentration (P-doping) in the absorber film, which devastates the photovoltaic performance. DMSO, with higher D_N than DMF, has been shown to form a perovskite film with low roughness and greatly increased surface coverage. S=O group in DMSO possesses a higher electron cloud density than C=O group in DMF, making DMSO a stronger Lewis base than DMF. The stronger interaction of DMSO with PbI_2 results in a shorter Pb=O bond between DMSO and PbI_2 (2.386 A^o) compared to DMF (2.431 A^o)[119,120]. As a result, DMSO, with high coordination capacity to PbI_2 could prevent rapid interaction between MAI and PbI_2 in the precursor solution[121,122]. In addition, a stable intermediate phase of MAI-PbI_2-DMSO will be formed during film formation, which greatly contributes to the retarded nucleation and growth of perovskite crystal. It was observed that as the increased amount of DMSO in the precursor solution, the deposited perovskite film showed a more uniform morphology without pinholes and caves, and the crystals were also found to be in a larger size, better contact with the substrate and better alignment along the vertical direction. Most importantly, no grain boundaries (GBs) were observed in the horizontal direction of the perovskite film[117]. The excellent perovskite film quality was mainly attributed to forming a stable intermediate phase and the higher boiling point of DMSO, which effectively retarded the crystallization rate of perovskite crystals[117,120]. However, if the crystallization rate is too slow (i.e., a high concentration of

DMSO is used as solvent), perovskite film shows inhomogeneous size of perovskite crystal grains and high surface roughness. These findings clearly show that the morphology of perovskite film can be well controlled by adjusting the solvent system's coordination. In this way, the performance of the device can be easily optimized. In addition to DMSO, other solvents with higher D_N than DMF, such as DMA, NMP, GBL, HMPA, etc., have also been used as single solvent or co-solvent to prepare perovskite precursor solutions, and these solvents have shown similar chemical and physical characteristics as DMF or DMSO[123]. Nevertheless, the DMF-DMSO solvent system is still most commonly used to fabricate high-quality perovskite film toward high-performing PSCs[122,124,125], which might be closely related to the favorable property of the DMFDMSO solvent system, such as polarity, viscosity, coordination ability with PbI_2, etc[126,127].

However, the situation for tin perovskites is quite different. Sn^{2+} cation is much more reactive than Pb^{2+} due to its electronic properties. The interaction between SnI_2, for example, and the organic halide such as FAI to form $FASnI_3$ takes place quickly compared to the lead-based counterpart such as $FAPbI_3$ or $MAPbI_3$. As a result, tin perovskites show faster crystallization dynamics than lead, meaning that the nucleation and crystal growth phases take place quickly, leading to inhomogeneous growth. Consequently, the perovskite film microstructure is of low quality, the grain domains are small, and the film suffers from pin holes and internal cavities. As a result, the photovoltaic performance is incomparable to that of lead perovskites. One more noteworthy consequence of fast crystallization is the low concentration of tin perovskite solutions compared to lead, which leads to a very thin film of the absorber material. For comparison, the thickness of tin perovskites ranges from 200 to 350 nm, while lead perovskites range from 400 to 800 nm[128]. To sum up, solvent engineering is one of the effective approaches to regulating crystallization and inhibiting the oxidation of Sn^{2+}, enhancing the perovskite´s microstructure and device efficiency.

3.2 Antisolvents for high-quality perovskite films:

3.2.1 What is an Antisolvent.

Antisolvents are fluids (liquid, vapor, or supercritical gas) that do not dissolve the solute but are miscible with the solvent of the solution. They are also known as nonsolvents (to a specific solute). A solution's solubility is quickly decreased, and the addition of an antisolvent brings about local supersaturation conditions leading to Precipitation or crystallization of the precursor. It is also appropriate for heat-sensitive materials because it is a room-temperature approach. It is also utilized to produce medicinal compounds[129,130,131,132], proteins[133,134], micro- and nanoparticles[135,136], inorganic materials[137], polymers[138,139], and recently, perovskite light-emitting diodes (LEDs)[140,141,142] and solar cells, it has a

wide range of applications. The mechanism of antisolvent-assisted crystallization or precipitation is shown in Figure 3.2.

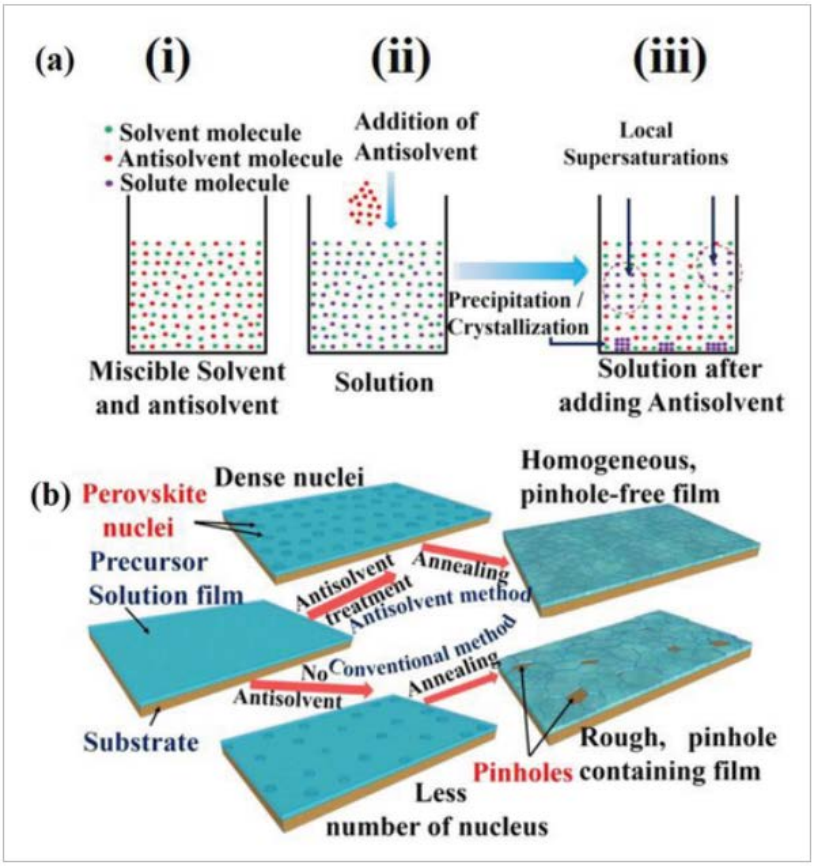

Figure 3.2. a) illustrative diagram for antisolvent crystallization mechanism. b) The mechanism of film formation, where the addition of the antisolvent induces the formation of dense films of highly ordered and oriented perovskite crystals. Copyright © 2020, Wiley.

3.2.2 The role of Antisolvent in film formation and crystallization:

Several techniques have been employed to address the challenges associated with the quality of perovskite films. These techniques include the two-step or sequential deposition technique, vapor-assisted process, printing, spray coating, and others[143,144]. Although significant advancements have been made in enhancing the quality of perovskite films through various techniques, there remains a necessity for further refinement. Additionally, particular challenges have been identified, such as the time-

consuming nature of the two-step sequential deposition process, which often results in incomplete conversion and is primarily applicable for depositing on mesoporous layers. Furthermore, the vapor-assisted process necessitates using sophisticated instruments, thereby increasing costs and limiting substrate options. Consequently, these factors have motivated researchers to explore and develop novel techniques. Thus, applying antisolvent treatment to the perovskite layer has emerged as a highly effective and widely adopted method for enhancing the perovskite layer's quality in PSCs. This technique, characterized by its expeditious and straightforward one-step process, has garnered significant success and popularity. The perovskite layer can be treated using various methods involving antisolvent. These methods include the antisolvent dripping process, the antisolvent-solvent extraction process, and the antisolvent vapor-assisted process.

3.2.3 Antisolvent dripping:

During the spin coating process, a specific amount of the antisolvent is incrementally introduced onto the perovskite layer in a technique known as antisolvent dripping. In a seminal study conducted by Xiao et al., they explored the application of antisolvent for perovskite layers. Specifically, they investigated the efficacy of a fast deposition-crystallization (FDC) process utilizing various solvents as antisolvents for perovskite. The solvents examined included chlorobenzene, toluene, benzene, xylene, methanol, ethanol, 2-propanol, ethylene glycol, tetrahydrofuran (THF), chloroform, benzonitrile, and acetonitrile. During the spin coating process, the antisolvent was introduced onto the rotating perovskite substrate within a short time frame after the initiation of the coating procedure[145]. The user's text is already academic and does not requires any rewriting. The film exhibited a rapid crystallization process, as evidenced by its color's prompt and noticeable darkening. In contrast, in traditional spin coating, the crystallization process occurred solely after the application of thermal treatment at approximately 100°C. Uniform film formation and complete surface coverage have been successfully achieved using chlorobenzene, benzene, xylene, and toluene, as evidenced by the results obtained from testing various solvents. It is noteworthy to mention that MAI, PbI_2, and $MAPbI_3$ exhibit lower solubility in these solvents, and the antisolvents induced rapid supersaturation by decreasing the solubility of the perovskite precursors. This phenomenon facilitates a swift crystallization process and the subsequent formation of perovskite films during the spin coating technique. In contrast, solvents that exhibit high or moderate solubility towards perovskite precursors, such as methanol, ethanol, ethylene glycol, acetonitrile, tetrahydrofuran (THF), and benzonitrile, have been observed to yield undesirable outcomes, including the formation of large PbI_2 crystals or the production of transparent films. The devices optimized in this study had a perovskite layer thickness of 350 μm and were fabricated using chlorobenzene antisolvent. These devices demonstrated an impressive average PCE of 13.9 ± 0.7%, which surpassed the PCEs achieved by other contemporary fabrication methods for PSCs. The increase in the PCE has been

ascribed to the homogeneous deposition of the perovskite absorber layer, which exhibits a lack of pinholes, as depicted in Figure 3.2. The enhanced film exhibited increased light absorption capabilities and decreased defects, improving both J_{sc} and V_{oc}.

Figure 3.3. Illustrative diagram of the dripping process of an antisolvent[146]. Copyright © 2021, Nature.

3.2.4 Antisolvent treatment for lead-free perovskites:

The potential limitations on the large-scale production of lead-based PSCs may arise from the hazardous properties associated with lead as a heavy and bioavailable element. Due to this rationale, researchers are driven to identify suitable substitutes for lead in perovskite materials. Sn^{2+}, Bi^{3+}, Ge^{2+}, Sb^{3+}, and other elements have demonstrated promise as potential substitutes for Pb in lead-free perovskite/perovskite-like materials. However, it should be noted that the PCE of lead-free PSCs remains significantly lower than that of lead-based PSCs[147,148,149,150]. In the field of lead-free perovskites, Sn^{2+} based materials have emerged as up-and-coming alternatives. Unfortunately, tin perovskites encounter a significant challenge in the form of oxidation degradation, wherein Sn^{2+} ions are oxidized to Sn^{4+} ions. However, incorporating SnF_2 into the perovskite structure can mitigate this detrimental process, effectively inhibiting the oxidation reaction. An additional problematic aspect associated with Sn perovskite pertains to the lack of control over crystallization, resulting in the formation of nonuniform films characterized by pinholes. In their study, Lee et al. employed SnF_2 and adopted the antisolvent treatment technique described by Jeon et al., utilizing toluene as the antisolvent to produce a $FASnI_3$ film[151,122]. Despite the antisolvent treatment improving film quality compared to the untreated film, the presence of uncovered areas, commonly referred to as pinholes, remained prominent. Nevertheless, the employment of a blended solvent comprising of dimethylformamide (DMF) and dimethyl sulfoxide (DMSO), in conjunction with pyrazine (in the presence of tin^{2+} fluoride (SnF_2)), and subsequent treatment with an antisolvent, resulted in the fabrication of a film composed of formamidinium tin triiodide ($FASnI_3$) of exceptional quality. In

their study, Liao et al. employed chlorobenzene, toluene, and diethyl ether as antisolvents to drip onto a spinning precursor solution of $FASnI_3$. This precursor solution was prepared using a mixed solvent of DMF and DMSO, which was further supplemented with SnF_2. The dripping process was carried out on an ITO substrate coated with PEDOT:PSS as HTL. Recently, research has revealed that the utilization of diethyl ether has resulted in the production of perovskite films of exceptional quality, characterized by the absence of pinholes. In contrast, the efficacy of chlorobenzene and toluene in generating perovskite films with complete coverage, devoid of pinholes, was comparatively limited. The devices of architecture ITO/PEDOT:PSS/$FASnI_3$/C_{60}/BCP/Ag, treated with diethyl ether, exhibited a PCE of approximately 5.41%. The champion device achieved a PCE of 6.22%, with a steady state efficiency of roughly 6%.

3.2.5 Green Antisolvents:

Ensuring environmental safety is a paramount concern in safeguarding the planet. This perspective entails the avoidance or regulated utilization of processes involving toxic or environmentally hazardous substances. Therefore, despite their significant potential, the utilization of toluene, chlorobenzene, and other antisolvents with toxic or harmful properties may encounter limitations in industrial-scale production procedures. The investigation conducted by researchers involved the use of environmentally benign antisolvents, yielding intriguing findings. Ethyl acetate may be considered an environmentally friendly antisolvent, as it lacks the potential health risks associated with substances such as toluene, chlorobenzene, and dichloromethane. Ethyl acetate has demonstrated superior performance compared to chlorobenzene in producing high-quality perovskite films. This is evidenced by the films being pinhole-free and smooth, reducing defects and increasing light absorption, among other benefits. The phenomenon of rapid crystallization was observed when ethyl acetate was introduced, which facilitated the disruption of the PbI_2–MAI–DMSO intermediate phase by displacing the DMSO solvent. The study's results revealed a notable similarity in the crystallinity and optoelectronic characteristics between unannealed and annealed perovskite films[125]. This finding provides strong evidence to support the notion that ethyl acetate can effectively induce perovskite crystallization at ambient temperatures. Furthermore, ethyl acetate as a solvent for spiro HTM has been found to enhance the stability of PSCs to a greater extent[152].

Additionally, sec-butyl alcohol possesses the potential to function as an environmentally friendly antisolvent, exhibiting a comparable level of toxicity to that of ethyl acetate. In their study, Zhang et al. employed sec-butyl alcohol as an antisolvent during the manufacturing process of a $MAPbI_3$ perovskite film on a PEDOT:PSS substrate[153]. Despite its complexity, the process involved an additional step of antisolvent soaking. After optimizing various parameters such as precursor ratio and antisolvent soaking

time, the resulting devices demonstrated the highest power conversion efficiency (PCE) of 14.3%. The device configuration used in this study was ITO/PEDOT:PSS/perovskite/phenyl-C_{61}-PCBM/Al. Moreover, sec-pentyl alcohol has been employed as an ecologically sustainable antisolvent. Significantly, the moderate polarity of the substance renders it an appropriate antisolvent for generating larger yet compact perovskite grains[154]. While o-xylene and 1,2,4-trimethylbenzene do not exhibit the same performance as chlorobenzene as antisolvents, it is worth noting that these compounds are comparatively less toxic than halogenated solvents such as chlorobenzene. In their study, Fang et al. employed o-xylene and 1,2,4-trimethylbenzene as antisolvents for perovskite and solvents for $PC_{61}BM$, respectively, as alternatives to chlorobenzene. Notably, the researchers successfully combined the antisolvent treatment and ETL deposition steps into a unified process, resulting in a significant increase in power conversion efficiency (PCE) to a value exceeding 16%[155].

Moreover, anisole or methoxybenzene can serve as a viable alternative to highly toxic antisolvents with superior performance. Anisole, in particular, exhibits significantly reduced health risks while yielding perovskite films of comparable or even superior quality. Notably, anisole molecules exhibit intermolecular interactions with DMF and DMSO through hydrogen bonding. Additionally, anisole has a higher boiling point than chlorobenzene, toluene, and diethyl ether. These factors are crucial in producing high-quality perovskite films[156,157]. Yavari et al., have successfully attained PCEs of 19.9% and 15.5% by employing anisole as an antisolvent within and outside the glovebox. Moreover, anisole has the potential to serve as a solvent for HTL materials, thereby offering a viable alternative to the use of hazardous solvents such as chlorobenzene. In their study, Zhao et al. achieved a PCE exceeding 19% by employing anisole as the antisolvent. Zhang et al., achieved a PCE exceeding 19% by employing anisole as the antisolvent.

Moreover, tetraethyl orthosilicate has been employed in antisolvent treatment due to its lower toxicity. In their study, Wang et al. achieved an efficiency of over 17% for solid substrates and over 14% for flexible substrates of inverted PCSs. This was accomplished by utilizing tetraethyl orthosilicate as an antisolvent. Furthermore, tetraethyl orthocarbonate has been employed as an environmentally friendly antisolvent. Moreover, it is worth noting that tetraethyl orthocarbonate exhibits a significantly elevated boiling point of 161 °C, rendering it a suitable candidate for the production of perovskite films of superior quality. Additionally, its dielectric constant is deemed satisfactory, enhancing its desirability for this purpose[158]. Wang et al., employed tetraethyl orthocarbonate as an antisolvent in their study and successfully attained a power conversion efficiency (PCE) exceeding 17% in inverted PSCs[159].

3.3 Basics of energy bands alignment in perovskite solar cells:

CTLS in perovskite solar cells are crucial components positioned between electrodes and the absorber film. These materials significantly impact the overall performance of optoelectronic devices based on perovskite materials[160,161,162,163]. Precisely, the alignment of perovskite band structures with neighboring CTLs can facilitate the effective injection or extraction of charges into or from the perovskite film, thereby mitigating undesired charge transfer phenomena such as electron-hole recombination[164,33,165]. Consequently, the regulation of the energy level alignment (ELA) at the interfaces connecting perovskites and CTLs has the potential to mitigate the loss of V_{OC} in photovoltaic devices and decrease the required driving voltage in PSCs[166]. This chapter explains the possible alignment schemes between perovskite films and CTLs. The objective is to enhance the performance of perovskite hybrid interfaces through optimization.

As depicted in Figure 3.4, multiple interfaces are shown, namely the ETL/perovskite interface (referred to as b), the perovskite/HTL interface (referred to as c), the cathode/ETL interface (referred to as a), and the HTL/anode interface (referred to as d). The significance of interfaces lies in their ability to determine charge extraction through the modulation of energy offsets. The energy offsets at the interfaces of b and a determine the electron transfer process. In this process, electrons are transferred from the conduction band minimum (CBM) of the perovskite material to either the LUMO level of the organic material or the CBM of the inorganic material in the ETL. Subsequently, the electrons are transferred to the cathode, then to the external circuit. Without significant barriers to electron transfer at the interfaces of b and a, the extraction of free electrons from the perovskite material to the ETL can occur efficiently. Simultaneously, it is imperative to minimize or impede the undesired transfer of holes at the interfaces to prevent unfavorable recombination events from taking place at these interfaces. The energy offsets present at the interfaces labeled as c and d influence the hole transfer process. Specifically, holes are transferred from the VBM of the perovskite material to either the HOMO of the organic material or the VBM of the inorganic material, depending on the type of HTL used. Subsequently, the holes are further transferred to the anode. Comparably, in the absence of significant obstacles to hole transfer at the interfaces, the unbound holes can be effectively extracted from the perovskite layer and subsequently transferred to the HTL, ultimately reaching the anode in a seamless manner. Minimization or prevention of undesirable electron transfer at the interfaces of c and d is imperative to mitigate the occurrence of unfavorable recombination at these interfaces. In general, the ELA at interfaces plays a crucial role in determining the transfer and transport of charges. Additionally, it is closely associated with the recombination processes occurring at the interfaces, thereby significantly impacting the device's performance. Therefore, it is crucial to comprehend the ELA at different interfaces to develop photovoltaic devices with enhanced efficiency.

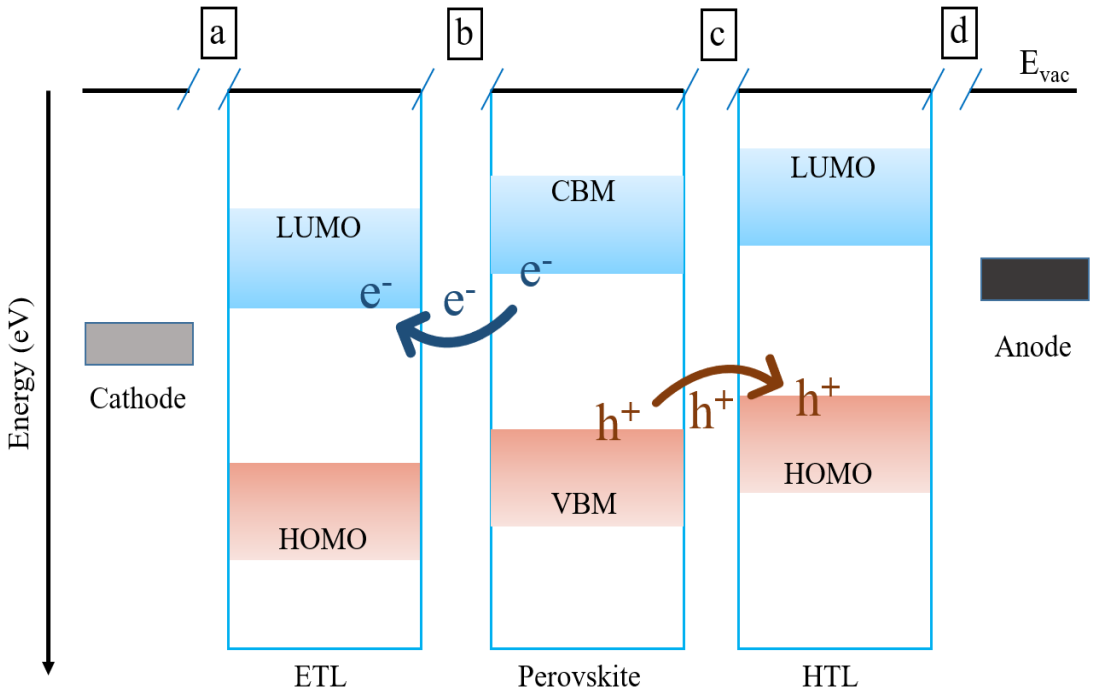

Figure 3.4. Graphical illustration of the interfaces in a single junction planar perovskite solar cell, it illustrates the mechanism of charge separation and extraction from the absorber perovskite film to the CTLs. a) cathode/ETL interface. b) ETL/Perovskite interface. c) Perovskite HTL interface. d) HTL/Anode interface.

The ELAs at the interfaces between perovskite and HTL hybrids play a crucial role in solar cells. These alignments are essential for efficient charge extraction and for achieving high V_{OC}. Ideally, the energy difference between the VBM of the perovskite material and the HOMO level of the HTL should be sufficiently small to prevent a drop in the V_{OC}. Similarly, the energy difference between the CBM of the perovskite material and the LUMO of the ETL should also be minimized to avoid any adverse effects on the V_{OC}. A classification system for the band alignment of CTLs with frontier orbitals that are either deep-lying or low-lying in perovskite films can be broadly categorized into four distinct types. These types are characterized by explicit discussions on the behavior of carriers at the interface, as depicted in Figure 3.5. As depicted in Figure 3.5a, the interaction between the absorber films and HTLs possessing low-lying LUMO and HOMO energy levels results in creating a staggered gap heterointerface. This configuration is advantageous for the extraction of holes due to the absence of barriers and effectively hinders the extraction of electrons (conversely, as demonstrated in Figure 3.5c, this is true for ETLs. In the case of a straddling-gap heterointerface featuring a small bandgap HTL, as depicted in Figure 3.5b, electron-hole recombination losses can arise within the HTLs. This can be attributed to the lack of electron and hole-blocking barriers[167]. On the other hand, a reverse straddling-gap heterointerface can be established in cases where the HTL possesses a HOMO level that is deeply situated and a wide bandgap,

as depicted in Figure 3.5d. This particular band alignment is deemed unsuitable for charge collection as it hinders the extraction of both electrons and holes.

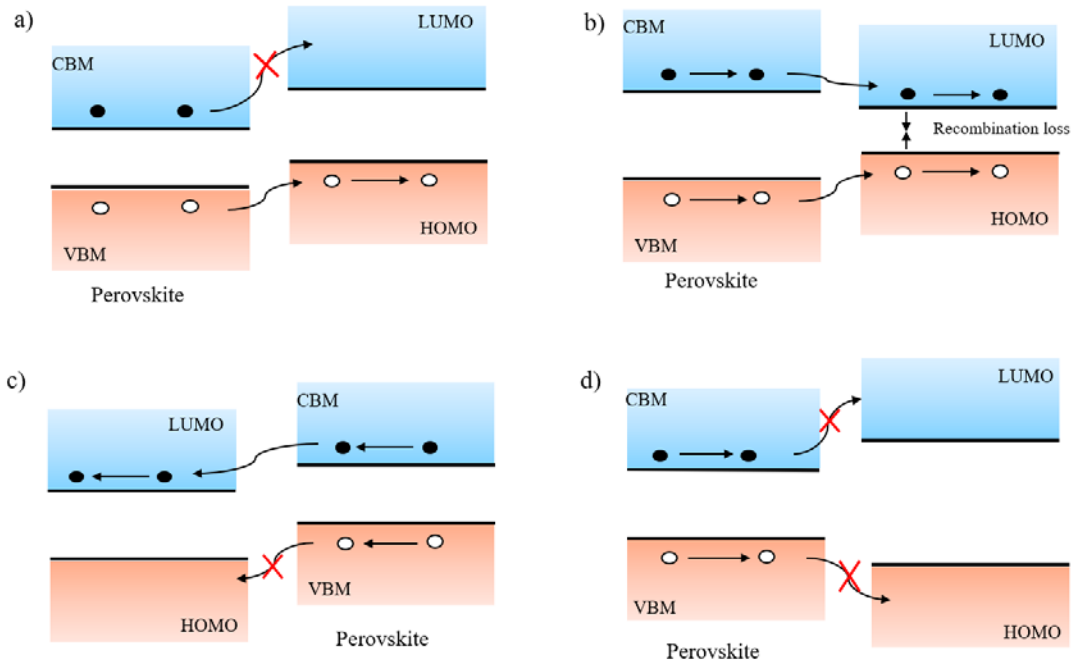

Figure 3.5. Schematic illustration of energy bands alignment possibilities of perovskite/CTL interface, which could be HTL or ETL. a) Interface with a staggered gap, which is suitable for hole extraction but exercises an energy gap that blocks electron extraction. b) Straddling-gap interface configuration. c) reverse staggered-gap. d) reversed straddling gap.

Tin perovskites possess a direct bandgap ranging from 1.2 to 1.4 eV, indicating a significant ability to achieve high-performance relative to the Shockley-Queisser limit, which stands at approximately 33% [77,168]. In addition, it should be noted that in the absence of external factors such as grain boundaries, energetic disorder, and impurities, charges mobility in tin perovskites exhibits superior performance compared to those containing lead. This can be attributed to the lighter nature of tin, which results in a smaller Fröhlich interaction due to its higher longitudinal optical (LO) phonon frequencies[169,170]. Nevertheless, it can be observed from Figure 3b that the atomic energy levels originating from Sn and Pb give rise to distinct energy levels within perovskite materials[171]. The determination of the CBM in perovskite is reliant on the overlapping between the p-orbitals of the metal and the s-orbitals of the halide. Similarly, the determination of the VBM is influenced by the overlapping between the s-orbitals of the metal and the p-orbitals of the halide. The replacement of Pb with Sn results in an upshift of both VBM and CBM due to the higher energy levels of the s-orbital states of Sn compared to those of Pb[172]. The disparity in energy levels poses a challenge in selecting appropriate charge transport materials.

Moreover, it should be noted that tin, with its four valence electrons, exhibits a tendency for the divalent Sn^{2+} cation to undergo oxidation, forming the tetravalent Sn^{4+} cation. On the other hand, the heavier element lead (Pb^{2+}) remains stable due to the presence of stable 6s2 electrons, which exhibit a stronger inert pair effect. Tin perovskites are subject to challenges arising from their elevated background carrier density and increased defect density, which can be attributed to oxidized Sn^{4+} ions. Furthermore, the pronounced Lewis acidity exhibited by Sn^{2+} serves to expedite the process of crystallization, thereby leading to the production of films with inferior quality characterized by an increased density of defects (as depicted in Figure 3.6a). As illustrated in Figure 3.6c, the proposed mechanism suggests that the severe degradation of tin-based perovskites can be facilitated by the presence of O_2, H_2O, and Sn^{4+}. The aforementioned issues posed a significant impediment to using tin perovskites during their initial implementation phase[173]. In addition to the considerable demand for environmentally friendly PSCs, the past ten years have witnessed substantial advancements in the performance of tin perovskites[174,175]. These advancements have been achieved through the implementation of diverse engineering strategies aimed at mitigating tin oxidation, regulating perovskite crystal growth, and enhancing charge extraction efficiency[176,177,178].

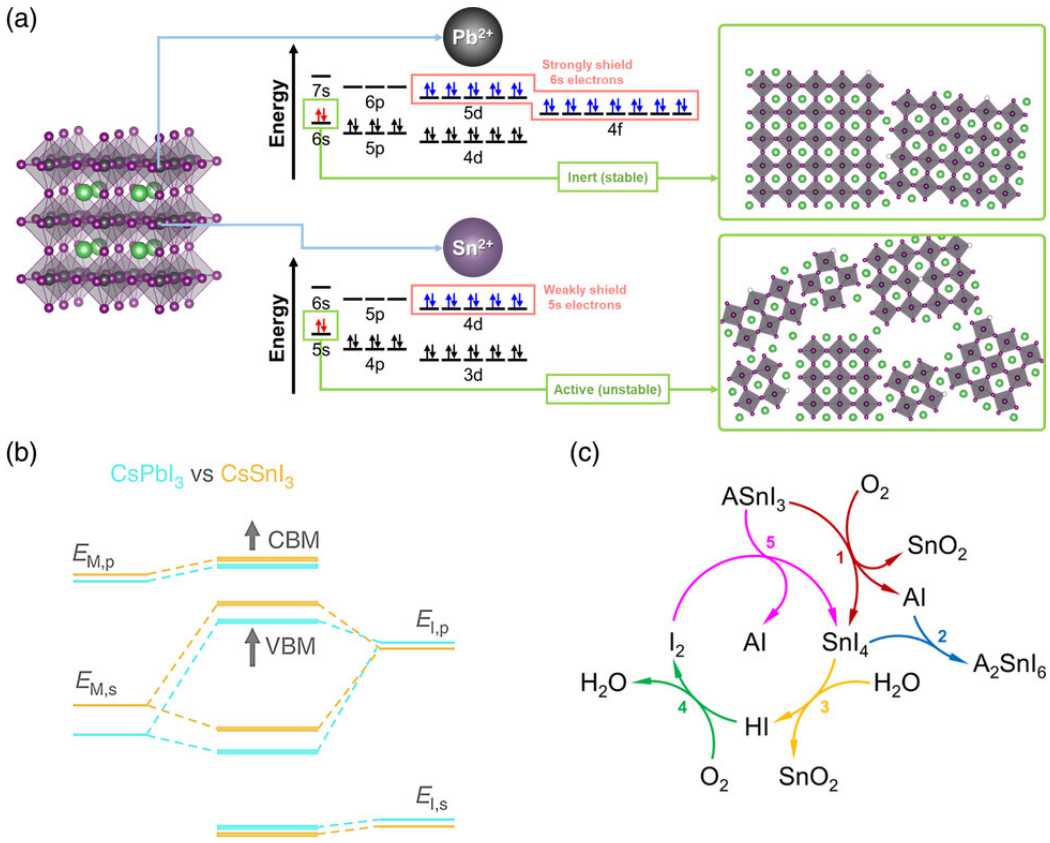

Figure 3.6. a) comparative illustration of the electronic structure between Sn and Pb perovskites and the subsequent effect on the pace of crystallization. b) energy levels of $CsPbI_3$ and $CsSnI_3$. c) possible chemical degradation mechanisms of tin perovskites. Copyright © 2021, Springer Nature.

4. Methods

4.1 Device fabrication:

4.1.1 DMSO-based devices:

PSCs that were manufactured with the following stacking were given an inverted structure as a design option. Glass/ITO/PEDOT:PSS/$FA_{0.78}MA_{0.2}EDAI_{0.02}SnI_3$/$C_{60}$/BCP/Ag make up the material. First, the patterned indium tin oxide (ITO) coated glasses were given a wash in an ultrasonic thermal bath at a temperature of forty degrees Celsius according to the technique as follows: washed in acetone and then sonicated for 15 minutes; washed in ethanol and then sonicated for 15 minutes; dried with a dry air cannon to prevent the formation of stains. This process was repeated four times. Following this procedure, the substrates were placed in a nitrogen-filled glovebox at a temperature of 25 degrees Celsius, where there was less than 0.1 ppm of oxygen and less than 0.1 ppm of water vapor. The substrates were treated with N_2 plasma for ten minutes before the HTL was deposited. After spin coating at 5000 rpm for 30 seconds, diluted Clevious HTL Solar 3 in toluene (1:6 V/V) was applied, and the coating was subsequently annealed at 150 degrees Celsius for ten minutes. Due to the limited wettability of the liquid on the PEDOT surface, 50 L of the perovskite solution was placed on the substrate with a micropipette and distributed with a disposable pipette tip to simulate a blade coating approach. This was done just before beginning the spin coater at 5000 rpm for 45 seconds. As an antisolvent, cyclohexane was utilized, and after 15 seconds from the start of the spin, it was allowed to be released. The perovskite films went through a thermal annealing process for half an hour at a temperature of 100 degrees Celsius. Both the ETL and the silver electrode were deposited in a high vacuum environment (at a pressure of less than 10^{-6} bar) using a thermal evaporation chamber. The thickness of the C_{60} layer was 32 nm, the thickness of the BCP layer was 10 nm, and the thickness of the Ag layer was 120 nm.

4.1.2 DMF:DMI:tBP-based devices:

A solution of SnI_2 in DMF:DMI at a 6:1 volume ratio was prepared with nominal molarity of 1.2 M. The solution was kept under shaking at ambient temperature overnight to dissolve the tin salts completely. The density was checked to calculate the actual molarity of the solution. In a new vial, FAI powder was scaled, and the proper amount of the tin iodide solution was added to the powder using a calibrated micropipette leading to a FA:Sn molar ration of 0.78:1. The solution was kept under shaking for an hour at ambient temperature for the complete dissolution of FAI. The density of the $FA_{0.78}SnI_3$ solution was

measured to calculate the molarity of the solution. In a new vial, MAI and $EDAI_2$ were scaled. The proper amount of the $FA_{0.78}SnI_3$ solution was added to the powder using a calibrated micropipette leading to a FA:MA:$EDAI_2$:Sn molar ratio of 0.78:0.2:0.02:1 molar ratio. The solution was kept under shaking for one hour at ambient temperature to dissolve MAI and $EDAI_2$ completely. The $FA_{0.78}MA_{0.2}EDAI_{0.02}SnI_3$ solution was diluted with tBP in the ratio of 2:1 and kept under shaking for 10 minutes at ambient temperature. For samples obtained by addition of tBP at the beginning of the perovskite solution preparation, the procedure was modified by preparing a 0.9 M nominal solution of SnI_2 instead of the 1.2 M and with a solvent mixture of DMF:DMI:tBP at 6:1:4.5 to consider the solution dilution and the solvents final ratios.

4.2 Hansen solubility parameters:

4.2.1 Fundamentals of Hansen solubility parameters:

Hildebrand and Scott are credited as being the ones who first presented the idea of a solubility parameter, with Scatchard's early work having a significant impact on its evolution. The Hildebrand solubility parameter quickly established itself as the industry standard for this metric not long after it was first developed. It is expressed as the square root of the cohesive energy density, which may be described as $= (E/V_m)^{1/2}$. In this equation, E stands for vaporization energy, and V_m is the molar volume of the pure solvent. These cohesive energies result from the interactions between molecules that share the same solvent[179,180].

The solubility parameters developed by Hildebrand are extensively employed as the standard measure for solubility in a variety of different sectors. They can aid in selecting suitable solvents for coating preparations, predict polymer compatibility, evaluate chemical resistance and penetration rates, and characterize the surfaces of pigments, fibers, and fillers. Miscibility between liquids with comparable solubility properties may be observed, and polymers can be dissolved in solvents with similar solubility parameters. This idea is often expressed using the phrase "like dissolves like." However, a more recent adjustment defines it as "like seeks like," reflecting the different surface characterizations that often do not allow disintegration. In its basic form, solubility parameters express a simple qualitative idea, generating a prediction number for solubility relationships[181,182].

4.2.2 Determination of HSPs for $FASnI_3$:

The determination of Hansen Solubility Parameters for a novel compound, or a compound for which the parameters have not been determined yet, is performed through the following steps:

1) Testing the solubility of the given compound in a large number of solvents. Usually, at least 30-40 solvents are used, but the larger the number, the more robust the analysis. It is essential to define the solubility of interest. In our case, we considered $FASnI_3$ dissolved only if a solution nominally 1M is formed after stirring at room temperature for at least 12 hours (overnight), but different definitions can be adopted. The most rigorous approach is to calculate the solubility limit for every solvent and consider this value in the next steps.

2) Determining the triad of Hansen Solubility Parameters via a numerical algorithm. The definition of the numerical algorithm is the most crucial point, and several have been proposed in the literature[183]. The criteria are usually based on the minimization of the number of outliers (non-solvents inside the Hansen sphere or solvents outside of that), the minimization of the volume of the sphere, or the minimization of a score function named DATAFIT. Combinations of those criteria have been considered.

The DATAFIT function is

$$DATAFIT = \left(\prod_{i=1}^{N} f_i \right)^{1/N}$$

with f_i calculated by:

$$f_i = \begin{cases} e^{(R_0 - R_i)}, & sol = 1; \quad R_i > R_0 \\ e^{(R_i - R_0)}, & sol = 0; \quad R_0 > R_i \\ 1; & \text{otherwise} \end{cases}$$

Here N is the number of the "i" solvents (sol=1) and non-solvents (sol=0), R_0 is the radius of the Hansen sphere (which is a parameter to be optimized), and R_i is the distance of the i-th molecule from the guessed HSPs (the other parameters to be optimized). DATAFIT comprises 0 and 1; it is 1 when all the solvents are within the Hansen sphere and all the non-solvents are outside (a "perfect" solution).

We tested all the algorithms proposed in the literature and, unfortunately, found poor consistency among them, similar to what was reported by others. We also tried to combine the various criteria arbitrarily, but we observed that the results were too dependent on our choice. We believe this is mainly because the solubility of $FASnI_3$ is driven by an aspect poorly described by the Hansen approach, the

complexation of Sn^{2+}. Another reason for the poor performance of Hansen Solubility Parameters is the presence in the solution of different complexes (as repeatedly reported in the case of lead halide perovskites), which would result in the distribution of various Hansen Solubility Parameters.

As an explicative example, the minimization of the DATAFIT score function gave us the HSPs triad (δ_D = 22.4 $MPa^{1/2}$, δ_P = 13.0 $MPa^{1/2}$ and δ_H = 13.6 $MPa^{1/2}$). This point is far from both solvents and non-solvents (see the projection of Hansen space in the δ_D; δ_P plane, where the green open point is obtained from the minimization of DATAFIT), has no physical or practical meaning.

We decided to identify the Hansen Solubility Parameters through the following criteria:

1) We aimed to have the largest Hansen sphere with only solvents inside, i.e. we maximized the distance of the closest non-solvent.
2) We aimed to find the maximum number of solvents within this Hansen Sphere.
3) We aimed to minimize the distance of the farthest solvent outside this Hansen Sphere.

With these criteria, we identify the larger Hansen volume where, the higher number of solvents can be found without any non-solvent, without stepping away from the region where all the experimental points are distributed (as in the case of DATAFIT shown).

4.3 Photoluminescence spectroscopy:

When light comes into contact with a substance, it assimilates photons with higher energy levels than its bandgap. The energy in question induces the movement of electrons from the valence band's highest energy level to the conduction band's lowest energy level. These electrons persist within the material without extraction or experiencing non-radiative recombination. In that case, they will ultimately engage in radiative recombination with a hole, leading to the emission of a photon. The optical phenomenon under discussion is commonly known PL. The photons released during this process cover a range of wavelengths and together constitute what is known as the PL spectrum. Similar to the utilization of integrating spheres in ultraviolet-visible (UV-Vis) measurements, the capturing of emitted photons is frequently facilitated by the implementation of an integrating sphere. The wavelength (λ) associated with the peak in the PL spectrum agrees with the E_g, as stated by the following equation:

$$E = \frac{hc}{\lambda}$$

The relationship between the number of photons emitted (Φ_E) and the number of photons absorbed (Φ_A) is used to determine the photoluminescence quantum yield (PLQY), which serves as an indicator of the

recombination process occurring inside the material. The photoluminescence quantum yield (PLQY) may be mathematically represented in terms of the recombination current as follows:

$$PLQY = \phi_E / \phi_A = J_{rad} / J_G = J_{rad} / J_R = J_{rad} / (J_{rad} + J_{non-rad})$$

In this context, J_G denotes the generation current. At the same time, J_R signifies the total recombination current, which may be further subdivided into the radiative recombination current (J_{rad}) and the non-radiative recombination current ($J_{non-rad}$). At V_{oc} conditions, an equilibrium is established where the net current flow is zero, resulting in the equality of J_G and J_R. Hence, a clear association arises, wherein a reduction in the involvement of non-radiative mechanisms accompanies an increase in PLQY. The non-radiative recombination can be attributed to defects with deep energy levels that effectively capture charges, hence impeding their radiative recombination. An increased PLQY, which suggests a decrease in non-radiative recombination, indicates the existence of high-quality material distinguished by a limited presence of deep traps. An additional understanding of charge recombination and charge collection may be obtained by employing time-resolved photoluminescence measurements (TRPL). These measurements include monitoring the emission of the material over a period of time after the application of a short laser pulse. Moreover, the PLQY provides a method for determining the quasi-Fermi level splitting (QFLS). The QFLS can be expressed as follows. The user did not provide any text to rewrite.

$$QFLS = QFLS_{rad} + K_B T \cdot \ln(PLQY)$$

Where $QFLS_{rad}$ is the radiative limit for the QFLS of the material. This sets the maximum V_{oc} achievable and corresponds to the situation of PLQY = 1, i.e., zero non-radiative recombination. This is a very useful relationship since it allows us to explore the relationship between V_{oc} and QFLS. Overall, PL measurements contain much helpful information. Here, the description has been limited to the analysis directly employed in this dissertation, where PL has been mainly used for deriving the QFLS and monitoring the recombination processes (Chapter 7).

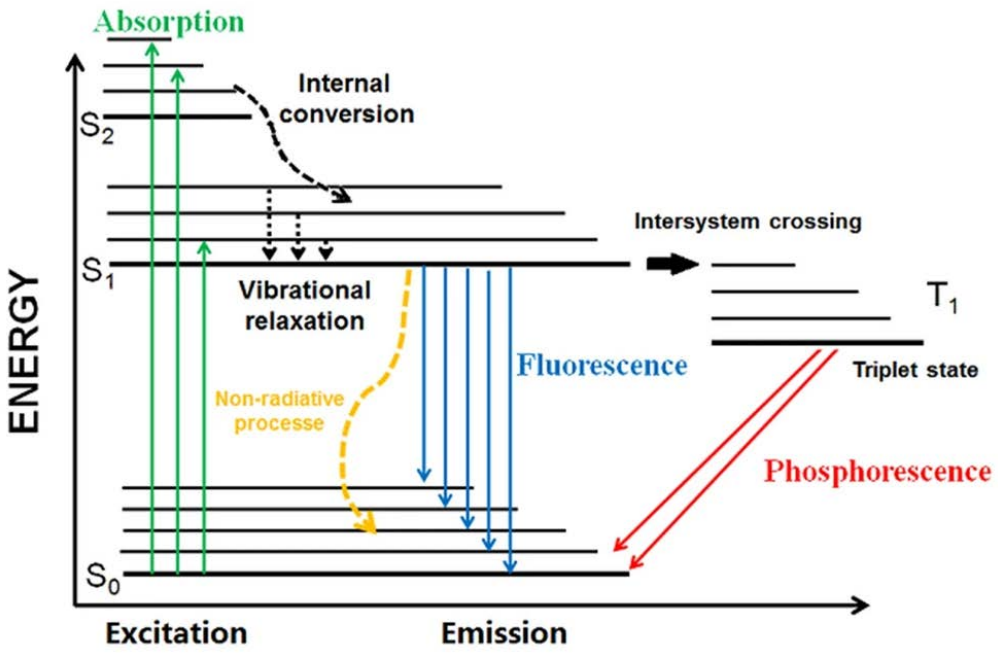

Figure 4.1. Perrin Jablonski illustrative diagram of fluorescence[184]. Copyright © 2021, Springer.

4.4 Photoelectron Yield Spectroscopy (PYS):

Photoelectron yield spectroscopy is a powerful analytical technique that provides valuable insights into materials' electronic properties and surface characteristics. By irradiating a sample with photons of varying energy levels, this method induces the ejection of photoelectrons from the material's surface. These emitted photoelectrons carry information about the material's electronic structure, bonding, and chemical composition. By analyzing the energy distribution and intensity of these photoelectrons, researchers can determine key parameters such as the material's work function, valence band structure, and the presence of surface contaminants. PYS is applicable in various fields, including surface science, materials research, and catalysis, offering a non-destructive and high-resolution approach to unraveling the intricacies of solid surfaces and interfaces.

The experimental protocol entails subjecting the surface of a specimen to controllable UV radiation while simultaneously measuring the released photoelectrons. The relationship between the quantum yield of photoelectrons (Y), the ratio of released photoelectrons to absorbed photons, and the energy of input photons (hν) is explicitly investigated in situations that pertain to materials exhibiting energy gaps. As the energy of the incident photon (hν) gradually increases above the ionization threshold energy (I_{th}), the ionization yield (Y) starts to increase. Therefore, the calculation of the threshold of the spectrum enables the assessment of I_{th}. Likewise, an analogous methodology may determine the sample's work function

within the framework of metal samples. The relationship between the yield spectrum and the threshold portion can be estimated as

$$Y \propto (h\nu - I_{th})_n$$

The value of n depends on the category of materials under examination. For metals, n is equal to 2. Semiconductors exhibit values of 1, 3/2, 2, and 5/2 for n. In the case of organic materials, it is suggested that n should be set to 3. The determination of the threshold may be accomplished by employing linear extrapolation of the Y1/n plot, which is made possible by selecting an appropriate detection system. One notable characteristic of this technology is its versatility, enabling its application in vacuum settings and atmospheric circumstances, distinguishing it from traditional photoelectron spectroscopy. Furthermore, using a sample bias voltage allows for the extension of PYS to highly insulating materials[185].

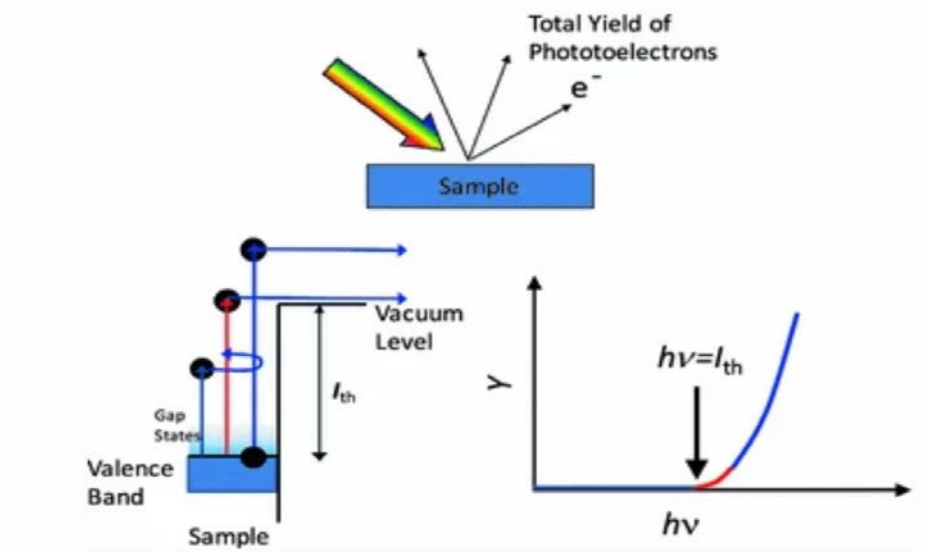

Figure 4.2. The basic principle of PYS[186]. Copyright © 2018, Springer Nature.

4.5 Kelvin Probe:

The KP technique evaluates the WF disparity between two materials that constitute the opposing sides of a parallel plate capacitor[187]. The operational concept of the KP, as illustrated in Figure 4.3 for the scenario involving dissimilar metals, can be outlined as follows. Initially, in Figure 4.2a, the two materials remain separate, maintaining electrical neutrality, with the E_{vac} being shared. Upon connection through an external circuit (depicted in Figure 4.3b), charge migration ensues, flowing from the material with the lower W_F to the one with the higher W_F until equilibrium is established, resulting in an alignment of the E_F. Consequently, an electric field manifests within the gap between the materials, reducing E_{vac}.

This reduction is recognized as the contact potential difference (CPD) and signifies the discrepancy between the W_F of the two metals. While the CPD's value could be readily computed if the capacitance (C) and stored charge (Q) were known—indeed, for parallel plate capacitors,

$$Q = C \cdot V$$

Where V represents the CPD, this issue surrounding CPD determination was ingeniously addressed by Lord Kelvin[188]. His proposal involved the application of an external bias (V_{CPD}) to the system, depicted in Figure 4.2c. When the applied voltage equates in magnitude but opposes the CPD, the capacitor discharges, aligning EVAC, and the distinction between the WF of the materials corresponds to VCPD.

Subsequently, given that the work function of one material (WFP) is known, the calculation of the work function of the second material (WFS) becomes straightforward:

$$V_{CPD} = \Delta_{WF}/e = (WF_S - WF_P)/e$$

In practical terms, determining V_{CPD} involves inducing periodic vibrations in the probe[189]. This approach alters the capacitance between the materials, resulting in changes to the charge within the capacitor and generating a current flow. When the applied voltage precisely matches V_{CPD}, the capacitor discharges, ceasing current flow. The predominant technique for inducing probe vibrations is connecting the electrode to a piezoelectric ceramic[190]. Maintaining the constancy of WF_P throughout the measurement process is crucial, which is why inert materials such as gold (Au) are commonly employed as references. Utilizing a metal probe is particularly reliable because the work function of metals remains unaffected by light, making it well-suited for measuring semiconductors as well. The KP method can be effectively applied to semiconductor samples, extending beyond metals, as exemplified in the case provided for elucidation. The underlying operational principle remains identical, although the semiconductor-metal interface might exhibit band bending. Capitalizing on the probe's inert nature, the KP method enables the measurement of semiconductor work function variations induced by light. In such instances, any shift in work function attributed to light exclusively originates from the semiconductor. The alteration in CPD for a semiconductor subjected to illumination is termed surface photovoltage (SPV). Throughout this dissertation, the KP method has served as the principal tool for characterizing the shifts in energy levels discussed in Chapter 7.

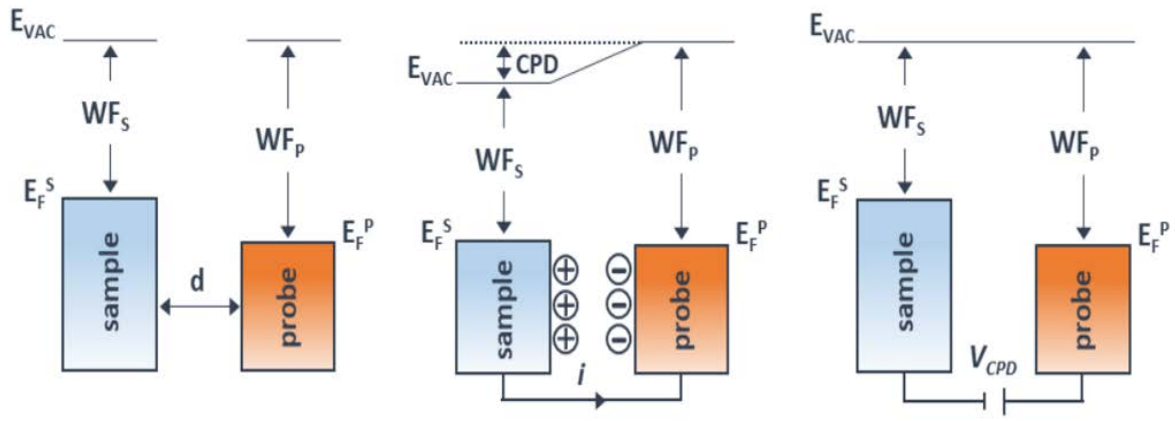

Figure 4.3. The basic working principle of the kelvin probe (KP). Copyright © Uni Potsdam publishing center.

4.6 Surface Photovoltage (SPV):

The SPV method entails the measurement and study of the spectrum dependence of the surface photovoltage phenomenon. The aforementioned technique is robust for characterizing semiconductor materials without intrusive or physical contact. It has shown to be highly successful in assessing a wide range of semiconductor materials. The applications of this technique are wide-ranging and include the determination of many parameters such as semiconductor band gaps, surface potentials, oxide thickness, minority carrier lifespan and diffusion length, impurity concentrations, as well as surface, interface, and defect states. Additionally, this study offers valuable insights into determining band offsets in quantum well architectures, as evidenced by previous research[191,192]. In the present era, the main benefit of this technique is its ability to investigate electronic transitions and optical properties of bulk materials and nanostructures. This is due to its enhanced sensitivity and capacity to function at room temperature, as previous studies showed[193,194]. The adaptability of this approach allows it to be placed in a comparable position to alternative spectroscopic methods such as optical absorption (transmission), photoluminescence (PL), photoluminescence excitation, and electroreflectance spectroscopy.

Significantly, the utilization of SPV obviates the necessity for intricate sample preparation, the construction of contacts, or the formation of junctions. Its usefulness extends to investigating buried layers, deposited thin films, and heterostructures. The primary methods employed for SPV measurements are the Kelvin probe and the metal-insulator-semiconductor (MIS) structure operating modes. Recently, the Management Information Systems (MIS) approach has had a significant surge in popularity and use due to its many advantages[187,195]. This overview concisely summarizes the underlying concepts and experimental setup of the Surface Photovoltage (SPV) technique. The primary emphasis lies in using

SPV to investigate semiconductor materials in optoelectronic applications[196,197]. This study primarily focuses on the outcomes of III-V nanostructures employed as optical emitters and infrared photodetectors. Additionally, it examines Si nanowires and bulk dilute nitride layers, such as Ga(In)As(Sb)N, which have practical applications in solar systems.

5. Solvents for Stable Tin Halide Perovskites

5.1 Introduction:

As their power conversion efficiency approaches that of silicon photovoltaics, halide perovskite photovoltaics are expected to join the market in the near future. The tandem combination of these two technologies exceeded the 30% mark. Recent advances in stability have resulted in longer solar cell lifetimes[198,199], as demonstrated by improvements in interface engineering[200,201,202], perovskite compositional engineering[203,35,204], and appropriate encapsulation[205]. The lightweight and flexible character of metal halide perovskites expands their potential applications to include photovoltaics for wearable[206] and indoor[207] applications. In addition, semitransparent devices are suitable for building-integrated photovoltaics[208] due to their ability to tune the band gap and their high efficiency readily. However, the universal application of perovskite solar cells raises lead toxicity concerns[209]. Although lead sequestration via innovative encapsulation strategies provides some respite[210], the definitive solution would be to replace lead with a less toxic metal, such as tin[211].

Certified tin PSCs efficiencies have recently surpassed 14%[212]. Typically, the most efficient devices use formamidinium tin iodide ($FASnI_3$) and a combination of bulk and surface passivation additives, with SnF_2[76] and phenylethylammonium[213] being the most common dopants and additives. These results demonstrate the high potential of tin halide perovskites in photovoltaic applications while also indicating the existence of fundamental limitations that must be overcome to match the performance of lead-based alternatives. Tin halide perovskites tend to undergo excessive self-p-doping due to the low formation energy of tin vacancies (V_{Sn})[214], which is one of these limitations. In addition, the limited stability of Sn^{2+} leads to rapid perovskite degradation when exposed to even trace amounts of oxygen or water molecules accidentally during film processing[215]. The limited lifetime of photocarriers in tin halide perovskites stems from the chemistry of these defects. During refining, tin perovskites are commonly exposed to reducing agents to prevent the incorporation of Sn^{4+}.

Nevertheless, despite these efforts, the power conversion efficiency frequently remains below 10%, indicating that this approach is not wholly viable and that new strategies should be investigated. The discovery that dimethylsulfoxide (DMSO) oxidizes Sn^{2+} to Sn^{4+}, as reported by Saidaminov et al.[216] and investigated by us[217], represents a significant advancement in this area. It is plausible to hypothesize that the uncontrolled oxidation of tin from the solvent itself during film processing is responsible for the humble development of tin halide perovskite solar cells and the difficulties in reproducibility between laboratories. Consequently, identifying novel, stable, and non-oxidative solvents is crucial for advancing lead-free perovskite solar cells, and this chapter intends to investigate this direction comprehensively.

This chapter analyzes the solubility, stability, and "PerovskitAbility" (i.e., the ability to form $FASnI_3$) of approximately 80 solvents, encompassing all possible functional groups, in terms of solubility, stability, and "PerovskitAbility." We have identified sixteen non-sulfoxide solvents, twelve of which form a stable perovskite precursor solution at 100°C and successfully produce $FASnI_3$. The efficient solution fabrication of tin halide perovskite solar cells begins with these solvents. As evidence, we demonstrate a novel solvent system from which reproducible devices with superior performance to those processed with DMSO can be obtained.

5.2 Finding new solvents for $FASnI_3$:

The aim of developing an extensive list of potential solvents was to test all feasible functional groups thoroughly (Figure A1.1). Special attention was given to dipolar aprotic solvents, such as DMF and DMSO, which possess a strong dipole moment crucial for dissolving ionic compounds like SnI_2 and FAI. In the selection process, we assessed approximately 2000 molecules from various sources and databases[218,219]. Certain classes of molecules were excluded, such as potent acids (due to processability concerns) and aromatic compounds (commonly used as anti-solvents for perovskites, for example, chlorobenzene and toluene). The chosen solvents needed to be liquid at room temperature (with a melting point below 30°C), thereby eliminating large molecules. Likewise, solvents with excessively low boiling points, like methylamine, were ruled out (despite its usefulness in combination with acetonitrile as a solvent mixture for methylammonium lead iodide[220]. Practical considerations, such as commercial availability and safety, were also considered.

5.2.1 Solubility testing protocol:

We defined a molecule as a solvent if it enabled the preparation of a stable solution of $FASnI_3$ with a concentration of over 1M after being stirred or shaken at room temperature for at least 12 hours (overnight). Our solution preparation protocol followed the guidelines outlined in an article by Saliba et al[221]. Initially, we created a stock solution of SnI_2 and then added the appropriate volume to FAI powder, resulting in a SnI_2:FAI solution with a 1:1 stoichiometry. In cases where SnI_2 did not dissolve in the solvent alone, we prepared a stock solution of FAI to facilitate the dissolution of SnI_2. For GBL and sulfolane, a clear $FASnI_3$ solution was obtained only when FAI powder was dissolved first, consistently yielding a slightly below 1M concentration (around 0.8-0.7M). Overall, we identified a total of 17 solvents, which included DMSO.

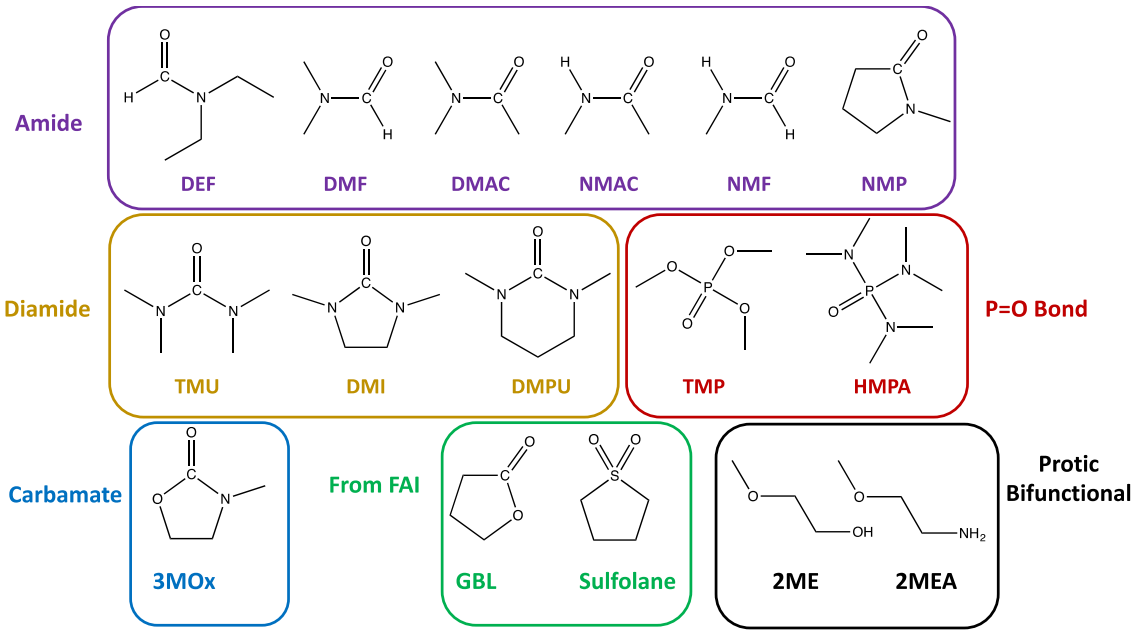

Figure 5.1. The 16 non-sulfoxide solvents that formed 1M solution of $FASnI_3$. Solvents with similar functional groups are grouped and classified by color.

We categorized the solvents into six distinct classes based on the functional group. The most prevalent class consists of amides encompassing DMF and NMP, commonly used solvents for lead halide perovskites. Two closely related classes are diamides (comprising three components) and carbamates (consisting of one component). GBL and sulfolane are grouped together because they form a perovskite solution only when FAI is dissolved first, meaning they dissolve $FASnI_3$ but not SnI_2 at concentrations exceeding 1M. The presence of a P=O bond characterizes another class. Lastly, among the bifunctional molecules, only 2-methoxyethanol (2ME) and 2-methoxyethylamine (2MEA) were helpful; interestingly, these are the only two protic solvents. To elucidate the solubility of $FASnI_3$, we conducted an investigation to explore the correlation between solubility and certain relevant molecular properties.

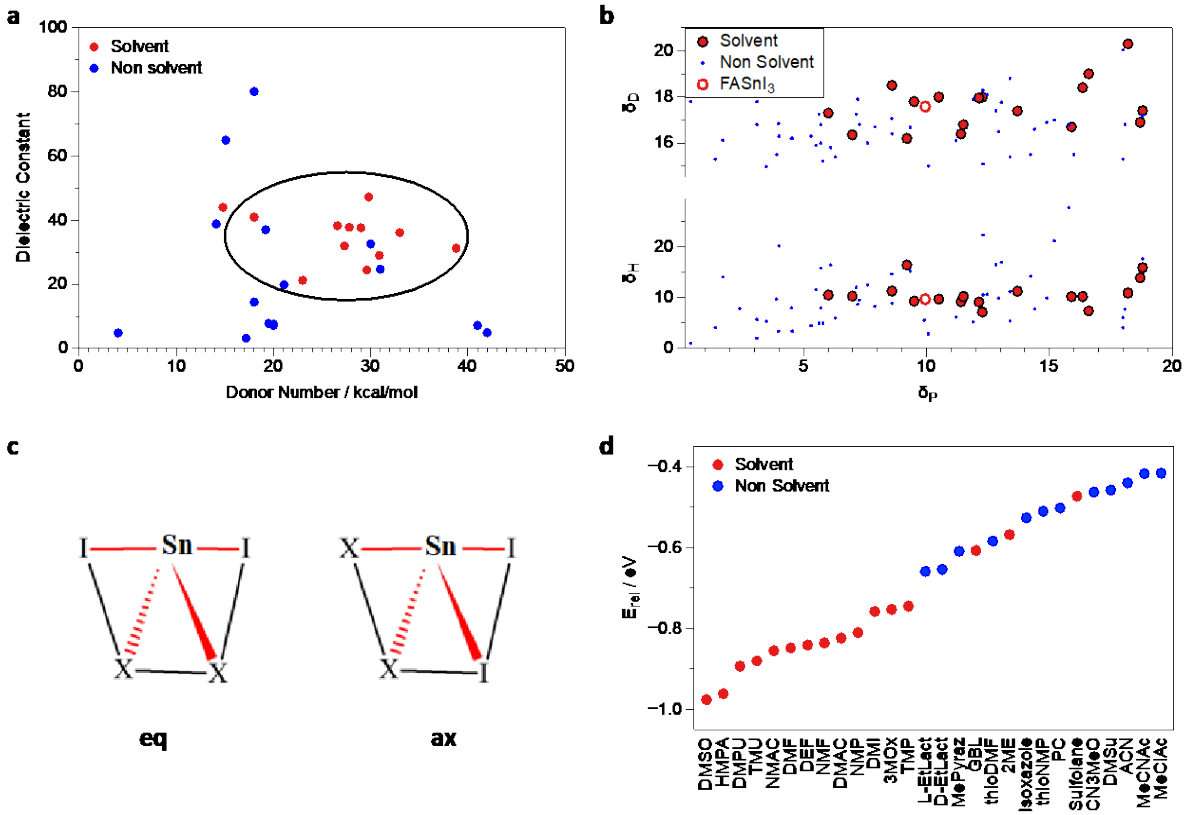

Figure 5.2. $FASnI_3$ solubility in different solvents a) Dielectric constant versus donor number (D_N) plot where the solvents are in red and the non-solvents in blue. Most of the solvents were found to accumulate in a specific area highlighted by the oval frame. b) Plot of Hansen Solubility Parameters (HSPs) of the tested solvents in the δ_D; δ_P and δ_H; δ_P planes. The solvents are in red, and the non-solvents are in blue. c) The geometrical arrangement of SnI_2-$Solv_2$ complexes employed to evaluate the binding energy of the solvents to Sn^{2+} from DFT simulations. d) The value of the binding energies, E_{REL} in eV, obtained from DFT analysis ordered from the higher (in the module) to the lower. The solvents are in red, and the non-solvents are in blue. It is possible to observe a clear correlation between the solubility and the binding energy.

5.2.2 Property activity relationship:

We examined the relationship between solubility and two crucial properties, namely the dielectric constant and the donor number (D_N), which are essential for the dissolution of salts. A high dielectric constant means low coulombic attraction between ions of opposite charges. On the other hand, the D_N indicates a molecule's Lewis basicity, specifically its ability to donate a lone pair to Lewis acids (with $SbCl_5$ serving as the reference). In this context, the D_N reflects the capacity to coordinate a cation in solution. Although we established threshold values for solubility based on these parameters, we did not observe a clear correlation, as demonstrated in Figure A1.2. According to our dataset, a dielectric

constant above 17 or a D_N exceeding 15 kcal/mol is necessary to form a stable solution of $FASnI_3$. However, these values alone are unreliable criteria for determining whether a molecule can act as a solvent.

Interestingly, when considering both parameters together, it is intriguing to note that there is a region in which most solvents tend to cluster, as illustrated in Figure 5.2a. Focusing on these specific physical parameters could potentially facilitate the identification of novel solvents. However, the impracticality arises from the limited availability of D_N values in the literature[219]. A more viable alternative is the utilization of Hansen Solubility Parameters (HSPs)[222], which offer a vast library encompassing approximately 10,000 molecules along with methods to calculate or measure the HSPs of new compounds. The Hansen approach assigns three parameters (HSPs) to a molecule, denoted as δD (dispersion interactions), δP (dipolar interactions), and δH (hydrogen bonding), all measured in $MPa^{1/2}$. Treating the HSPs as Cartesian coordinates in "Hansen space" makes calculating a "distance" between molecules possible. The closer two molecules are in Hansen space, the higher the probability of mutual solubility. Moreover, it is feasible to extract the HSPs for a new compound by analyzing the distribution of its solvents and non-solvents in Hansen space, with the aim of finding a triad of HSPs that minimizes the distance to solvents while simultaneously maximizing the distance to non-solvents. However, this is a nontrivial task, and various algorithms have been proposed in the literature to determine the HSPs[183].

For $FASnI_3$, we obtained the following Hansen solubility parameters: δD = 17.6 $MPa^{1/2}$, δP = 9.9 $MPa^{1/2}$, and δH = 9.7 $MPa^{1/2}$. More detailed discussion and analysis can be found in Figure A1.4a. In Figure 2b, we present the projections of the Hansen space onto the δD; δP and δH; δ_P planes. It is evident that the HSPs obtained for $FASnI_3$ are closer to most solvents than non-solvents, although there are some exceptions. To clarify further, Figure A1.4a and A1.4b demonstrates the distance to $FASnI_3$, showing that solvents are the only substances within a threshold of 3 $MPa^{1/2}$. Targeting this region could serve as a valuable guideline for the discovery of new solvents or solvent mixtures. Notably, several solvents that exhibit a greater distance to $FASnI_3$ display peculiar behaviors: sulfolane and GBL require the presence of FAI to dissolve SnI_2, trimethyl phosphate forms a transparent solution indicating the formation of unusual complexes, and 2-methoxyethanol is the only bifunctional solvent that is also protic by nature. In conclusion, NMF and NMAC possess the unique characteristic of having an N-H bond, which allows for the potential formation of hydrogen bonds. While it is possible to provide explanations for the exceptions observed in our Hansen analysis, it is crucial to consider that this method was originally designed to account for the solubility and drying of polymers[222]. It has been noted that HSPs may have limitations in describing coordinative bonds between solvents and ions[223]. Consequently, we proceeded to investigate the binding energy of solvents and certain non-solvents with Sn^{2+} using Density Functional Theory (DFT).

We calculated this energy as the relative formation of SnI_2-solvent complexes, E_{rel}, which is:

$$E_{rel} = \frac{E_{tot} - E_{SnI_2} - E_{solv} * n}{n}$$

Where E_{tot} is the energy of the complex comprising SnI_2, while E_{SnI_2} and E_{solv} are the energies for SnI_2 and the non-interacting solvent, respectively.

Our focus was on two specific solvent molecules (n=2 in equation 1), and we examined various geometries for two distinct configurations of SnI_2, where the I-Sn-I angle takes values of approximately 180° (axial configuration, labeled as "ax") and 90° (equatorial configuration, labeled as "eq"). We selected only the most stable configuration, as depicted in Figure 2c. In Figure 2d, we present the relative binding energies (E_{rel}) for the evaluated solvent molecules and discovered a remarkable correlation with solubility[224]. This finding emphasizes that the complexation of Sn^{2+} ions may be the most prominent mechanism for dissolving $FASnI_3$. Interestingly, GBL and sulfolane exhibit relatively lower binding energies and greater distances in Hansen space from $FASnI_3$. This trend suggests that, for these two solvents, the solubilization of $FASnI_3$ follows a different pathway compared to the other solvents. This observation aligns with the requirement of initially dissolving FAI to achieve a stable ink solution.

5.3 The ability to form a perovskite structure of new solvents:

The most straightforward method to assess the efficacy of a precursor solution in forming perovskite is through the thermal annealing of the solution, drop-casted onto a glass substrate. In our experiment, we utilized a thermal ramp with a rate of approximately 12°C per minute, starting from 30°C and reaching 150°C, at which point the temperature was held constant. The entire experiment had a duration of 20 minutes. Upon completion of the thermal treatment, we observed the absence of perovskite formation from two solvents: 2-methoxyethylamine and trimethyl phosphate (corresponding to solvents 1 and 10, respectively, in the pictures shown in Figure 3b). We hypothesize that 2-methoxyethylamine inhibits perovskite formation due to acid-base competition for protons with formamidinium, aligning with the analysis conducted by Noel et al. concerning the ACN/amine solvent system for $MAPbI_3$, particularly for amines larger than methylamine. In the case of trimethyl phosphate, it is possible that the solvent irreversibly removes iodide from the Sn^{2+} complex, as suggested by the transparent appearance of the solution[220].

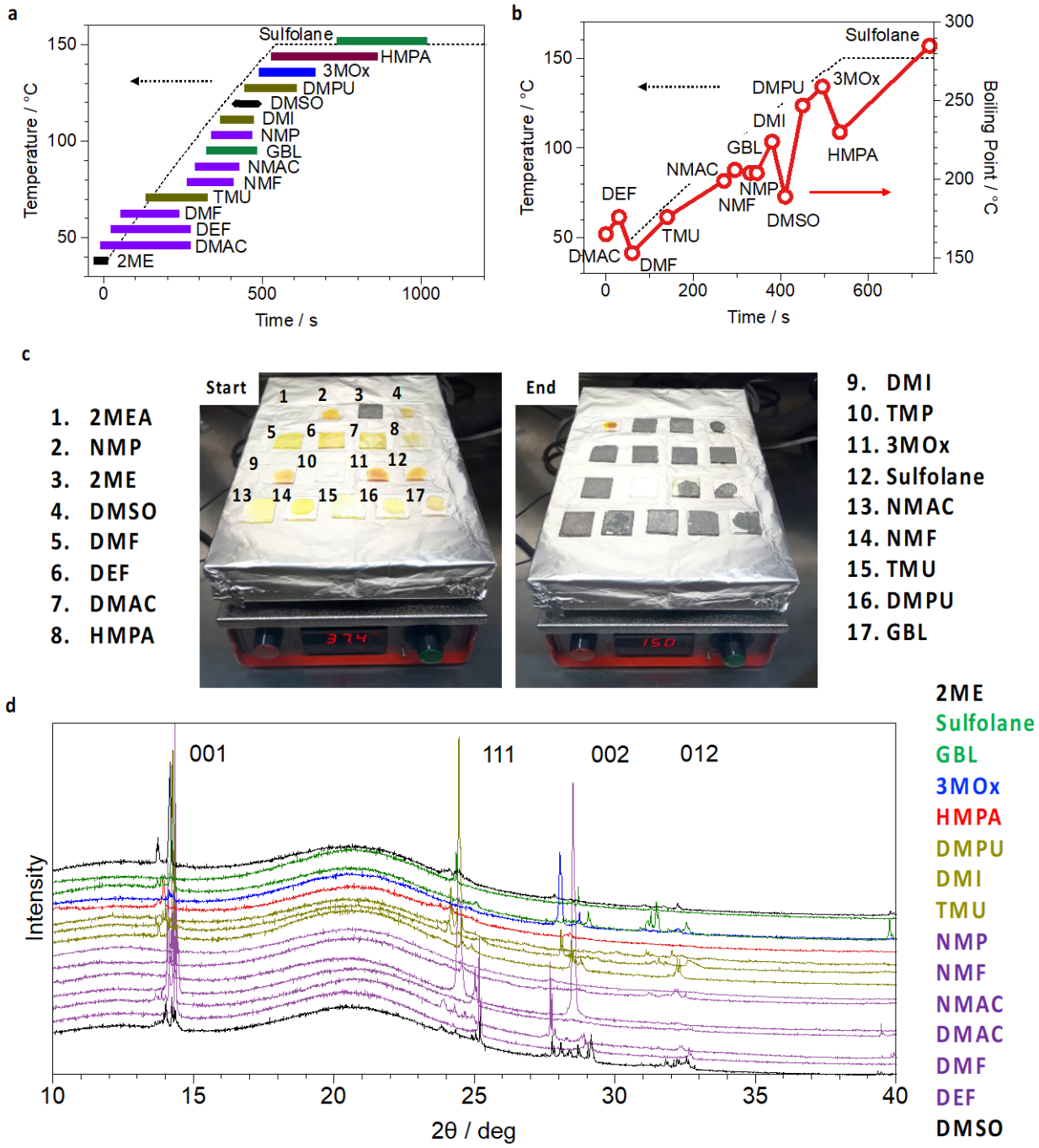

Figure 5.3. The possibility to form $FASnI_3$. a) Plot of temperature (°C) versus time (in seconds) where the dashed line indicates the temperature of the hotplate during the drop-casting experiment performed to test the possibility to form perovskite from a 1M $FASnI_3$ precursor solution. For each solvent that forms perovskite, we introduce a bar indicating the beginning and end of the perovskite formation as revealed by the extended version of the video in supporting information. b) Same graph as a) where for every solvent the beginning of the perovskite formation versus the boiling point (Tb) is plotted, which shows a clear correlation between these two parameters. c) Time-laps shots from the video in the supporting information of the drop-casting experiments. It is possible to see that 15 out 17 solvents (including DMSO) form perovskite. d) XRD of the films obtained via drop-casting from the 15 solvents

(including DMSO). The position of main $FASnI_3$ peaks as obtained from literature research is indicated with light blue bars.

Figure 5.3a illustrates the time window for perovskite formation from the various solvents. Notably, 2-methoxyethanol is capable of forming perovskite even at temperatures below 40°C, while in the case of sulfolane, perovskite formation initiates after a few minutes at 150°C. In Figure 5.3b, we demonstrate a clear correlation between the boiling point (T_b) of the solvents and the time of perovskite appearance, indicating that solvent evaporation serves as the primary driving force for perovskite formation in this experiment. It is worth mentioning that DMSO and HMPA slightly deviate from this trend, as they exhibit higher binding energy to Sn^{2+}, as revealed by DFT calculations. X-ray diffraction (XRD) analysis were performed on the obtained films to confirm the formation of perovskite, as illustrated in Figure 5.3d. For all samples, we detected peaks consistent with the crystal structure of $FASnI_3$ [225,226,227]. It should be noted that most of the samples exhibited low crystallinity and the presence of multiple phases (such as different phases of $FASnI_3$ or compounds involving the solvent, as described in Figure A1.6). Depending on the specific deposition method, these aspects will require optimization in thin film processing.

5.4 Thermal stability of the new perovskite precursors

We also investigated the thermal stability of the perovskite precursor solutions by subjecting them to a stress test at 100 °C for 3 hours. In previous studies, we demonstrated that under these conditions, DMSO triggers the oxidation of Sn^{2+} to Sn^{4+}, which can be detected by a distinct color change of the solution (from yellow to dark red) and through ^{119}Sn NMR spectroscopy[228]. However, for all the identified solvents in our study, we observed no change in the color of the solution (as shown in A1.5) nor the appearance of Sn^{4+} signals in the NMR spectra. This trend confirms sulfoxide as the oxidizing functional group, as observed for methyl phenyl sulfoxide and diphenyl sulfoxide. Apart from tin oxidation, we utilized ^1H NMR and ^{13}C NMR spectroscopy to investigate potential alternative chemical side reactions involving formamidinium or the solvents themselves. NMR spectra were measured for 1M solutions of SnI_2 and $FASnI_3$ before and after heating at 100°C for 3 hours for all identified solvents. A graphical representation of the chemical shift variations for ^1H, ^{13}C, and ^{119}Sn can be found in Figure 5.4a. We propose a detailed discussion on the variation in chemical shifts for future work and focus solely on the identification of degradation pathways in this manuscript.

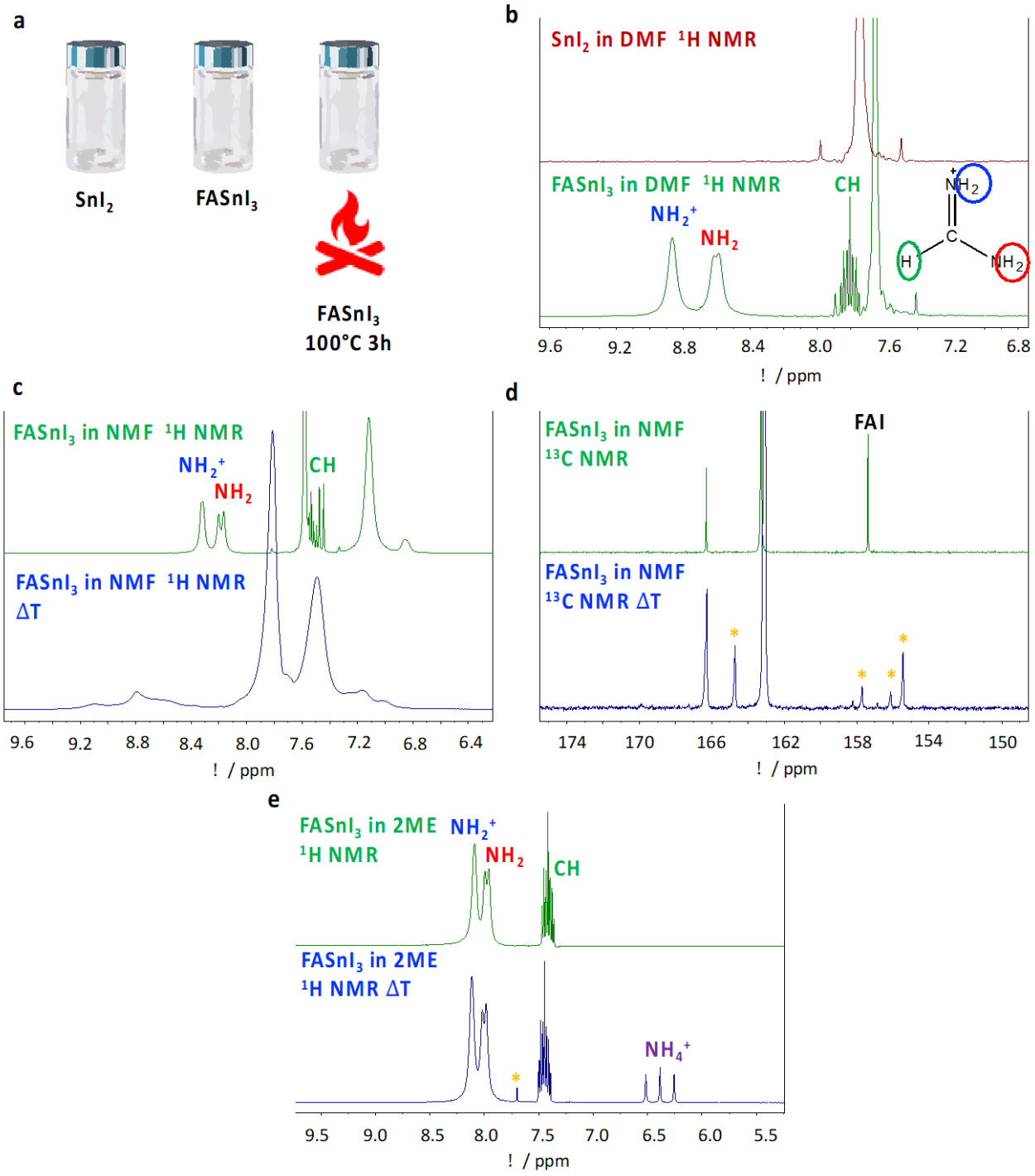

Figure 5.4. The stability of $FASnI_3$ solutions a) The three samples analysed to assess the thermal stability of the perovskite precursor solutions: SnI_2, $FASnI_3$ and $FASnI_3$ heated at 100°C for 3 hours (in supporting information SI4 the pictures for last two samples). **b)** ^1H NMR spectra for SnI_2 and $FASnI_3$ solutions in DMF as a reference to show the peak assignment related to formamidinium. **c)** ^1H NMR for $FASnI_3$ solution before and after heating at 100°C for 3 hours in NMF which offer a significant change in the spectrum shape after heating. **d)** ^{13}C NMR for the same samples as in **c)** which shows the loss of the peak attributed to formamidinium and the appearance of 4 new (unidentified) peaks after heating. **e)** ^1H NMR

for $FASnI_3$ solution before and after heating at 100°C for 3 hours in 2ME which show the appearance of ammonium and an unnamed new peak after heating.

In Figure 5.4b, we present the ^1H NMR spectrum for SnI_2 in DMF, where only the peaks corresponding to DMF are observed. Similarly, for $FASnI_3$ in the same solvent, we clarify the attribution of peaks to the NH^{2+}, NH_2, and CH protons of formamidinium. By comparing the NMR spectra of $FASnI_3$ solutions before and after thermal stress, we identified N-methylformamide (NMF) and 2-methoxyethanol (2ME) as the only two unstable solvents. Figure 5.4c illustrates this comparison for NMF, revealing a noticeable change in the spectrum shape after heating. Unfortunately, interpreting the ^1H NMR spectrum alone does not allow for a clear identification of the reaction pathway. However, from the ^{13}C NMR spectra of the same samples shown in Figure 5.4d, we observe the disappearance of the signal associated with formamidinium and four new signals' appearance. This observation suggests the degradation of the formamidinium cation and the formation of different compounds with overlapping ^1H NMR spectra that are not easily resolved. We also observed similar signal broadening in the ^1H NMR spectrum of DMF, but without losing the original spectral shape or the appearance of new signals, leading us to conclude that DMF remains stable under these conditions. Additionally, in Figure 4e, we demonstrate that thermal stress on the solution of $FASnI_3$ in 2-MEA leads to the formation of NH^{4+}, as indicated by the appearance of a characteristic triplet centered at δ 6.4[229].

Based on the NMR analysis, we can exclude two additional molecules from the initial set of 16, resulting in a final selection of 12 non-sulfoxide solvents that form clear and thermally stable perovskite precursor solutions, enabling the formation of $FASnI_3$ through thermal annealing between room temperature and 150°C. It should be noted that the degradation processes observed primarily involve the formamidinium cation and, therefore, are not relevant in the case of inorganic perovskites (such as $CsSnI_3$). Subsequently, we provide a table containing all the pertinent properties for this chapter´s 12 identified solvents (along with DMSO for comparison).

Name (CAS)	**M_W g/mol**	**δ g/cm^3**	**T_m °C**	**T_b °C**	**η cP**	**ϵ_r**	**μ D**	**DN. kcal/mol**	**HSPs $\delta_D, \delta_P, \delta_H$**	**E_{REL} (DFT) eV**
DMF 68-12-2	73.09	0.94	-61	153	0.92	38.25	3.86	26.6	17.39 13.7 11.25	-0.848
DEF 617-84-5	101.15	0.91	--	177	--	29.02	3.99	30.9	16.4 11.4 9.2	-0.841
DMAC 127-19-5	87.12	0.94	-20	165	2.14	37.78	3.72	27.8	16.8 11.5 10.2	-0.824

TMU 632-22-4	116.16	0.97	-1	177	1.50	24.46	3.47	29.6	17.3 6.0 10.5	-0.880
NMAC 79-16-3	73.09	0.96	27	206	--	179	4.12	--	16.9 18.7 13.9	-0.855
GBL 96-48-0	86.09	1.05	-44	204	1.70	40.96	4.27	18	19 16.6 7.4	-0.607
NMP 872-50-4	99.13	1.03	-24	204	1.67	32	4.02	27.3	18 12.27 7.16	-0.810
DMI 80-73-9	114.15	1.06	8.2	224	1.94	37.6	2.64	29	18 10.5 9.7	-0.758
DMPU 7226-23-5	128.18	1.06	-20	247	2.95	36.12	4.17	33	17.8 9.5 9.3	-0.893
3MOx 19836-78-3	101.11	1.17	15	259[36]	2.48	77.5	5.0	--	18.0 12.1 9.1	-0.753
HMPA 680-31-9	179.20	1.03	7	230	3.25	31.3	5.38	38.8	18.5 8.6 11.3	-0.961
Sulfolane 126-33-0	120.17	1.26	25	285	10.3	44	4.68	14.8	20.3 18.2 10.9	-0.473
DMSO 67-68-5	78.13	1.10	19	189	1.99	47.24	3.96	29.8	18.4 16.36 10.23	-0.976
Name (CAS)	**M_W g/mol**	**δ g/cm^3**	**T_m °C**	**T_b °C**	**η cP**	**ϵ_r**	**μ D**	**DN. kcal/mol**	**HSPs $\delta_D, \delta_P, \delta_H$**	**E_{REL} (DFT) eV**

5.5 Thermal stability of the new perovskite precursors

Undertaking a systematic investigation to determine the optimal solvent system for producing high-efficiency solar cells is a formidable task. When considering pure solvents and binary mixtures alone, there are a total of 78 possibilities (12 pure solvents and 66 combinations) without even considering the variations in the molar ratio of the solvents within each binary mixture. Moreover, suppose we also account for crucial experimental parameters such as perovskite concentration, precursor stoichiometry, spin coating ramp, antisolvent dripping, and thermal annealing. In that case, it becomes apparent that conducting a comprehensive analysis is unfeasible. Nonetheless, we did assess the spin-coating

deposition of $FASnI_3$ from each pure solvent and several mixtures. Regarding pure solvents, we achieved the best film quality and device performance using DMF (Figure A1.7). However, the most effective solvent system we obtained was a mixture of DEF and DMPU with a volume ratio of 6 to 1. As depicted in Figure 5.5a, the DEF:DMPU mixture allowed us to achieve the typical perovskite morphology with grain sizes in the range of hundreds of nanometers. To assess the optoelectronic quality of the $FASnI_3$ film, we fabricated solar cells using the ITO/PEDOT:PSS/$FASnI_3$/C_{60}/BCP/Ag configuration. Devices processed with the DEF:DMPU solvent mixture exhibited power conversion efficiencies exceeding 6% (V_{OC} = 0.533 V, J_{SC} = 21.9 mA cm^{-2}, FF = 53%, PCE = 6.2%). In contrast, devices using perovskite processed from DMSO showed significantly lower efficiencies, typically below 4% (V_{OC} = 0.490 V, JSC = 14.8 mA cm^{-2}, FF = 52%, PCE = 3.84%). Results from over 30 devices are provided in the supporting information (SI8), which confirms the improved performance and reproducibility achieved with the DEF:DMPU mixture. Importantly, it should be noted that these results were obtained without the inclusion of any additives (such as SnF_2, metallic tin, or 2D cations)[76,213] or reducing agents[198,199]. This demonstrates that eliminating DMSO and finding a suitable alternative is advantageous for fabricating tin halide perovskite solar cells.

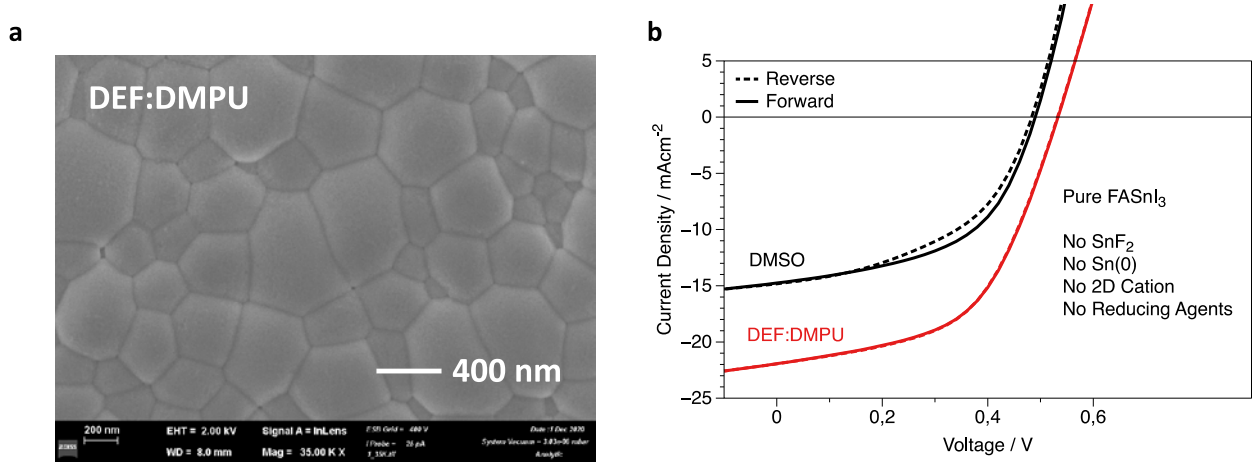

Figure 5.5. $FASnI_3$ films and devices from DEF:DMPU solvent system. a) SEM top view obtained for the $FASnI_3$ thin film spin-coated from a DEF:DMPU solvent mixture **b)** *JV* curves for solar cells comprising $FASnI_3$ thin film processed from DMSO (black lines) and DEF:DMPU (red lines). We remark that these devices are fabricated without introducing any passivating agent or additive, which usually leads to non-working devices.

6. Pyridine-Controlled Tin Perovskite Crystallization

6.1 Introduction:

Metal halide perovskites are crystalline materials with outstanding optoelectronic properties that can revolutionize photovoltaics by reducing costs and simplifying manufacturing[203,230,231]. Lead-based perovskites have already demonstrated the capacity to compete with silicon in terms of efficiency in lab-scale devices (reaching 26% at the time), indicating that they are on their way to becoming a viable alternative[232,14]. However, the commercialization of these products has been hampered by worries regarding their long-term stability and lead toxicity.[233,234,235,236,209,237,238,239].

Tin, which is less hazardous to the environment and potentially more effective than lead, is currently being investigated as a potential replacement for lead in high-efficiency PSCs[209]. Due to their reduced bandgaps, lead-free tin halide perovskites, also known as THPs, are suited for high efficiency in single-junction solar devices. For example, $FASnI_3$ with a band gap of 1.35 eV can deliver a theoretical PCE of over 30% according to shockly-queisser limit[240]. However, the most efficient certified device only achieves 14.8% efficiency[241,242]. In order to improve the performance of THPs, it is necessary to address the following three primary challenges: maximizing energy band alignment with Charge transport layers (CTLs)[243], lowering the rate of crystallization[244], and preventing the undesirable oxidation of Sn^{2+} to Sn^{4+}. As a result of its favorable interaction with perovskite precursors, which slows down the crystallization process[245], DMSO is commonly employed as a solvent for preparing lead and tin perovskite thin films. However, it has been discovered that DMSO exhibits an undesired oxidizing behavior when combined with iodide salts, which increases the concentration of Sn^{4+} in the precursor, and triggers a self-P-doping mechanism in the perovskite film[246,216]. In order to find an alternative to DMSO that does not oxidize Sn, we investigated and screened a broad group of solvents and introduced the results in Chapter 5[247]. The process of selecting new solvents for THP processing is intricate due to the need to consider various factors pertaining to the chemical and physical properties of the solvents. These factors include the solubility of the precursors, the vapor pressure of the solvents, and the ability to form stable complexes with both the organic and inorganic components of the salts[248]. As a result, we propose the introduction of a co-solvent that can work as a mediator between SnI_2 and the solvent molecules. Pyridines, particularly 4-(tert-butyl) pyridine (tBP)[249,250], have shown potential as an additive to lead halide perovskites. They form stable complexes with Sn^{2+} and Sn^{4+} halides by coordinating Sn in

SnI_2 and N in pyridine, regulating the crystallization dynamics and enhancing the microstructure of the perovskite films[251].

In this chapter, we present that tBP can form stable organo-metal complexes with tin iodide salts in solutions that do not contain DMSO. As a result, the crystallization process of THP thin films is facilitated, and the possibility of Sn^{2+} oxidation to Sn^{4+} is mitigated. An in-depth investigation of the precursor solution chemistry indicated that the capability of tBP to bind to Sn^{2+} stabilizes colloidal perovskite nanoparticles, ultimately resulting in a stable intermediate phase that slows down the crystallization dynamics of THPs. As a consequence of this effect, the improved microstructure of THP thin films showed increased hole mobility and lowered defect density. It attained a PCE of 7.3%, the highest value reported for DMSO-free THP solar cells based on solution processing. This study reveals that it is possible to successfully manage the crystallization of THPs without relying on DMSO. As a result, there is no longer any cause for concern over the presence of oxidants throughout the fabrication process.

6.2 tBP as a Co-crystallization additive:

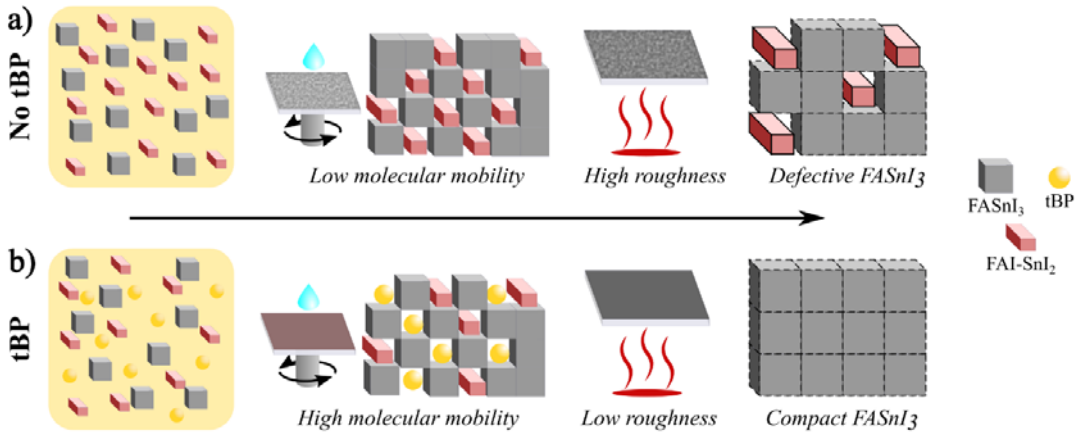

Figure 6.1. Graphical illustration of the perovskite thin film formation. (a) without tBP, and (b) with tBP

As demonstrated in prior research, the process of dissolving perovskite precursor salts in solvents triggers the dynamic generation of diverse colloidal nanoparticles (NPs)[252,253]. The colloidal nanoparticles function as the initial catalyst for the nucleation and subsequent growth of perovskite grains in the spin coating procedure. These colloidal solutions' chemical composition and stability are paramount in regulating the quality of the resultant perovskite thin film. In the context of THP, the rapid nucleation

and growth of colloids in this scenario result in low-quality morphology and incomplete conversion of SnI_2 into the perovskite phase, as illustrated in Figure 6.1a. These factors have a negative impact on the overall performance of the device.

During solution spincoating, a substantial quantity of the solvent evaporates from the liquid film, forming larger and more stable nuclei for the colloidal nanoparticles. The addition of the antisolvent triggers a rapid increase in the concentration of the solution beyond its saturation point, resulting in almost instantaneous formation and enlargement of THP grains. The fast kinetics of the system impedes the diffusion and reconstruction of SnI_2 clusters, thereby hindering the transformation into the perovskite phase. This leads to a suboptimal microstructure, as evidenced by the opaque surface finish observed in Figure A 2.1a.

In order to decelerate the crystallization dynamics in THPs, we utilized tBP as a co-solvent. It exhibits a high affinity towards SnI_2, as demonstrated by forming robust and enduring intermediate complexes, as depicted in Figure 6.1b. Furthermore, tBP exhibits a degree of retention within the wet film throughout the spin coating procedure. Consequently, the duration of the crystallization process is expanded, leading to a gradual alteration of the color of the THP film from a partially transparent red-brown to a brown-black shade. This transformation occurs over approximately 20 seconds subsequent to the antisolvent dripping, producing a smooth and reflective appearance (Figure A 2.1b).

The annealing process exerts differential effects on the two films. Films that were not treated with tBP exhibit minimal alterations in their visual characteristics upon annealing, suggesting that the crystallization process had already finished during the spin-coating stage. In contrast, it can be observed that films treated with tBP exhibit a significant decrease in transparency and an increase in darkness during the annealing process. This phenomenon implies that tBP molecules within the film establish robust connections, necessitating further energy input for removal from the system.

6.3 The mechanism of tBP co-crystallization:

The utilization of Scanning Electron Microscopy (SEM) imaging provides empirical evidence that there is a significant improvement in the morphology of THP films, as depicted in Figure 6.2a. When tBP is not included in the precursor solution, the average grain size is estimated at around 200 nm (Figure 6.2a, left). Additionally, the coverage of the substrate is not complete due to the existence of pinholes. Nevertheless, introducing tBP results in a notable increase in grain sizes of THP films, with a range of 500 nm to 1 µm observed (Figure 6.2a, right). The observed enhancement can be attributed to the decelerated nucleation and crystallization kinetics facilitated by tBP.

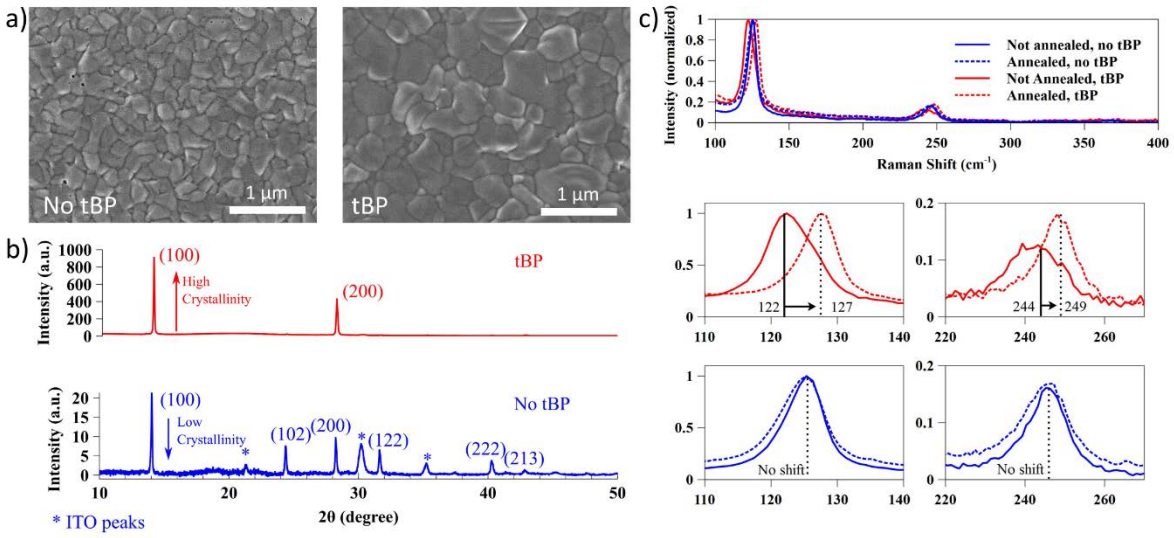

Figure 6.2. Microstructure characterization of perovskite thin films treated with and without tBP. (a) SEM images clearly show the impact of tBP on the grain size and the morphology of the prepared films, and (b) XRD signals show the high crystallinity of the tBP-treated films. (c) Raman spectra indicate the change in the vibrational modes of the films under investigation upon the addition of tBP before and after annealing.

The validation of enhanced crystallinity is further supported by conducting X-ray Diffraction (XRD) measurements, as shown in Figure 6.2b. The X-ray diffraction (XRD) pattern obtained from the tBP-free $FASnI_3$ film exhibits six distinct peaks that can be attributed to specific crystallographic planes, namely (100), (102), (200), (122), (222), and (213). These peaks provide evidence for the presence of an orthorhombic crystal structure in the film. The observed pattern implies that the tBP-free $FASnI_3$ films exhibit a composition comprising nanocrystals arranged randomly. Nevertheless, the inclusion of tBP results in a notable enhancement of the (100) and (200) facets, whereas the absence of the (102), (122), (222), and (213) facets is observed in tBP-free $FASnI_3$ films. The presence of the (100) and (200) facets indicates the potential existence of a highly oriented crystal film, where the crystals align preferentially along these planes. Alternatively, it may suggest higher crystallinity in the $FASnI_3$ films[242].

We used Raman spectroscopy to examine the influence of tBP during the annealing process comprehensively. In Figure 6.2c, the Raman spectra of THP thin films were recorded before and after thermal annealing. The samples were divided into two groups: one from the control solution and the other from a solution diluted with tBP. An apparent peak, located within the spectral range of 120 – 128 cm^{-1}, was detected in all spectra, which could be attributed to the reticular cage modes resulting from the collective stretching vibrations of the Sn-I bonds within the crystal lattice[254,255]. It proves the structural

order of the tBP-treated perovskite films. It has been suggested as a means of assessing the consistency and uniformity of deposited layers and exploring fundamental attributes such as the thickness of the film, density of defects, composition, and stability[256].

A notable band within the spectral range of 240 – 248 cm^{-1} can be ascribed to the methylammonium cation. More specifically, this band corresponds to a torsional mode exhibited by the fragment within the cage-like structure, which makes the band broader than that at 120 - 130 cm^{-1}. The object's shape and Full Width at Half Height (FWHH) can be influenced by interactions with the surrounding environment, especially in the presence of structural defects, resulting in a non-uniform environment. Consequently, the interaction generates a band that exhibits increased width and forms a multi-component structure. Due to the aforementioned attributes, we used this feature as an indicator for the orientational disorder of the material[255].

When comparing the Raman spectra of $FASnI_3$ with those of related materials such as Pb halide perovskites[255,256], it is evident that the spectra demonstrate a noteworthy level of narrowness and enhanced resolution. In a conventional lead iodide system, an intricate multi-component profile is centered at 120 cm^{-1} and exhibits a Full Width at Half Height (FWHH) of 50 cm^{-1}. Nevertheless, in $FASnI_3$, the peak observed at 120 – 130 cm^{-1} exhibits a significantly narrower width, approximately one order of magnitude smaller (FWHH = 5 – 6 cm^{-1}). This observation suggests the presence of a highly organized crystal structure characterized by a minimal amount of defects induced by degradation. Comparably, the lead-based system exhibits a band consisting of four components at a wavenumber of 250 cm^{-1}, characterized by a full width at half maximum (FWHH) of approximately 70 cm^{-1}. Conversely, our data demonstrate a solitary Gaussian peak ranging from 240 to 248 cm^{-1}, with an FWHH spanning from 9 to 11 cm^{-1}.

The findings of this study provide compelling evidence for the existence of a highly organized crystalline arrangement characterized by a limited occurrence of degradation-induced imperfections. Upon examination of Figure 6.2c, it becomes apparent that the control film (indicated by the blue lines) exhibits consistent peak positions at 125 and 246 cm^{-1} prior to and subsequent to the annealing process. This suggests that the process of THP crystallization reaches its conclusion during the spin coating stage, in conjunction with the addition of the antisolvent through dripping. As a result, the annealing process does not lead to any substantial structural modifications in the crystals.

In contrast, when THP is prepared using tBP and subjected to annealing, the peak initially located at 121 cm^{-1} undergoes a shift towards a higher frequency of 6 cm^{-1}. Additionally, it becomes noticeably narrower, with the full width at half height (FWHH) decreasing from 9 to 6 cm^{-1}. The torsional mode exhibits a comparable phenomenon, wherein its position undergoes a displacement from 244 to 249 cm^{-1}, accompanied by a reduction in the full width at half maximum (FWHM) by 9 cm^{-1} (from 18 to 9 cm^{-1}). The aforementioned observations provide compelling evidence that the annealing procedure

conducted in the presence of tBP leads to a substantial reorganization of the lattice structure, thereby amplifying the degree of order in the crystals.

In order to acquire a theoretical understanding of the mechanism of complexation between SnI_2 and different solvents such as tBP, DMSO, DMF, and DMI, we performed quantum chemical calculations. The present study involved an investigation of complexes formed between SnI_2 and various solvents (tBP, DMI, DMF, DMSO), with stoichiometries of both 1:1 and 1:2. These complexes were subsequently incorporated into a bulk solvent environment consisting of DMF. The analysis of the geometric structure and energetics of these complexes were conducted by considering parameters such as the Sn←solvent bond length (d), the complexation energy ($E_{complex}$), and the SnI_2-solvent pairwise interaction energy (E_{int}) between SnI_2 and the solvent. These parameters are illustrated in Figure 6.3a and summarized in Table A4.1. The calculated $E_{complex}$ values indicate that the complexation of SnI_2 with tBP is more thermodynamically favorable in comparison to the corresponding complexes formed with DMI, DMF, and DMSO. The SnI_2:2tBP complex is notably distinguished as the most exoenergetic, with the arrangement of two tBP molecules occupying equatorial positions. Notably, including an additional tBP molecule in this complex enhances the strength of both SnI_2-tBP interactions, as evidenced by the increased E_{int}. On the other hand, the favored isomers of SnI_2:2DMI, SnI_2:2DMF, and SnI_2:2DMSO exhibit the axial positioning of their solvent molecules, resulting in a notable elongation of the Sn←O bond length and subsequent attenuation of the SnI_2-solvent interactions. The results mentioned above provide insights into the comparative stability and strength of interactions exhibited by SnI_2 complexes in various solvents. Notably, tBP demonstrates the highest energy favorability and advantageous characteristics as a ligand for SnI_2 complexation.

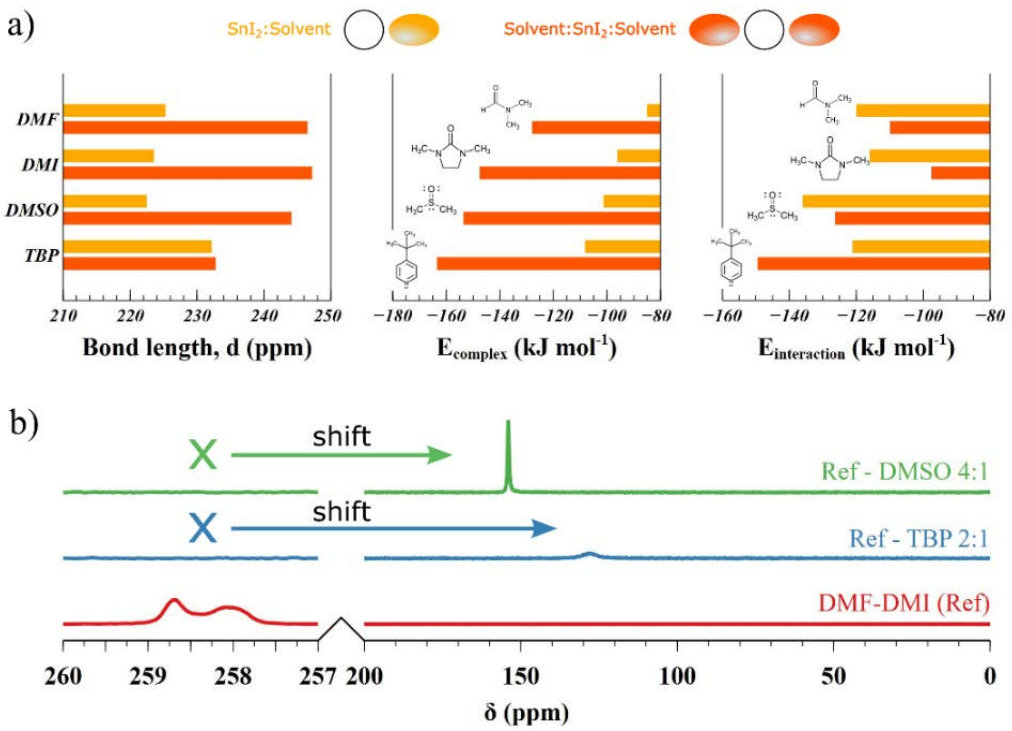

Figure 6.1. (a) geometrical (d, in ppm) and energetic ($E_{complex}$, E_{int}, in kJ mol^{-1}) parameters calculated for the 1:1 and 1:2 complexes in their preferred isomers in DMF solution. (b) ^{119}Sn- NMR signals measured for THP precursors in a DMF-DMI 6:1 solution and with the addition of tBP and DMSO as co-solvents, respectively, at 2:1 and 4:1 volume ratio. All solutions were measured at 0.9M concentration.

In order to provide additional evidence for this theoretical finding, we conducted liquid ^{119}Sn-NMR analysis to assess the solvation state of tin in various solvent mixtures. Figure 6.3b illustrates the presence of two partially overlapping peaks at 258.0 and 258.7 ppm in a 6:1 DMF-DMI solution of the perovskite precursors. The presence of both DMSO and tBP leads to the disappearance of these peaks and their replacement by a single peak at shorter chemical shifts. This observation confirms that the complexing ability of DMSO and tBP is significantly stronger and more stable compared to that of DMF and DMI. The proximity of the chemical shift positions of DMSO and tBP indicates they possess comparable electron density donation capabilities to Sn^{2+}.

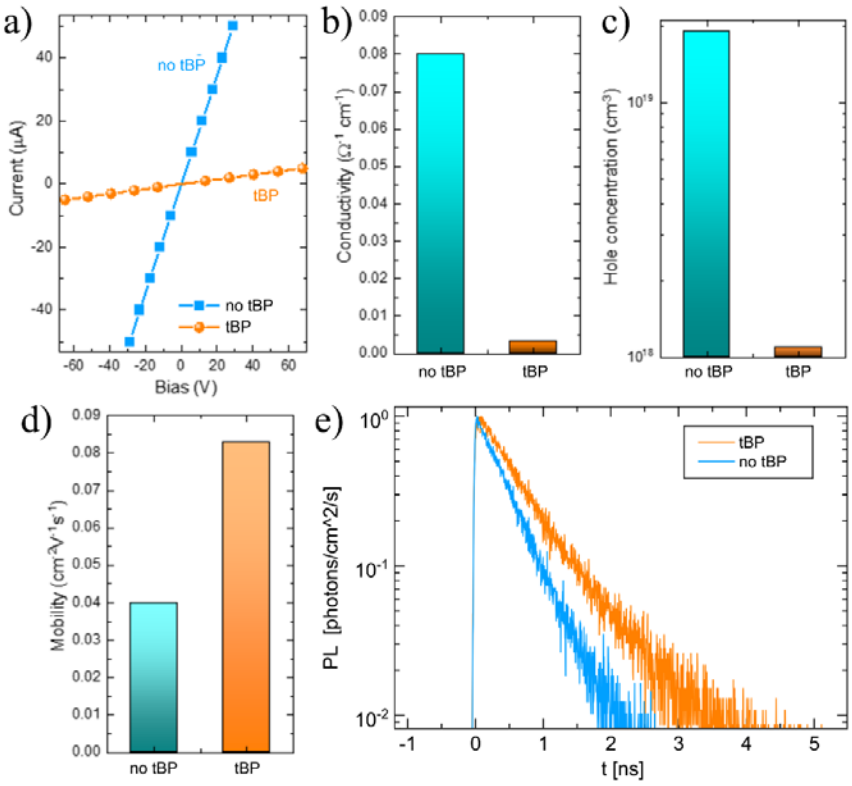

Figure 6.2. (a) current-bias measurements of tBP-treated and tBP-free THP thin films; (b) 4-probe conductivity; (c) Hall concentration; (d) Hall mobility; (e) Electron radiative lifetime calculated from Hall concentration.

6.4 Effect of tBP on the photovoltaic performance of $FASnI_3$:

To assess the influence of tBP incorporation on the transportation of charges in THPs, we conducted a comprehensive analysis of $FASnI_3$ thin films using 4-probe conductivity measurements and the Hall effect technique with alternating current (AC) magnetic field. The results indicate that the tBP sample displayed a significantly lower conductivity of $3.3*10^{-3}$ Ω^{-1} cm^{-1} compared to tBP-free films, which exhibited a higher conductivity value of $8*10^{-2}$ Ω^{-1} cm^{-1} (Figure 6.4a,b). The observed decline in conductivity within the tBP sample can be ascribed to enhanced crystallinity and a reduced presence of defects. Nevertheless, it is essential to acknowledge that a decrease in hole mobility can also impact the reduction in conductivity. Hall effect measurements were conducted to determine carrier concentrations and mobilities directly. The Hall effect measurements revealed that the samples containing tBP exhibited free hole mobility (0.083 $cm^2V^{-1}s^{-1}$), that was twice as high as the reference sample (0.04 $cm^2V^{-1}s^{-1}$) (Figure 6.4d). Furthermore, the tBP samples demonstrated a significantly reduced free hole density, measuring at $1.1*10^{18}$ cm^{-3}, which is ten times lower than the hole density of the reference sample, which measured at $1.9*10^{19}$ cm^{-3} (Figure 6.4c).

The findings of this study demonstrate the essential impact of tBP inclusion on charge dynamics, crystallinity, and defect formation. Specifically, the decrease in the concentration of acceptor defects results in a notable elongation of the radiative lifetime of electrons in the tBP sample, as determined by the calculation of hole concentration (Figure 6.4c). The radiative lifetime increases from 0.1 ns to 2.3 ns. It is worth mentioning that the findings regarding concentration, mobility, and lifetime are consistent with prior research, taking into account the diverse range of values reported by other research teams (Figure 6.4c)[257]. In addition, the measurements of the transient photoluminescence decay of the THP film, both with and without the presence of tBP, supported the observed increase in charge carrier lifetime from 0.4 ns in the absence of tBP to 0.6 ns when tBP was present (Figure 6.4e). The aforementioned results underscore the notable enhancements in the dynamics of charge carriers and optoelectronic characteristics that have been accomplished by incorporating tBP. Consequently, tBP emerges as a highly promising contender for augmenting the efficiency of solar cells based on THP.

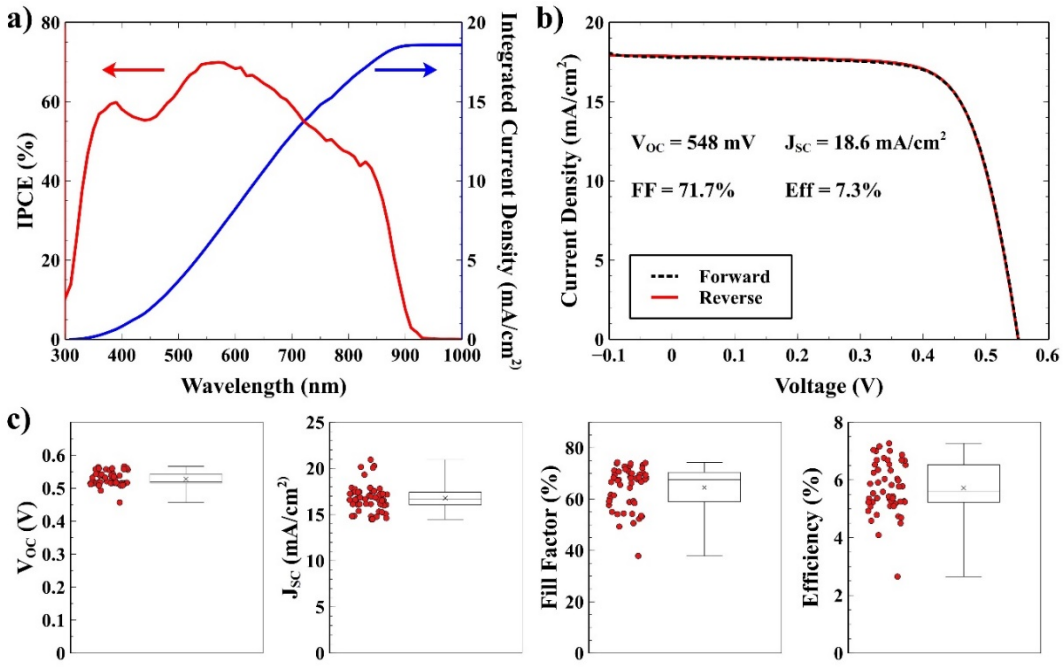

Figure 6.3. (a) EQE spectra. (b) JV curve of the best-performing device. (c) JV characteristics of devices obtained by adding tBP to the precursor solution.

To evaluate the photovoltaic characteristics of films treated with tBP, we prepared p-i-n devices using the ITO/PEDOT/THP/C_{60}/BCP/Ag structure. tBP-free devices demonstrated efficiencies below 2% as a result of the existence of pinholes and inadequate film microstructure. In addition, the reproducibility of these devices is very low due to uncontrolled P-doping, which stems from the oxidation of Sn^{2+} to Sn^{4+}.

Nevertheless, incorporating tBP as a co-solvent yielded a notable enhancement in the crystallization procedure, expanding the THPs processing window and enhancing reproducibility. Figures 6.5a and b present the external quantum efficiency (EQE) and current density-voltage (J-V) characteristics of the most optimal device. The device exhibited an open-circuit voltage (V_{OC}) of 548 millivolts, a short-circuit current (J_{SC}) of 18.6 mA/cm^2 (a value verified by the integrated current density derived from the external quantum efficiency), a fill factor (FF) of 71.7%, and a power conversion efficiency (PCE) of 7.3%. The statistical distribution of V_{OC} and FF displayed notable characteristics, as a significant proportion of devices exhibited V_{OC} values exceeding 500 mV and FF values surpassing 60%. The J_{SC} and PCE values exhibited a slightly greater range of values, yet they still exhibited encouraging performance. The findings of this study demonstrate the notable enhancement in the efficiency and performance of the device by utilizing tBP as a co-solvent in the THP film preparation procedure. The augmented attributes, encompassing elevated values of V_{OC}, J_{SC}, FF, and PCE, serve as evidence of the potential utility of tBP-assisted THP films in the realm of practical and efficient photovoltaic applications.

7. Understanding the limitations of emerging charge transport layers in tin perovskite solar cells

7.1 Introduction:

The exceptional performance of perovskite materials in diverse photovoltaic applications can be attributed to their favorable charge transport characteristics and adjustable bandgap. PSCs have achieved a notable efficiency of 26%, indicating their advanced stage of development and potential for commercialization[258]. However, the realization of these aspirations is impeded by various challenges that have the potential to impede or, in the most unfavorable circumstances, prevent the commercialization of PSCs. Two potential risks that could pose an environmental danger in the event of cell rupture or cleavage are the toxicity of lead and how easy it is to leak into the environment, known as bioavailability[19,20]. In the given context, tin appears to be the most appropriate alternative to lead owing to its structural resemblance[21]. Nevertheless, the efficiency of THPs, which exhibit the highest performance, is around 14% which is 10% lower compared to their lead counterparts. Furthermore, these THPs also lag significantly behind in stability and reproducibility. Energy band misalignment has been identified as a prominent factor contributing to this regression[22].

Tin-based perovskites are known for possessing a VBM and CBM that are comparatively shallower than those of lead perovskites. This leads to a mismatch of the energy bands between CTLs and the tin absorber material, culminating in an energetic mismatch that amplifies interfacial recombination rates and diminishes charge extraction efficiency[172,259]. As a result, tin perovskites' photovoltaic performance is much less than their theoretical potential[260]. In the beginning, the tin perovskite community adopted the n-i-p structure using metal oxides like TiO_2 and Nb_2O_5 as ETLs and Spiro-OMeTAD as HTL. However, this approach presented challenges due to the technical difficulties arising from the chemical reactivity of metal oxides[261]. Introducing fullerenes in PSCs instigated a shift towards the inverted p-i-n architecture for tin perovskites[262]. Here, PEDOT:PSS was implemented as the HTL due to its ease of processing and good wettability, while C_{60}/BCP replaced the reactive metal oxides. Despite the significant energy mismatch at both interfaces, this inverted p-i-n architecture became widespread. It developed to the point where it achieved a PCE of around 15%[212,242]. To unlock the full photovoltaic potential of tin perovskites, effectively managing the energetic alignment at the interfaces is vital. The performance of tin perovskites can be considerably improved by ameliorating the interfacial losses resulting from energy band misalignment.

Several techniques have been developed to enhance the alignment of CTLs with the tin perovskite absorber. These methodologies entail the integration of interfacial molecular additives that generate intermediate energy band positions, leading to improved alignment and more efficient charge extraction[263]. Wang et al., successfully attained a noteworthy open-circuit voltage (V_{oc}) of 0.85 V through the implementation of an intermediate layer composed of ethylene ammonium bromide (EABr). Similarily, Liyuan et al. implemented a perovskite-graded structure, where a narrow bandgap perovskite was utilized in the bulk region, while a wide bandgap perovskite was employed at the interface. This strategic approach resulted in enhanced rates of charge extraction and ultimately yielded a PCE of 11%[264]. In a similar vein, an alternative approach entails the application of a thin film composed of molecules that fulfill a dual role of passivation and regulation of energy alignment. The molecules that exhibited the highest efficacy were Fullerene-n-butyl-pyridine (C_{60}-BPy), 6-maleimidohexanehydrazide trifluoroacetate, and trifluoroacetamide (TFA), resulting in PCEs of 14.1%[265], 13.6%[266], and 11.7%[267], correspondingly. In addition, Hayase and colleagues employed a sequential deposition technique to introduce acetylacetone (AcAc) and Ethylenediamine (EDA) in order to create a series of energy levels that are closely aligned, leading to an improved PCE of 13%[268]. Nevertheless, the optimal resolution for minimizing interfacial energy losses in tin perovskites involves the exploration of novel CTLs that exhibit precise alignment with the conduction and valence band edges of the absorber material. Consequently, numerous theoretical investigations have endeavored to replicate the efficiency of different amalgamations of tin perovskites and CTLs. Among these simulations, the most encouraging one proposes a prospective PCE of 23% by employing FTO/ZnO/$MASnI_3$/CuSCN/CUI/Au as a device stack[269,270].

In order to translate theoretical predictions into practical devices, it is crucial to have an accurate understanding of the energetic landscape of tin perovskites. Detailed investigations are necessary to bridge the knowledge gap concerning the primary limitations of the most used CTLs in tin perovskites. Despite the significance of this topic, to the best of our knowledge, no research has been conducted to address this knowledge gap[271,272]. Nevertheless, accurate measurement of the energy bands positions and charge extraction rates at interfaces is a difficult task, especially when the perovskite film is situated between CTLs and the energy bands are connected in series. Additionally, vacuum or energy beams may damage to the sensitive tin perovskite films[273,274].

In this chapter, the technique of time-resolved surface photovoltage (tr-SPV) was employed to investigate the process of charge extraction in THPs. By utilizing tr-SPV, we could monitor the surface potential induced by illumination and the movement direction of photo-excited charges, thus enabling us to understand the entire charge extraction process from excitation to extraction at the interface. This technique has proved a remarkable efficacy for organic[275] and perovskite solar cells[276] and can investigate deep interfaces in nip and pin architectures[277]. Additionally, we employed an ambient-pressure Kelvin probe (KP) and photoelectron yield spectroscopy (PYS) to build a band diagram for the tin perovskite

device stack. Furthermore, we used various methods, including hall effect, photoluminescence (PL), and KP to determine the hole concentration in the tin perovskite films. Through comparing the efficacy of different CTLs, such as surface monolayers (SAMs), in terms of charge carrier extraction rates at interfaces using tr-SPV, we aimed to shed light on the limitations of each CTL. Finally, we determined the optimal device architecture for charge carrier extraction in THPSCs using tr-SPV.

7.2 P-doping concentration in $FASnI_3$:

Accurately estimating the p-doping level of tin perovskites is crucial for comprehending their charge dynamics and band alignment. Nonetheless, the exact hole concentration in $FASnI_3$ remains imprecise, with reported values ranging from 10^{15} to 10^{18} cm^{-3} using 10% SnF_2[278]. Therefore, in this chapter, we did the measurements using different methods at the same where prepared together at the same batch. We employed Hall effect, PL, and KP-PYS. Our results show that the Hall effect and PL techniques exhibit the same concentration of $1.5x10^{17}$ cm^{-3}, which is in agrees strongly with the KP-PYS measurements revealing hole concentrations of $1.9x10^{17}$ cm^{-3} and $1.3x10^{17}$ cm^{-3} on freshly prepared $FASnI_3$ films on quartz glass and ITO substrates, respectively. These values were calculated based on the EF-EVBM energies of 0.01 eV and 0.08 eV from KP-PYS measurements and hole effective mass in $FASnI_3$ of 0.05 m_o. The agreement of the hole concentration from the three different techniques indicates that the 0.05 m_o hole effective mass reported by Xie et al. is the most accurate value when compared to the other values[279].

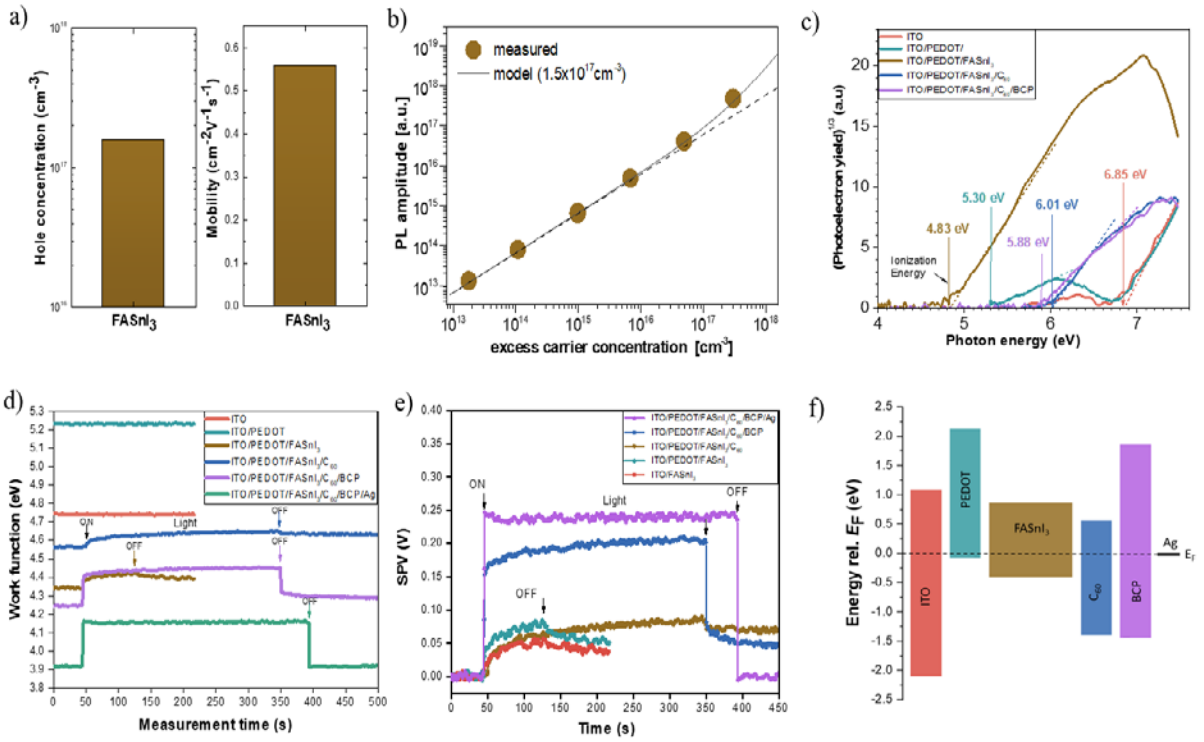

Figure 7.1. (a) The conductivity and mobility measurements of $FASnI_3$. (b) TRPL measurements for the doping concentration in $FASnI_3$. (c) PYS measurements of the device stack revealing the ionization potential for each layer. (d) Time-resolved WF measurements in the dark and under illumination (on and off refers to lighting). (e) KP-generated SPV signals for a full tin perovskite device stack. (f) The band diagram aligned to the Fermi level (E_F) was plotted from the values obtained by the KP-PYS technique.

7.3 Energy bands of $FASnI_3$:

In order to gain a comprehensive understanding of the constraints associated with CTLs in THPs, a thorough examination is conducted to assess the alignment of interfacial energy bands between the absorber layer and different CTLs, as well as the kinetics of charge carrier extraction. Significant variations in the positions of conduction and valence bands among different tin perovskite compositions and CTLs have been observed in the literature. These variations can be attributed to several challenges encountered during the measurement process, including the sensitivity of Sn^{2+} to oxygen, beam damage during high-energy photoelectron analysis, and composition changes under high vacuum conditions. In order to tackle these concerns, KP-PYS measurements are performed in a controlled environment of an inert N_2 atmosphere, maintaining ambient pressure and temperature conditions. This experimental approach involves the utilization of low-energy photons with energy levels ranging from 3.4 to 7.5 eV. A band diagram for the ITO/PEDOT/FASnI3/C_{60}/BCP/Ag solar cell device is constructed based on the provided measurements. The position of the Fermi level is determined through work function

measurements conducted by KP[280]. Meanwhile, the band bendings and the individual contributions of each layer to the solar cell's V_{oc} are derived from the magnitude of the SPV signal obtained from KP data, both in the absence of light and under illumination. The determination of the VBM position is based on the ionization energy derived from PYS spectra[172]. This is achieved by employing linear regression and extrapolation techniques on the $Y^{1/3}(h\nu)$ data, with the exception of Ag. The $Y^{1/3}(h\nu)$ values are plotted separately, using a square root transformation. The position of the conduction band minimum (CBM) is determined through the addition of the band gap of the thin film to the energy of the valence band maximum (EVBM), assuming the presence of flat band conditions under the illumination of 100 mW/cm^2. Subsequently, the doping concentration of the films is determined. It is imperative to acknowledge that the measurements of ionization energy (E_i) and WF were performed using the identical Kelvin probe tip at the identical sample position[243]. Furthermore, the integrity of the Kelvin probe tip was duly verified prior to each measurement. Furthermore, the consistent ionization energy values obtained from multiple PYS measurements suggest that the thin film surface being investigated exhibits chemical stability[257].

The work function measurements obtained in the dark and under lighting of the THP devices are depicted in Figure 7.1d. The measurements exhibited consistent values over a period of time, indicating the chemical stability and uniformity of the surface of the films that were prepared. Following the application of illumination, there was an observed augmentation (reduction) in the values of the WF and E_F, correspondingly[281]. The manifestation of this dynamic transformation caused by illumination became apparent subsequent to the application of the $FASnI_3$ thin film and remained present in conjunction with C_{60}. However, there was a notable increase observed following the evaporation of BCP and Ag, which aligns with the evolved SPV signals of the device stack that was deposited and measured layer by layer, as depicted in Figure 7.1e. The changes observed in the WF and surface photovoltage (SPV) signals when exposed to light suggest the occurrence of charge separation and extraction processes, which are closely related to the V_{oc} of the device. A notable augmentation in the extracted charges was observed subsequent to the deposition of BCP, underscoring its pivotal function in electron extraction. The forthcoming section of this chapter will present the energetic explanation of this role[280].

7.4 The role of BCP:

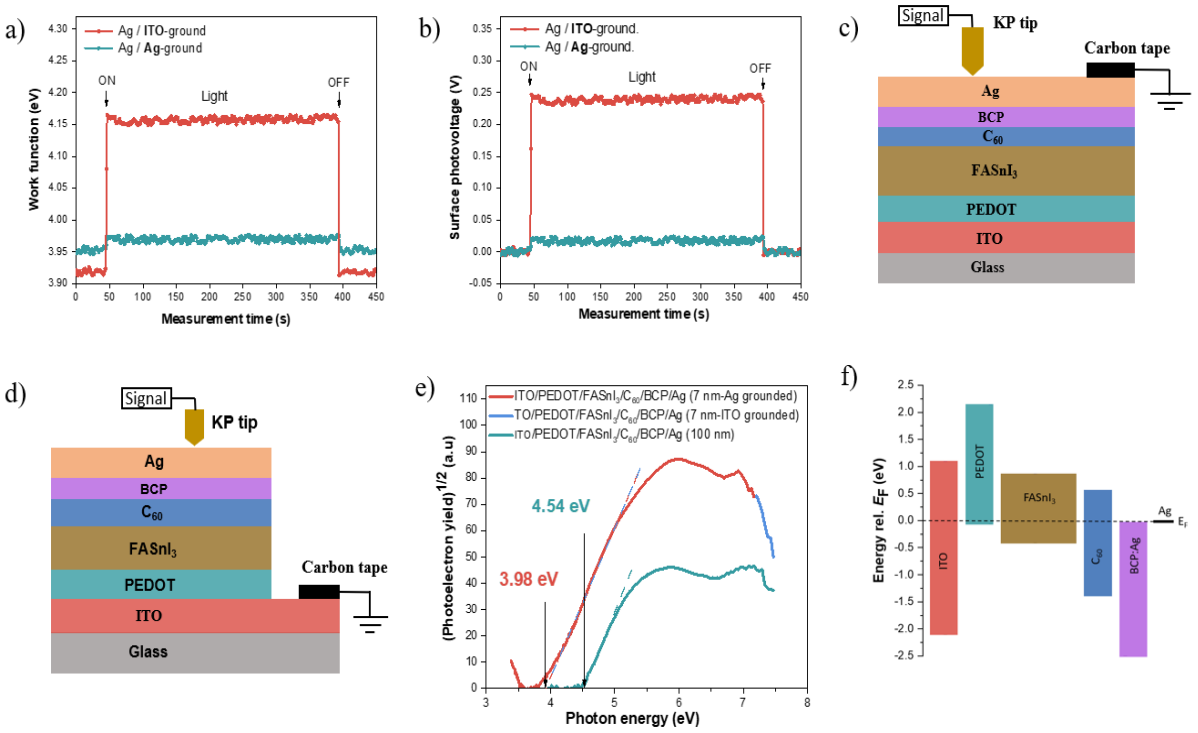

Figure 7.2. (a) grounded Ag and ITO KP W_F measurements. (b) SPV signals of the device stack generated through KP measurements. (c) Schematic diagram of the KP-PYS Ag-grounded measurement. (d) ITO-grounded measurement. (e) E_i measurements of Ag and ITO grounded samples with 7 nm thickness and 100 nm thick Ag film. (f) Modified energy band diagram of a full device stack with BCP:Ag blend.

The insertion of the BCP on the top of the ETL (mostly in conjunction with C_{60}) has been recognized as a means to create a cascade of energy levels. This insertion also serves to establish a hole blocking layer, which effectively hinders holes and inhibits charge recombination at the interface. Additionally, it improves electron transfer and extraction[282]. Nevertheless, the significant improvement in electron extraction prompted us to examine the interface between BCP and Ag in order to gain a deeper understanding of the underlying reasons for this enhancement from an energetic perspective. Consequently, we have assembled a complete device stack featuring a thin Ag film of 7 nm in thickness. The KP measurements were conducted under two conditions: in the absence of light and under illumination. The ITO film was grounded in the first measurement, while the Ag film was grounded in the second measurement. These experimental setups are depicted in Figures 7.2a-d. The KP-PYS measurements were conducted on the identical sample position in both instances. It is essential to observe that in the grounded indium tin oxide (ITO) scenario, the signals are measured in relation to the ITO thin film's electrical field (E_F). Conversely, in the case of grounded silver (Ag), the signals are measured in relation to the E_F of the Ag layer.

The dark Kelvin probe measurements (Figure 7.2a) indicate that the WF values for Ag and ITO grounding exhibit a high degree of similarity, falling within the range of 3.92 eV to 3.95 eV. In addition, the PYS measurements depicted in Figure 7.2e demonstrates that the Ei value remains constant at 3.98 eV for both scenarios. Hence, regardless of whether the thin film on a stack of solar cells is measured by grounding the solar cell's ITO contact or directly on the Ag top layer, the utilization of KP provides an accurate determination of the WF of the film. The observed SPV in the Ag-grounded measurement, as depicted in Figure 7.2b, is ascribed to a minor surface band bending occurring in the uppermost layer. The observed SPV in the plot grounded with ITO is believed to be linked to the V_{oc} of the stack. This Voc arises from the splitting of the Fermi level due to the generation of charge carriers when the $FASnI_3$ absorber thin film is illuminated.

In conclusion, it can be observed that both the KP (dark) and PYS measurements yield similar values for WF and E_i, respectively. This outcome aligns with the anticipated results for measurements conducted on either a metallic material or a degenerate semiconductor. Nevertheless, the measured value of approximately 4.0 eV is observed to be 0.56 eV lower than that of the Ag reference film with a thickness of 100 nm (Figure 7.2e). Additionally, it demonstrates a decrease of 0.25 eV in comparison to the WF of BCP, and a significant reduction of 1.88 eV when compared to the E_i of BCP[283]. The results indicate that the Ag deposited in the initial stages undergoes diffusion into the BCP layer, resulting in the formation of a BCP:Ag blend with a WF of approximately 4 eV[284,285]. This value is widely recognized as optimal for promoting effective electron extraction from C_{60}.

Recently, the notion of an Ag:BCP blend layer was introduced in literature in both tandem[286] and single junction devices[287]. This layer serves as an intermediary between C_{60} and indium-zinc oxide (IZO), which functions as a transparent electrode. The objective was to safeguard the C_{60} layer against sputtering-induced damage while depositing the upper conductive electrode. The researchers demonstrated the formation of a charge transfer complex between Ag and bis(4-carboxyphenyl)amine (BCP) through the establishment of coordinate covalent bonds between Ag and the nitrogen (N) atoms of BCP during the process of evaporation. Previous studies have also documented comparable interactions between BCP and electrodes composed of a distinct metal, such as Mg[288]. Ying et al. proposed that the Ag:BCP complex gives rise to gap states that serve as conduits for facilitating the transport of electrons to the electrode. Nevertheless, our examination of the interface between BCP and Ag demonstrates comparable energies of approximately 4.0 eV for both the work function and ionization energy. These findings suggest the presence of a deteriorated surface layer consisting of Ag:BCP. Hence, we posit that the Ag:BCP exhibits a complex nature, wherein its Fermi level aligns with its CBM position at 4.0 eV. The contact layer with a low work function facilitates a downward bending of the C_{60} bands, thereby facilitating the efficient transfer of electrons from C_{60} to the Ag electrode at the device's back side. This phenomenon is illustrated in Figure A5.6. In conclusion, we propose a revised energy band diagram, as

depicted in Figure 7.2f, wherein the conventional BCP layer is substituted with an Ag:BCP blend possessing a WF of approximately 4 eV.

Charge extraction dynamics at charge selective contacts:

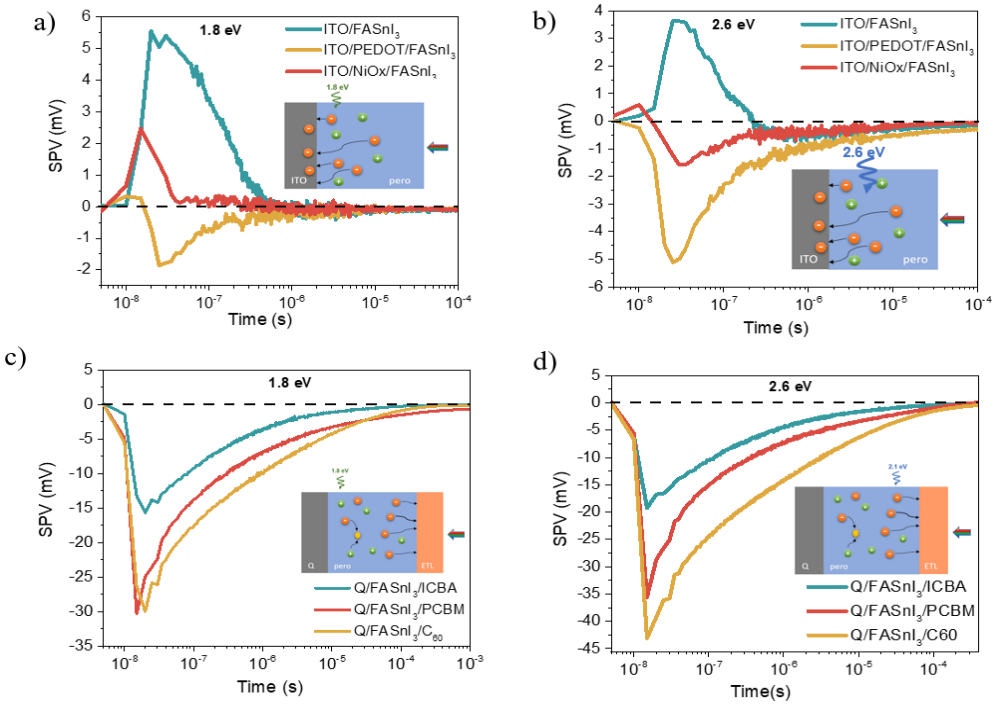

Figure 7.3. **(**a & c) excitation using 688 nm laser pulse (1.8 eV), exciting charge carriers close to the deep interface. (b & d) excitation using a 486 nm laser pulse (2.6 eV) exciting charge carriers in the bulk of the perovskite film.

After providing a visual representation of the energetic topography in the prevalent THP stack, we proceed to examine the efficacy of various CTLs in extracting charges from the absorber layer through the measurement of tr-SPV. The interfaces under investigation were illuminated from the upper side, as depicted in the insets of Figure 7.3, using photon energy above the bandgap. Subsequently, we measured the charge dynamics within a time range of 5 nanoseconds to 1 milliseconds. The tr-SPV diagram of neat $FASnI_3$ is depicted in Figures 7.3a and 3b insets, showcasing two distinct excitation energies of 1.8 eV and 2.6 eV. These energies correspond to penetration depths of 210 nm and 90 nm, respectively, as indicated in Figure A3.7. The SPV signal indicates the spatial separation of electrons or holes. The transient exhibits a positive (negative) indication of the separation of electrons (holes) within the bulk of the thin film towards its surface or interface. Consequently, the perovskite film acquires a positive (negative) charge[276]. The amplitude and rise rate of the signal serve as indicators of the quantity of separated charges, thereby reflecting the efficacy of charge extraction. The subsequent decrease in signal observed can be attributed to the recombination losses experienced by the separated charge carriers Figure A3.8.

The initial step involves quantifying the capacity of ITO to directly extract charges from the $FASnI_3$ layer, without the presence of any CTL intermediaries. The interface between ITO and $FASnI_3$ was observed to exhibit a positive tr-SPV signal. This signal suggests the presence of electron accumulation in close proximity to or within the ITO material, as depicted in Figures 7.3a and b. The amplitude of the signal peak exhibited a decrease as the distance between the interface and the generated carriers increased, specifically in the case of 2.6 eV photons (Figure 7.3b). The observed accumulation of electrons can be ascribed to the phenomenon of electron trapping or transfer within the ITO. This effect has been previously documented in the interface between ITO and lead perovskite, as reported in a recent publication[276]. In addition, we investigate the dynamics of hole extraction at the interfaces of $FASnI_3$ and HTLs. In contrast to the ITO/$FASnI_3$ interface, the PEDOT/$FASnI_3$ interface exhibits negative signals throughout the perovskite film, indicating the extraction of holes in the PEDOT layer. Nevertheless, the strength of the signal is more pronounced when carriers are generated at greater depths within the perovskite film, as depicted in Figure 7.3b, in comparison to the proximity of the interface, as illustrated in Figure 7.3a. The observed variation in amplitude indicates a significant interfacial recombination rate or barrier at the interface between PEDOT and $FASnI_3$. This highlights the importance of interfacial passivation and alignment of the buried interface in THPs[289] (-). It is worth mentioning that PEDOT exhibits a minor initial positive response, characterized by early electron entrapment at the interface prior to 10 ns, which is subsequently overwhelmed by hole extraction (Figure 7.3a)[290]. This suggests that the charge extraction mechanism at the interface of PEDOT/$FASnI_3$ is influenced by the interplay between two competing processes: hole extraction and electron trapping. This behavior can be attributed to the misalignment of energy bands and the limited charge selectivity of PEDOT. However, the hypothesis regarding electron trapping aligns well with the experimental data obtained at 2.6 eV for the PEDOT interface (Figure 7.3b). No positive signal was detected in this case due to electron-hole generation and recombination occurring far from the PEDOT interface. Instead, the dominant phenomenon observed was the drift of the majority of free holes within the bulk of the p-type material[195].

In this chapter, we investigate the hole extraction properties of NiOx, as well as two self-assembled monolayers (2PACz and MeO-2PACz) based on carbazole. These monolayers have demonstrated promising hole extraction capabilities in lead-based perovskite cells[276] and have also been explored for tin perovskites[291]. The transient response of NiOx exhibits a significantly attenuated negative signal and inferior hole extraction capabilities compared to PEDOT. The generation of free carriers in close proximity to the interface, specifically with a 1.8 eV photon, results in the predominant accumulation of electrons at the NiOx/$FASnI_3$ interface. This electron accumulation is responsible for the observed positive tr-SPV signal, as depicted in Figure 7.3a. Simultaneously, the extraction of holes is observed exclusively under 2.6 eV illumination, a condition that is still notably influenced by the positive signal indicating the accumulation of electrons. The comprehensive qualitative analysis of charge transport at the NiOx interface is presented in Figure A3.9. In contrast, it was observed that only 2PACz exhibited

indications of hole extraction under 2.6 eV illumination within the group of SAMs, as depicted in Figures A3.10a and b. Similarly, SAMs exhibited electron accumulation and relatively limited extraction capabilities when compared to poly(3,4-ethylenedioxythiophene) (PEDOT). In order to assess the impact of the alignment effect on hole extraction by SAMs, we introduced a 20% concentration of $SnBr_2$ to enhance the valence band of tin perovskite[172]. Notably, the enhancement of hole extraction can be observed by utilizing NiOx, 2PACz, and MeO-2PACz. This observation provides evidence that these HTLs have the potential to be effective in conjunction with tin perovskites, given that the energy bands are suitably aligned. In summary, it can be inferred that optimizing these hybrid tin-perovskites with a broader bandgap holds potential for their utilization in lead-free tandem applications.

7.5 Electron extraction dynamics at THPSCs:

In order to investigate the electron extraction dynamics occurring at the interfaces of perovskite/ETLs, we conducted tr-SPV measurements for ICBA, PCBM, and C_{60} materials that were deposited onto FASnI3. These measurements are illustrated in Figures 7.3c and d. In this particular configuration, the illumination is directed from the upper side. Therefore, it can be observed from the inset of Figure 7.3c and d that the charge carriers near the interface are generated by the higher excitation energy of 2.6 eV. In contrast, the lower energy laser of 1.8 eV predominantly excites charge carriers in the bulk of the film. Negative signals are observed for all ETLs, suggesting the presence of active electron extraction at the interface. The observed significant amplification of the signal amplitude indicates the presence of rapid electron separation dynamics towards the ETL. In general, C_{60} exhibits enhanced extraction capabilities, particularly when subjected to excitation close to the interface. It is noteworthy that the rate at which charges are extracted in the three ETLs aligns with the order of charges mobility, specifically 1.6 cm^2 V s^{-1}, 6.1 × 10^{-2} cm^2 V s^{-1}, and 16.9 × 10^{-3} cm^2 V s^{-1} for C_{60}, PCBM, and ICBA respectively, rather than the order of the CBO values. The correlation above elucidates the exceptional efficiency of C_{60}-based devices, despite the disparity in energy bands when compared to ICBA and PCBM. Additionally, it is essential to acknowledge the crucial contribution of BCP when combined with C_{60} to create a unified ETL[292]. Furthermore, the C_{60} interface, along with other ETLs, exhibits a significantly higher peak amplitude of the signal (-47 mV) in comparison to the PEDOT interface (-5 mV). This observation indicates superior electron extraction capabilities as opposed to hole extraction capabilities. The discovery is intriguing as it reveals a significant impact of vacant traps on the behavior of electrons, which serve as minority carriers, within p-type doped $FASnI_3$. Consequently, it is anticipated that the amplitude of tr-SPV signals would be lower for interfaces involving ETLs compared to interfaces involving HTLs. This observation serves to emphasize a limitation in the current THPSC-HTL interface.

To investigate the extraction of electrons and holes concurrently, we performed a tr-SPV comparative analysis of a sample containing both ETL and HTL, as illustrated in Figure A3.10. The findings indicate

a substantial improvement in the extracted charges, as evidenced by the tr-SPV signal's amplitude (-80 mV), which is several magnitudes greater than the combined signals of the pure ETL and HTL. The observed significant augmentation in the amplitude of the tr-SPV peak indicates a robust association between the extraction of electrons and holes, thereby emphasizing the considerable losses in recombination resulting from the presence of unextracted carriers. The phenomenon of carrier recombination encompasses multiple pathways, such as nonradiative, surface, and radiative channels. For a more comprehensive analysis, readers are referred to Appendix note A3.1 and Figure A3.11.

7.6 Simulation of interfacial charge extraction and recombination:

In the preceding section of this Chapter, we presented a qualitative analysis of the charge transport dynamics occurring at tin perovskite interfaces. This analysis involved the utilization of different ETLs and HTLs. This section presents a quantitative analysis of charge extraction efficiency and the underlying mechanisms accountable for charge loss through the utilization of charge extraction and recombination simulations. In this study, we conduct simulations to analyze the charge transport in interfaces demonstrating the most efficient charge extraction in tin perovskites. We then proceed to compare the efficacy of charge extraction in these interfaces with similar interfaces found in lead-based perovskite, specifically $(Cs_{0.05}FA_{0.85}MA_{0.095})Pb(I_{0.9}Br_{0.1})_3$. This comparative analysis will facilitate the acquisition of insights pertaining to the fundamental mechanisms responsible for charge losses, thereby furnishing valuable information for formulating future strategies to augment the performance of THPs and other optoelectronic devices.

There exist three mechanisms through which charge loss can occur: radiative recombination, nonradiative bulk recombination, and nonradiative recombination at the interfaces. Radiative recombination, denoted as $Cb\cdot\Delta n(t)\cdot(\Delta p(t)+p0)$, is influenced by the background hole concentration p0. Nonradiative bulk recombination, represented as $\Delta n/\tau\_(non\text{-}rad)$, takes place through bulk defects. Nonradiative recombination at the interfaces is characterized by ($s_{etl}\cdot\Delta n$ and $s_{htl}\cdot\Delta p$), where $\Delta n(t)$ and $\Delta p(t)$ denote the photogenerated electrons and holes, respectively. The three recombination channels discussed in this study are regarded as crucial determinants of charge dynamics in perovskite interfaces. Additionally, the electron and hole extraction rates, denoted as $Ke\cdot n(t)$ and $Kh\cdot p(t)$ respectively, are also considered significant factors. The coefficients for electron and hole extraction rates are represented by Ke and Kh, as illustrated in Equations 1-2 and Figure 7.4a.

$$\frac{d\Delta p}{dt} = -K_h\Delta p + K_{hb}\Delta p_{HTM} - C_b\big((\Delta p + p0)\Delta n\big) - \frac{\Delta p}{\tau_{non-rad}} - s_h\Delta p \qquad \textbf{(1)}$$

$$\frac{d\Delta n}{dt} = -K_e \Delta n + K_{eb} \Delta n_{HTM} - C_b\big((\Delta p + p0)\Delta n\big) - \frac{\Delta n}{\tau_{non-rad}} - s_e \Delta n \qquad \textbf{(2)}$$

The Levenberg-Marquardt method[276] was utilized as the initial approach to fit the experimental data of $FASnI_3/C_{60}$ and $FASnI_3$/PEDOT[293]. The objective was to ascertain the rate constants most accurately correspond to the experimental tr-SPV outcomes. The fit results are displayed in Figure 7.4b and Table A5.1, whereas the temporal progression of electrons, holes, and extracted electrons is illustrated in Figure 7.4e. We then conducted a comparable fitting procedure to analyze lead perovskites' electron and hole extraction dynamics. The tr-SPV measurements were employed in our study, following the same experimental conditions. This can be observed in Figures 7.4c, f, and Table A5.1. A thorough analysis of the charge extraction dynamics demonstrates a clear association between the temporal increase of the tr-SPV signal as depicted in Figures 7.4b and c and a decrease in the concentration of carriers (as illustrated in Figures 7.4e and f) within the perovskite film. The ETL's electron concentration decline directly results from the charge extraction process. The degradation of tr-SPV and the peak magnitude of the tr-SPV signal is significantly impacted by radiative and nonradiative recombination mechanisms, which have a tendency to reduce the overall carrier concentration.

Based on the simulation outcomes, notable disparities are evident in charge extraction and recombination processes when comparing lead and tin perovskites. The lead perovskite system demonstrates reduced recombination losses, leading to an increased carrier lifetime and an elongated exponential tail, as depicted in Figure 7.4f. Furthermore, it is worth noting that the lead perovskite exhibits a greater concentration of extracted charges, specifically electrons and holes (Figure 7.4e-f). The total extracted charge, Qex, determined by calculating the surface area under the nex(t) and pex(t) curves, is also larger. These findings are summarized in Figure 7.4d. Notably, the overall extracted charge in the lead perovskite system exhibits a near balance, as evidenced by the ratio of Qe/Qh being approximately equal to 2. However, a considerably more notable distinction is observed in the tin perovskite system, where the ratio of Qe to Qh is 14.5. Moreover, the tin perovskite system experiences a significant loss of charge. In particular, the ETL demonstrates a significantly reduced electron extraction efficiency, approximately 30 times lower. In contrast, the HTL exhibits a diminished hole extraction efficiency of approximately 160 compared to the lead perovskite system. The observed substantial decrease in extracted charge underscores the limited efficacy of tin perovskite solar cell interfaces in facilitating the extraction of both holes and electrons, along with the presence of significant recombination losses.

Upon showcasing the modest charge extraction capabilities of tin perovskites compared to lead-perovskite interfaces. Subsequently, the influence exerted by each recombination channel on the extracted charges is quantified. Three key factors can potentially affect the extracted charges, namely

the extraction rate constant (also referred to as rate constant deficit), nonradiative recombination, and radiative recombination. In this chapter, we will investigate the impact of each of these factors on the extracted charges and conduct a comparative evaluation of the extraction and losses pertaining to both holes and electrons. It has been observed that the tin-based perovskite material demonstrates lower charge extraction constants, as depicted in Figure 7.4d. The HTL exhibits a rate constraint that is 33 times lower, while the ETL shows a rate constraint that is 12 times lower. The observed disparity could potentially be attributed to the lack of alignment in energy levels between the absorber layer and the CTLs, as indicated by the KP-PYS data depicted in Figure 7.1. Alternatively, this phenomenon may be ascribed to the degradation of the perovskite surface, leading to an inadequately aligned interface with the CTLs. In this study, we establish the charge extracted from lead perovskite, which possesses a power conversion efficiency of 22%, as the reference point. Subsequently, we systematically investigate the effects of various factors on charge extraction, namely extraction constant deficit, nonradiative recombination, and radiative recombination. By analyzing the impact of these factors individually, we aim to evaluate their respective contributions to charge losses. Ultimately, this analysis will provide valuable insights into addressing the challenge of energy bands misalignment in tin perovskites. The charge losses can be observed in Figure 7.4h and i, with the electron and hole charge from Figure 7.4d represented as 100% in each case. The percentage of charge loss can be determined by employing the formula: loss = $(Q_{pero} - Q_{tin}) / Q_{pero}$.

Nonradiative recombination is the predominant mechanism responsible for charge loss in both ETLs and HTLs. Specifically, it accounts for approximately 90% of the charge loss occurring at the ETL interface and about 99% at the HTL interface. The observed increase in loss percentage at the HTL interface can be ascribed to the greater surface recombination, as evidenced by the data presented in Table A5.1. The deficit in the extraction rate constant is responsible for 70% and 60% of the charge loss observed at the ETL and HTL interfaces, respectively. Notably, within the HTL interface, high material doping at a concentration of $1.5*10^{17}$ cm^{-3} leads to a substantial loss of holes, with approximately 97% of holes being lost. On the other hand, it is observed that the doping level in the ETL results in a mere 28% reduction in electron count at the tin ETL interface. In order to ascertain the underlying factors contributing to this behavior, we conducted a graphical representation of quasi-Fermi level splitting (QFLS) in both lead and tin systems. This analysis effectively illustrates the impact of recombination channels on the concentration of charges within the perovskite absorber film. Moreover, we took into account the influence of additional surface recombination in the ETL and HTL, as depicted in Figure 7.4j. The passivation capability of 2PACz in lead perovskites has been found to be greatly improved, resulting in a QFLS value of 1 eV. This value is in close proximity to the Shockley-Queisser limit of 1.1 eV observed in $FASI_3$. On the other hand, it can be observed that the C_{60} interface exhibits a higher vulnerability to nonradiative recombination, leading to a quantum fluorescence yield loss (QFYL) of 0.84 eV. As a result,

the presence of doping and radiative recombination significantly affects the charge extraction potential at the interface between the HTL and tin perovskite film, in contrast to the ETL interface

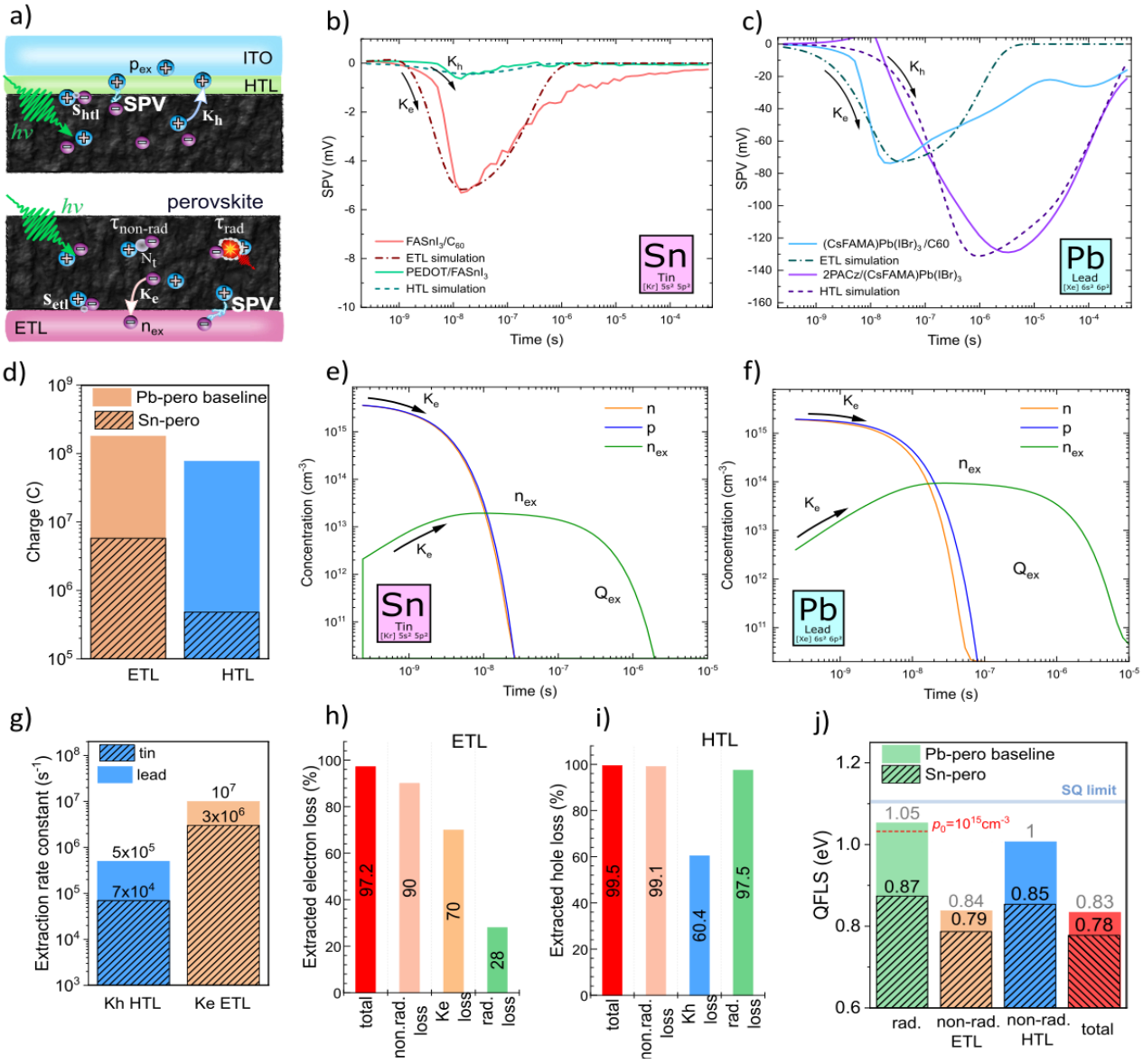

Figure 7.4. (a) Schematic diagram of charge extraction. (b) SPV data fitting for top an bottom interfaces of the device stack understudy. (c) SPV data fitting for lead perovskite comparative system. (d) Total electron and hole charge extracted at interfaces for one laser pulse. (e) and (f) Time resolved the evolution of charge carrier concentrations in the absorber layer and the development of extracted electrons in the tin and lead systems. (g) Hole and electron extraction rate constants. (h) and (i) Loss pathways for extracted charge carriers induced by different decay mechanisms, using Pb system as a baseline. (j) Quasi-Fermi Level Splitting (QFLS) affected by nonradiative and radiative recombination channels.

To attain the fundamental level of performance exhibited by lead perovskite, which is characterized by an efficiency of 22%, it is imperative to undertake a number of crucial measures. First and foremost, it

is imperative to effectively decrease nonradiative recombination and passivate trap states in both the bulk and surface of the tin perovskite absorber material. It is imperative to attain lifetimes in the microsecond range, comparable to the durations observed in perovskites containing lead. Additionally, it is imperative to decrease the density of background holes to a minimum level of $1*10^{15}$ cm^{-3}. In addition, it is imperative to enhance the alignment of the ETL and HTL to optimize the extraction rate constants, with the desired target being approximately $1*10^{7}$ $cm^{-3}s^{-1}$. The aforementioned enhancement can be attained through investigating novel charge transport materials or utilizing self-assembled monolayers featuring shallow energy levels. The study demonstrates a charge extraction methodology and presents findings that can be used to identify ideal ETL and HTL candidates. These candidates have the potential to achieve performance levels comparable to lead perovskite, as established in this research. Furthermore, the implementation of a multimethod approach that integrates AC Hall, Kelvin Probe, and photoluminescence techniques can be employed to accurately optimize the doping levels, thereby enhancing the utilization of environmentally sustainable tin perovskite in a wide range of optoelectronic devices.

8. Conclusion and outlook

Chapter 5:

In this study, we extensively evaluated approximately 80 molecules to identify solvents capable of forming stable $FASnI_3$. Our investigation encompassed various functional groups, including combinations of these groups in bifunctional molecules. As a result, we identified 16 solvents that do not contain sulfoxide groups. Additionally, we determined the Hansen Solubility Parameters for $FASnI_3$ and calculated the binding energy between the solvents and Sn^{2+} using DFT. This information provides insights into the solubility mechanism of $FASnI_3$, driven by the complexation with Sn^{2+}, and serves as a guideline for identifying additional solvents and formulating suitable solvent mixtures. With the exception of trimethyl phosphate and 2-methoxyethylamine, all the specified solvents could form perovskite. The wide range of boiling points and binding energies to Sn^{2+} offers significant opportunities for controlling the nucleation and growth of $FASnI_3$. Regarding thermal stability, NMF and 2-ME were found to undergo degradation at 100°C, as observed through NMR analysis. However, none of the solvents led to the oxidation of Sn^{2+}. Notably, we discovered a novel solvent system composed of a DEF:DMPU mixture, which outperformed films processed from DMSO when fabricated into solar cells. These results demonstrate that it is possible to eliminate the detrimental tin oxidation associated with DMSO while still obtaining high-quality tin halide perovskite films. We anticipate that further screening efforts may lead to the discovery of additional solvent systems with enhanced performance. Overall, the findings presented in this manuscript will contribute to the effective and informed solution processing of $FASnI_3$ for the production of lead-free perovskite solar cells.

Chapter 6:

In brief, establishing a stable complex between tBP and the tin halide is of utmost importance in regulating the dynamics of crystal nucleation and growth, leading to a morphology devoid of pinholes and notably increased crystal grain size. The present study employed a comprehensive approach involving thorough film characterization and numerical simulations to investigate the interactions between tBP and THP. The findings underscored the pivotal role of these interactions in shaping the crystallization process. The inclusion of tBP as a co-solvent resulted in a significant enhancement in the mobility of hole charge carriers. This improvement can be attributed to several factors, including enhancing film morphology, reducing defects density, and mitigating self-doping effects. Consequently, a replicable protocol was established to prepare Pb-free and DMSO-free devices with enhanced efficiency. Among the aforementioned devices, the most optimal one demonstrated a notable efficiency of 7.3%, thereby highlighting the considerable potential of this methodology in developing solar cells that exhibit superior performance characteristics while also being environmentally sustainable.

Chapter 7:

In this work, we investigated the energy bands alignment profile of $FASnI_3$ in the most used device stack ITO/PEDOT/$FASnI_3$/C_{60}/BCP/Ag using PK-PYS setup. We evaluated the energy diagram of the full stack layer by layer to measure the accurate energy position of every as close as possible to actual operating conditions. We also highlighted the energy mismatch at the PEDOT/$FASnI_3$ interface and the $FASnI_3$/C_{60} interface, leading to charge recombination and overall humble device performance.

The role of BCP was also explained, and found that it forms a complex with Ag, establishing an intermediate energy level that facilitates electron extraction. Tr-SPV measurements and KP-based SPV measurements confirmed the same results and illustrated the significant effect of BCP in electron extraction. In addition, the doping concentration of $FASnI_3$ was confirmed using three different techniques and found to be in the range of $1.5 * 10^{17}$ cm^{-3} with only 10% SnF_2 as an additive.

We also studied the charge extraction dynamics using transient SPV for the first time in tin halide perovskites. We proved the validity of such technique for encapsulated tin perovskite samples. We investigated the extraction dynamics of HTL/$FASnI_3$ interfaces using PEDOT and NiOx and found that both show very low hole extraction and low selectivity. However, PEDOT shows relatively better hole extraction than NiOx, which was enhanced by adding $SnBr_2$ to increase the energy band alignment. We also investigated SAMs, and found that it could work as HTL for tin perovskites provided a good energy band alignment. On the other hand, we investigated the electron extraction dynamics and found that C_{60} and BCPM show better electron extraction than ICBA. Surprisingly, the extraction abilities of the three films followed the charges mobility order rather than the CBO order.

We suggest designing a new charge extraction system well aligned with the shallow HOMO and LUMO levels of tin perovskite structures or trying the opposite strategy of controlling the WF of tin perovskites by polar surface additives to enhance the band alignment with good CTLs such as C_{60}/BCP.

9. Bibliography:

1. (20) (PDF) A Critical Discussion of Recent Studies Evaluating the Impacts of Climate Change on Water Resources in the Nile basin. Available at: https://www.researchgate.net/publication/256598224_A_Critical_Discussion_of_Recent_Studies_Evaluating_the_Impacts_of_Climate_Change_on_Water_Resources_in_the_Nile_basin. (Accessed: 6th August 2023)

2. (20) (PDF) The uncertain future of the Nile Delta. Available at: https://www.researchgate.net/publication/301549227_The_uncertain_future_of_the_Nile_Delta. (Accessed: 6th August 2023)

3. Smith, J. B. *et al.* Egypt's economic vulnerability to climate change. *Clim. Res.* **62**, 59–70 (2014).

4. Khamees, A. S., Rahoma, U. A., Hassan, A. H., Sayad, T. & Morsy, M. Investigation of Solar Energy Potential and PV-Outputs in Rural and Desert Areas: Case Study Egypt. doi:10.1088/1757-899X/1269/1/012006

5. Annual 2015 Global Climate Report | National Centers for Environmental Information (NCEI). Available at: https://www.ncei.noaa.gov/access/monitoring/monthly-report/global/201513. (Accessed: 21st August 2023)

6. Climate Change 2021: The Physical Science Basis | Climate Change 2021: The Physical Science Basis. Available at: https://www.ipcc.ch/report/ar6/wg1/. (Accessed: 6th August 2023)

7. Unfccc. ADOPTION OF THE PARIS AGREEMENT - Paris Agreement text English.

8. IRENA-International Renewable Energy Agency. World Energy Transitions Outlook: 1.5°C Pathway. *World Energy Transitions* 1–176 (2023).

9. Philipps, S., Ise, F., Warmuth, W. & Projects GmbH, P. Photovoltaics Report.

10. Correa-Baena, J. P. *et al.* Promises and challenges of perovskite solar cells. *Science (80-.).* **358**, 739–744 (2017).

11. Gao, P., Grätzel, M. & Nazeeruddin, M. K. Organohalide lead perovskites for photovoltaic applications. *Energy Environ. Sci.* **7**, 2448–2463 (2014).

12. Correa-Baena, J. P. *et al.* The rapid evolution of highly efficient perovskite solar cells. *Energy Environ. Sci.* **10**, 710–727 (2017).

13. A. Kojima, K. Teshima, Y. Shirai & T. Miyasaka. Organometal Halide Perovskites as Visible-Light Sensitizers for Photovoltaic Cells. *J. Am. Chem. Soc.* **131**, 6050–6051 (2009).

14. Best Research-Cell Efficiency Chart | Photovoltaic Research | NREL. Available at: https://www.nrel.gov/pv/cell-efficiency.html. (Accessed: 25th May 2021)

15. Yin, W. J., Shi, T. & Yan, Y. Superior Photovoltaic Properties of Lead Halide Perovskites: Insights from First-Principles Theory. *J. Phys. Chem. C* **119**, 5253–5264 (2015).

16. Egger, D. A. *et al.* What Remains Unexplained about the Properties of Halide Perovskites? *Adv. Mater.* **30**, 1800691 (2018).

17. Bera, S. *et al.* Review of defect engineering in perovskites for photovoltaic application. *Mater. Adv.* **3**, 5234–5247 (2022).

18. Eames, C. *et al.* Ionic transport in hybrid lead iodide perovskite solar cells. *Nat. Commun. 2015*

61 **6**, 1–8 (2015).

19. Abate, A. Perovskite Solar Cells Go Lead Free. doi:10.1016/j.joule.2017.09.007

20. Wang, X., Dong, B., Feng, M., Xue, D. J. & Wang, S. M. Sustainable management of lead in perovskite solar cells. *J. Mater. Chem. A* **10**, 15861–15864 (2022).

21. Byranvand, M. M., Zuo, W., Imani, R., Pazoki, M. & Saliba, M. Tin-based halide perovskite materials: properties and applications. *Chem. Sci.* **13**, 6766–6781 (2022).

22. Treglia, A. *et al.* Effect of electronic doping and traps on carrier dynamics in tin halide perovskites. *Mater. Horizons* **9**, 1763–1773 (2022).

23. Abate, A. Perovskite Solar Cells Go Lead Free. *Joule* **1**, 887 (2017).

24. DIRECTIVE 2002/95/EC OF THE EUROPEAN PARLIAMENT AND OF THE COUNCIL of 27 January 2003 on the restriction of the use of certain hazardous substances in electrical and electronic equipment.

25. Babayigit, A., Ethirajan, A., Muller, M. & Conings, B. Toxicity of organometal halide perovskite solar cells. *Nat. Mater. 2016 153* **15**, 247–251 (2016).

26. Van Der Voet, E. ; *et al.* General rights Environmental challenges of anthropogenic metals flows and cycles EnvironmEntal risks and ChallEngEs of anthropogEniC mEtals flows and CyClEs Acknowledgments. (2013).

27. Snaith, H. J. & Schmidt-Mende, L. Advances in Liquid-Electrolyte and Solid-State Dye-Sensitized Solar Cells. *Adv. Mater.* **19**, 3187–3200 (2007).

28. Im, J. H., Lee, C. R., Lee, J. W., Park, S. W. & Park, N. G. 6.5% efficient perovskite quantum-dot-sensitized solar cell. *Nanoscale* **3**, 4088–4093 (2011).

29. Lee, M. M., Teuscher, J., Miyasaka, T., Murakami, T. N. & Snaith, H. J. Efficient hybrid solar cells based on meso-superstructured organometal halide perovskites. *Science (80-.).* **338**, 643–647 (2012).

30. Heo, J. H. *et al.* Efficient inorganic–organic hybrid heterojunction solar cells containing perovskite compound and polymeric hole conductors. *Nat. Photonics 2013 76* **7**, 486–491 (2013).

31. Burschka, J. *et al.* Sequential deposition as a route to high-performance perovskite-sensitized solar cells. *Nat. 2013 4997458* **499**, 316–319 (2013).

32. Liu, M., Johnston, M. B. & Snaith, H. J. Efficient planar heterojunction perovskite solar cells by vapour deposition. *Nat. 2013 5017467* **501**, 395–398 (2013).

33. Zhou, H. *et al.* Interface engineering of highly efficient perovskite solar cells. *Science (80-.).* **345**, 542–546 (2014).

34. Yang, W. S. *et al.* High-performance photovoltaic perovskite layers fabricated through intramolecular exchange. *Science (80-.).* **348**, 1234–1237 (2015).

35. Saliba, M. *et al.* Incorporation of rubidium cations into perovskite solar cells improves photovoltaic performance. *Science (80-.).* **354**, 206–209 (2016).

36. Yang, W. S. *et al.* Iodide management in formamidinium-lead-halide-based perovskite layers for efficient solar cells. *Science (80-.).* **356**, 1376–1379 (2017).

37. Son, D. Y., Im, J. H., Kim, H. S. & Park, N. G. 11% efficient perovskite solar cell based on ZnO

nanorods: An effective charge collection system. *J. Phys. Chem. C* **118**, 16567–16573 (2014).

38. Mahmood, K. *et al.* Highly Efficient Hybrid Photovoltaics Based on Hyperbranched Three-Dimensional TiO2 Electron Transporting Materials. *Adv. Mater.* **27**, 2859–2865 (2015).

39. Luo, Q. *et al.* Discrete Iron(III) Oxide Nanoislands for Efficient and Photostable Perovskite Solar Cells. *Adv. Funct. Mater.* **27**, 1702090 (2017).

40. Bi, D. *et al.* Using a two-step deposition technique to prepare perovskite (CH3NH3PbI3) for thin film solar cells based on ZrO2 and TiO2 mesostructures. *RSC Adv.* **3**, 18762–18766 (2013).

41. Lee, K., Yoon, C. M., Noh, J. & Jang, J. Morphology-controlled mesoporous SiO2 nanorods for efficient scaffolds in organo-metal halide perovskite solar cells. *Chem. Commun.* **52**, 4231–4234 (2016).

42. Oh, L. S. *et al.* Zn2SnO4-based photoelectrodes for organolead halide perovskite solar cells. *J. Phys. Chem. C* **118**, 22991–22994 (2014).

43. Li, J., Wang, Q. & Abate, A. Perovskite solar cells. *Nanomater. Sol. Cell Appl.* 417–446 (2019). doi:10.1016/B978-0-12-813337-8.00012-6

44. Ke, W. *et al.* Lowerature solution-processed tin oxide as an alternative electron transporting layer for efficient perovskite solar cells. *J. Am. Chem. Soc.* **137**, 6730–6733 (2015).

45. Mali, S. S., Shim, C. S. & Hong, C. K. Highly stable and efficient solid-state solar cells based on methylammonium lead bromide (CH3NH3PbBr3) perovskite quantum dots. *NPG Asia Mater. 2015 78* **7**, e208–e208 (2015).

46. Qin, P. *et al.* Inorganic hole conductor-based lead halide perovskite solar cells with 12.4% conversion efficiency. *Nat. Commun. 2014 51* **5**, 1–6 (2014).

47. Christians, J. A., Fung, R. C. M. & Kamat, P. V. An inorganic hole conductor for Organo-lead halide perovskite solar cells. improved hole conductivity with copper iodide. *J. Am. Chem. Soc.* **136**, 758–764 (2014).

48. Jeng, J. Y. *et al.* CH3NH3PbI3 Perovskite/Fullerene Planar-Heterojunction Hybrid Solar Cells. *Adv. Mater.* **25**, 3727–3732 (2013).

49. Chiang, C. H., Tseng, Z. L. & Wu, C. G. Planar heterojunction perovskite/PC71BM solar cells with enhanced open-circuit voltage via a (2/1)-step spin-coating process. *J. Mater. Chem. A* **2**, 15897–15903 (2014).

50. Zheng, X. *et al.* Defect passivation in hybrid perovskite solar cells using quaternary ammonium halide anions and cations. *Nat. Energy 2017 27* **2**, 1–9 (2017).

51. Zhao, D. *et al.* High-Efficiency Solution-Processed Planar Perovskite Solar Cells with a Polymer Hole Transport Layer. *Adv. Energy Mater.* **5**, 1401855 (2015).

52. Ryu, S. *et al.* Voltage output of efficient perovskite solar cells with high open-circuit voltage and fill factor. *Energy Environ. Sci.* **7**, 2614–2618 (2014).

53. Huang, C. *et al.* Dopant-Free Hole-Transporting Material with a C3h Symmetrical Truxene Core for Highly Efficient Perovskite Solar Cells. *J. Am. Chem. Soc.* **138**, 2528–2531 (2016).

54. Park, I. J. *et al.* Highly Efficient and Uniform 1 cm2 Perovskite Solar Cells with an Electrochemically Deposited NiOx Hole-Extraction Layer. *ChemSusChem* **10**, 2660–2667 (2017).

55. Zuo, C. & Ding, L. Solution-Processed Cu2O and CuO as Hole Transport Materials for Efficient Perovskite Solar Cells. *Small* **11**, 5528–5532 (2015).

56. Qin, P.-L. *et al.* Copper-Doped Chromium Oxide Hole-Transporting Layer for Perovskite Solar Cells: Interface Engineering and Performance Improvement. *Adv. Mater. Interfaces* **3**, 1500799 (2016).

57. Green, M. A. *et al.* Solar cell efficiency tables (version 62). *Prog. Photovoltaics Res. Appl.* **31**, 651–663 (2023).

58. Nakane, A., Fujimoto, S. & Fujiwara, H. Fast determination of the current loss mechanisms in textured crystalline Si-based solar cells. *J. Appl. Phys.* **122**, 203101 (2017).

59. Kato, Y., Fujimoto, S., Kozawa, M. & Fujiwara, H. Maximum efficiencies and performance-limiting factors of inorganic and hybrid perovskite solar cells. *Phys. Rev. Appl.* **12**, 024039 (2019).

60. Hara, T. *et al.* Quantitative assessment of optical gain and loss in submicron-textured CuIn1-xGaxSe2 solar cells fabricated by three-stage coevaporation. *Phys. Rev. Appl.* **2**, 034012 (2014).

61. Saliba, M. *et al.* How to Make over 20% Efficient Perovskite Solar Cells in Regular (n-i-p) and Inverted (p-i-n) Architectures. *Chem. Mater.* **30**, 4193–4201 (2018).

62. Al-Attafi, K., Dwech, M. H., Mezher, H. A., Nattestad, A. & Kim, J. H. A Comparative Study of Organic Dye-Sensitized Solar Cells Based on Anatase TiO2 and Amorphous Free Mixed Phase's Anatase/Rutile P25 TiO2 Photoanodes. *Coatings* **13**, 121 (2023).

63. Docampo, P. *et al.* Control of Solid-State Dye-Sensitized Solar Cell Performance by Block-Copolymer-Directed TiO2 Synthesis. *Adv. Funct. Mater.* **20**, 1787–1796 (2010).

64. Singh, T., Miyasaka, T., Singh, T. & Miyasaka, T. Stabilizing the Efficiency Beyond 20% with a Mixed Cation Perovskite Solar Cell Fabricated in Ambient Air under Controlled Humidity. *Adv. Energy Mater.* **8**, 1700677 (2018).

65. Enhanced Reader.

66. Shirayama, M. *et al.* Optical Transitions in Hybrid Perovskite Solar Cells: Ellipsometry, Density Functional Theory, and Quantum Efficiency Analyses for CH3NH3PbI3. *Phys. Rev. Appl.* **5**, 014012 (2016).

67. Yamada, Y., Nakamura, T., Endo, M., Wakamiya, A. & Kanemitsu, Y. Photocarrier recombination dynamics in perovskite CH3NH 3PbI3 for solar cell applications. *J. Am. Chem. Soc.* **136**, 11610–11613 (2014).

68. Zhao, B. *et al.* High Open-Circuit Voltages in Tin-Rich Low-Bandgap Perovskite-Based Planar Heterojunction Photovoltaics. *Adv. Mater.* **29**, 1604744 (2017).

69. Y, H. *et al.* Efficient tandem solar cells with solution-processed perovskite on textured crystalline silicon. *Science* **367**, 1131–1134 (2020).

70. Chen, Z., Wang, J. J., Ren, Y., Yu, C. & Shum, K. Schottky solar cells based on CsSnI3 thin-films. *Appl. Phys. Lett.* **101**, 093901 (2012).

71. Zhang, M. *et al.* Recent advances in low-toxic lead-free metal halide perovskite materials for solar cell application. *Asia-Pacific J. Chem. Eng.* **11**, 392–398 (2016).

72. Hao, F., Stoumpos, C. C., Chang, R. P. H. & Kanatzidis, M. G. Anomalous band gap behavior in mixed Sn and Pb perovskites enables broadening of absorption spectrum in solar cells. *J. Am. Chem. Soc.* **136**, 8094–8099 (2014).

73. Yang, Z. *et al.* Stable Low-Bandgap Pb–Sn Binary Perovskites for Tandem Solar Cells. *Adv.*

Mater. **28**, 8990–8997 (2016).

74. Xing, G. *et al.* Long-range balanced electron-and hole-transport lengths in organic-inorganic CH3NH3PbI3. *Science (80-.).* **342**, 344–347 (2013).

75. Noel, N. K. *et al.* Lead-free organic–inorganic tin halide perovskites for photovoltaic applications. *Energy Environ. Sci.* **7**, 3061–3068 (2014).

76. Hemant Kumar, M. *et al.* Lead-Free Halide Perovskite Solar Cells with High Photocurrents Realized Through Vacancy Modulation. *Adv. Mater.* **26**, 7122–7127 (2014).

77. Rühle, S. Tabulated values of the Shockley–Queisser limit for single junction solar cells. *Sol. Energy* **130**, 139–147 (2016).

78. Zhao, Z. *et al.* Mixed-Organic-Cation Tin Iodide for Lead-Free Perovskite Solar Cells with an Efficiency of 8.12%. *Adv. Sci.* **4**, 1700204 (2017).

79. Song, T. Bin *et al.* Importance of reducing vapor atmosphere in the fabrication of Tin-based perovskite solar cells. *J. Am. Chem. Soc.* **139**, 836–842 (2017).

80. Lee, S. J. *et al.* Fabrication of Efficient Formamidinium Tin Iodide Perovskite Solar Cells through SnF2-Pyrazine Complex. *J. Am. Chem. Soc.* **138**, 3974–3977 (2016).

81. Tang, W. *et al.* Acetone-assisted precursor engineering enables low-temperature fabrication of CsPbI2Br perovskite for efficient solar cells. *J. Power Sources* **482**, 228965 (2021).

82. Wilk, B. *et al.* Green Solvent-Based Perovskite Precursor Development for Ink-Jet Printed Flexible Solar Cells. *ACS Sustain. Chem. Eng.* **9**, 3920–3930 (2021).

83. Liao, K. *et al.* Aqueous solvent-regulated crystallization and interfacial modification in perovskite solar cells with enhanced stability and performance. *J. Power Sources* **471**, 228447 (2020).

84. Li, Z. *et al.* Intermediates transformation for efficient perovskite solar cells. *J. Energy Chem.* **52**, 102–114 (2021).

85. Li, J. *et al.* Review on recent progress of lead-free halide perovskites in optoelectronic applications. *Nano Energy* **80**, 105526 (2021).

86. Zhang, J. *et al.* Binary Solvent Engineering for High-Performance Two-Dimensional Perovskite Solar Cells. *ACS Sustain. Chem. Eng.* **7**, 3487–3495 (2019).

87. Huang, S. H. *et al.* Controlling the Morphology and Interface of the Perovskite Layer for Scalable High-Efficiency Solar Cells Fabricated Using Green Solvents and Blade Coating in an Ambient Environment. *ACS Appl. Mater. Interfaces* **12**, 26041–26049 (2020).

88. Zhang, H. *et al.* Perovskite Photovoltaics: The Significant Role of Ligands in Film Formation, Passivation, and Stability. *Adv. Mater.* **31**, 1805702 (2019).

89. Castro, R. H. R. & Gouvêa, D. Sintering and Nanostability: The Thermodynamic Perspective. *J. Am. Ceram. Soc.* **99**, 1105–1121 (2016).

90. Nabika, H., Itatani, M. & Lagzi, I. Pattern Formation in Precipitation Reactions: The Liesegang Phenomenon. *Langmuir* **36**, 481–497 (2020).

91. Strey, R., Wagner, P. E. & Viisanen, Y. The problem of measuring homogeneous nucleation rates and the molecular contents of nuclei: Progress in the form of nucleation pulse measurements. *J. Phys. Chem.* **98**, 7748–7758 (1994).

92. Jung, M., Ji, S. G., Kim, G. & Seok, S. Il. Perovskite precursor solution chemistry: From fundamentals to photovoltaic applications. *Chemical Society Reviews* **48**, 2011–2038 (2019).

93. Lamer, V. K. & Dinegar, R. H. Theory, Production and Mechanism of Formation of Monodispersed Hydrosols.

94. Wu, K. J., Tse, E. C. M., Shang, C. & Guo, Z. Nucleation and growth in solution synthesis of nanostructures – From fundamentals to advanced applications. *Prog. Mater. Sci.* **123**, 100821 (2022).

95. Park, N. G. & Zhu, K. Scalable fabrication and coating methods for perovskite solar cells and solar modules. *Nat. Rev. Mater. 2020 55* **5**, 333–350 (2020).

96. Hoecker, C., Smail, F., Pick, M., Weller, L. & Boies, A. M. The Dependence of CNT Aerogel Synthesis on Sulfur-driven Catalyst Nucleation Processes and a Critical Catalyst Particle Mass Concentration. *Sci. Reports 2017 71* **7**, 1–11 (2017).

97. Kurasov, V. B. Theoretical justification of the von Weimarn law under homogeneous condensation in the free-molecular regime. *Tech. Phys. Lett.* **42**, 772–774 (2016).

98. Zhou, Y., Game, O. S., Pang, S. & Padture, N. P. Microstructures of Organometal Trihalide Perovskites for Solar Cells: Their Evolution from Solutions and Characterization. *J. Phys. Chem. Lett.* **6**, 4827–4839 (2015).

99. Yang, M. *et al.* Facile fabrication of large-grain CH3NH3PbI3−xBrx films for high-efficiency solar cells via CH3NH3Br-selective Ostwald ripening. *Nat. Commun. 2016 71* **7**, 1–9 (2016).

100. Mahmud, M. A. *et al.* Controlled Ostwald ripening mediated grain growth for smooth perovskite morphology and enhanced device performance. *Sol. Energy Mater. Sol. Cells* **167**, 87–101 (2017).

101. Roose, B. *et al.* Spontaneous crystal coalescence enables highly efficient perovskite solar cells. *Nano Energy* **39**, 24–29 (2017).

102. Kamaruddin, H. D. & Koros, W. J. Some observations about the application of Fick's first law for membrane separation of multicomponent mixtures. *J. Memb. Sci.* **135**, 147–159 (1997).

103. Li, B. *et al.* Engineering Halide Perovskite Crystals through Precursor Chemistry. *Small* **15**, 1903613 (2019).

104. Seo, Y. H., Kim, E. C., Cho, S. P., Kim, S. S. & Na, S. I. High-performance planar perovskite solar cells: Influence of solvent upon performance. *Appl. Mater. Today* **9**, 598–604 (2017).

105. Guo, X. *et al.* Identification and characterization of the intermediate phase in hybrid organic–inorganic MAPbI3 perovskite. *Dalt. Trans.* **45**, 3806–3813 (2016).

106. Lee, J. W. *et al.* Tuning Molecular Interactions for Highly Reproducible and Efficient Formamidinium Perovskite Solar Cells via Adduct Approach. *J. Am. Chem. Soc.* **140**, 6317–6324 (2018).

107. Ahn, N. *et al.* Highly Reproducible Perovskite Solar Cells with Average Efficiency of 18.3% and Best Efficiency of 19.7% Fabricated via Lewis Base Adduct of Lead(II) Iodide. *J. Am. Chem. Soc.* **137**, 8696–8699 (2015).

108. J. Clay Hamill, J., Schwartz, J. & Loo, Y.-L. Influence of Solvent Coordination on Hybrid Organic–Inorganic Perovskite Formation. *ACS Energy Lett.* **3**, 92–97 (2017).

109. Gutmann, V. Solvent effects on the reactivities of organometallic compounds. *Coord. Chem.*

Rev. **18**, 225–255 (1976).

110. Ozaki, M. *et al.* A Purified, Solvent-Intercalated Precursor Complex for Wide-Process-Window Fabrication of Efficient Perovskite Solar Cells and Modules. *Angew. Chemie* **131**, 9489–9493 (2019).

111. Qiu, J. *et al.* Rapid Crystallization for Efficient 2D Ruddlesden–Popper (2DRP) Perovskite Solar Cells. *Adv. Funct. Mater.* **29**, 1806831 (2019).

112. Baldan, A. Progress in Ostwald ripening theories and their applications to nickel-base superalloys. Part I: Ostwald ripening theories. *J. Mater. Sci.* **37**, 2171–2202 (2002).

113. Cao, X. *et al.* Fabrication of Perovskite Films with Large Columnar Grains via Solvent-Mediated Ostwald Ripening for Efficient Inverted Perovskite Solar Cells. *ACS Appl. Energy Mater.* **1**, 868–875 (2018).

114. Stamplecoskie, K. G., Manser, J. S. & Kamat, P. V. Dual nature of the excited state in organic–inorganic lead halide perovskites. *Energy Environ. Sci.* **8**, 208–215 (2014).

115. Sharenko, A., Mackeen, C., Jewell, L., Bridges, F. & Toney, M. F. Evolution of Iodoplumbate Complexes in Methylammonium Lead Iodide Perovskite Precursor Solutions. *Chem. Mater.* **29**, 1315–1320 (2017).

116. Cao, X. *et al.* Elucidating the Key Role of a Lewis Base Solvent in the Formation of Perovskite Films Fabricated from the Lewis Adduct Approach. *ACS Appl. Mater. Interfaces* **9**, 32868–32875 (2017).

117. Bai, Y. *et al.* A pure and stable intermediate phase is key to growing aligned and vertically monolithic perovskite crystals for efficient PIN planar perovskite solar cells with high processibility and stability. *Nano Energy* **34**, 58–68 (2017).

118. Kim, H. B. *et al.* Mixed solvents for the optimization of morphology in solution-processed, inverted-type perovskite/fullerene hybrid solar cells. *Nanoscale* **6**, 6679–6683 (2014).

119. Wu, Y. *et al.* Retarding the crystallization of PbI2 for highly reproducible planar-structured perovskite solar cells via sequential deposition. *Energy Environ. Sci.* **7**, 2934–2938 (2014).

120. Cao, J. *et al.* Identifying the Molecular Structures of Intermediates for Optimizing the Fabrication of High-Quality Perovskite Films. *J. Am. Chem. Soc.* **138**, 9919–9926 (2016).

121. Rong, Y. *et al.* Solvent engineering towards controlled grain growth in perovskite planar heterojunction solar cells. *Nanoscale* **7**, 10595–10599 (2015).

122. Jeon, N. J. *et al.* Solvent engineering for high-performance inorganic-organic hybrid perovskite solar cells. *Nat. Mater.* **13**, 897–903 (2014).

123. Yang, F. *et al.* Dependence of Acetate-Based Antisolvents for High Humidity Fabrication of CH3NH3PbI3 Perovskite Devices in Ambient Atmosphere. *ACS Appl. Mater. Interfaces* **10**, 16482–16489 (2018).

124. Paek, S. *et al.* From Nano- to Micrometer Scale: The Role of Antisolvent Treatment on High Performance Perovskite Solar Cells. *Chem. Mater.* **29**, 3490–3498 (2017).

125. Bu, T. *et al.* Synergic Interface Optimization with Green Solvent Engineering in Mixed Perovskite Solar Cells. *Adv. Energy Mater.* **7**, 1700576 (2017).

126. Kim, M. *et al.* Methylammonium Chloride Induces Intermediate Phase Stabilization for Efficient Perovskite Solar Cells. *Joule* **3**, 2179–2192 (2019).

127. Alsalloum, A. Y. *et al.* Low-Temperature Crystallization Enables 21.9% Efficient Single-Crystal MAPbI3 Inverted Perovskite Solar Cells. *ACS Energy Lett.* **5**, 657–662 (2020).

128. Hussein, M. *et al.* Challenges in tin perovskite solar cells. *Phys. Chem. Chem. Phys.* (2021). doi:10.1039/D1CP02596A

129. Park, M. W. & Yeo, S. Do. Antisolvent crystallization of carbamazepine from organic solutions. *Chem. Eng. Res. Des.* **90**, 2202–2208 (2012).

130. Woo, M. W., Mansouri, S. & Chen, X. D. Antisolvent vapor precipitation: the future of pulmonary drug delivery particle production? *https://doi.org/10.1517/17425247.2014.875527* **11**, 307–311 (2014).

131. Zhao, H., Wang, J. X., Wang, Q. A., Chen, J. F. & Yun, J. Controlled liquid antisolvent precipitation of hydrophobic pharmaceutical nanoparticles in a MicroChannel reactor. *Ind. Eng. Chem. Res.* **46**, 8229–8235 (2007).

132. Amaro-González, D., Mabe, G., Zabaloy, M. & Brignole, E. A. Gas antisolvent crystallization of organic salts from aqueous solutions. *J. Supercrit. Fluids* **17**, 249–258 (2000).

133. Chattopadhyay, P. & Gupta, R. B. Protein nanoparticles formation by supercritical antisolvent with enhanced mass transfer. *AIChE J.* **48**, 235–244 (2002).

134. Yeo, S. -D, Lim, G. -B, Debendetti, P. G. & Bernstein, H. Formation of microparticulate protein powder using a supercritical fluid antisolvent. *Biotechnol. Bioeng.* **41**, 341–346 (1993).

135. Reverchon, E., Adami, R., Caputo, G. & De Marco, I. Spherical microparticles production by supercritical antisolvent precipitation: Interpretation of results. *J. Supercrit. Fluids* **47**, 70–84 (2008).

136. Reverchon, E. Supercritical antisolvent precipitation of micro- and nano-particles. *J. Supercrit. Fluids* **15**, 1–21 (1999).

137. Oosterhof, H., Witkamp, G. J. & Van Rosmalen, G. M. Antisolvent crystallization of anhydrous sodium carbonate at atmospherical conditions. *AIChE J.* **47**, 602–608 (2001).

138. Randolph, T. W., Randolph, A. D., Mebes, M. & Yeung, S. Sub-Micrometer-Sized Biodegradable Particles of Poly(L-Lactic Acid) via the Gas Antisolvent Spray Precipitation Process. *Biotechnol. Prog.* **9**, 429–435 (1993).

139. Young, T. J., Johnston, K. P., Mishima, K. & Tanaka, H. Encapsulation of lysozyme in a biodegradable polymer by precipitation with a vapor-over-liquid antisolvent. *J. Pharm. Sci.* **88**, 640–650 (1999).

140. Wu, C. *et al.* Improved Performance and Stability of All-Inorganic Perovskite Light-Emitting Diodes by Antisolvent Vapor Treatment. *Adv. Funct. Mater.* **27**, 1700338 (2017).

141. Zhu, Y. *et al.* Very efficient green light-emitting diodes based on polycrystalline CH(NH3)2PbBr3 film achieved by regulating precursor concentration and employing novel anti-solvent. *Org. Electron.* **55**, 35–41 (2018).

142. Wang, Z., Huai, B., Yang, G., Wu, M. & Yu, J. High performance perovskite light-emitting diodes realized by isopropyl alcohol as green anti-solvent. *J. Lumin.* **204**, 110–115 (2018).

143. Wei, Z. *et al.* Inkjet Printing and Instant Chemical Transformation of a CH3NH3PbI3/Nanocarbon Electrode and Interface for Planar Perovskite Solar Cells. *Angew. Chemie Int. Ed.* **53**, 13239–13243 (2014).

144. Barrows, A. T. *et al.* Efficient planar heterojunction mixed-halide perovskite solar cells deposited via spray-deposition. *Energy Environ. Sci.* **7**, 2944–2950 (2014).

145. Xiao, M. *et al.* A Fast Deposition-Crystallization Procedure for Highly Efficient Lead Iodide Perovskite Thin-Film Solar Cells. *Angew. Chemie Int. Ed.* **53**, 9898–9903 (2014).

146. Taylor, A. D. *et al.* A general approach to high-efficiency perovskite solar cells by any antisolvent. *Nat. Commun. 2021 121* **12**, 1–11 (2021).

147. Qiu, X. *et al.* Lead-free mesoscopic Cs2SnI6 perovskite solar cells using different nanostructured ZnO nanorods as electron transport layers. *Phys. status solidi – Rapid Res. Lett.* **10**, 587–591 (2016).

148. Wang, M. *et al.* High-Quality Sequential-Vapor-Deposited Cs2AgBiBr6 Thin Films for Lead-Free Perovskite Solar Cells. *Sol. RRL* **2**, 1800217 (2018).

149. Jiang, F. *et al.* Chlorine-Incorporation-Induced Formation of the Layered Phase for Antimony-Based Lead-Free Perovskite Solar Cells. *J. Am. Chem. Soc.* **140**, 1019–1027 (2018).

150. Krishnamoorthy, T. *et al.* Lead-free germanium iodide perovskite materials for photovoltaic applications. *J. Mater. Chem. A* **3**, 23829–23832 (2015).

151. Lee, S. J. *et al.* Fabrication of Efficient Formamidinium Tin Iodide Perovskite Solar Cells through SnF_2–Pyrazine Complex. *J. Am. Chem. Soc.* **138**, 3974–3977 (2016).

152. Yin, M. *et al.* Annealing-free perovskite films by instant crystallization for efficient solar cells. *J. Mater. Chem. A* **4**, 8548–8553 (2016).

153. Zhang, F. *et al.* sec-Butyl alcohol assisted pinhole-free perovskite film growth for high-performance solar cells. *J. Mater. Chem. A* **4**, 3438–3445 (2016).

154. Li, S. *et al.* Entire mirror-like perovskite films for high-performance perovskite solar cells: The role of polar anti-solvent sec-pentyl alcohol. *Org. Electron.* **57**, 133–139 (2018).

155. Fang, F., Chen, J., Wu, G. & Chen, H. Highly efficient perovskite solar cells fabricated by simplified one-step deposition method with non-halogenated anti-solvents. *Org. Electron.* **59**, 330–336 (2018).

156. Yavari, M. *et al.* Greener, Nonhalogenated Solvent Systems for Highly Efficient Perovskite Solar Cells. *Adv. Energy Mater.* **8**, 1800177 (2018).

157. Zhao, P. *et al.* Antisolvent with an Ultrawide Processing Window for the One-Step Fabrication of Efficient and Large-Area Perovskite Solar Cells. *Adv. Mater.* **30**, 1802763 (2018).

158. Wang, M. *et al.* Improving the Performance and Reproducibility of Inverted Planar Perovskite Solar Cells Using Tetraethyl Orthosilicate as the Antisolvent. *ACS Appl. Mater. Interfaces* **11**, 3909–3916 (2019).

159. Wang, M. *et al.* Systematic optimization of perovskite solar cells via green solvent systems. *Chem. Eng. J.* **387**, 123966 (2020).

160. Gonzalez-Pedro, V. *et al.* General working principles of CH3NH3PbX3 perovskite solar cells. *Nano Lett.* **14**, 888–893 (2014).

161. Wang, M., Grätzel, C., Zakeeruddin, S. M. & Grätzel, M. Recent developments in redox electrolytes for dye-sensitized solar cells. *Energy Environ. Sci.* **5**, 9394–9405 (2012).

162. Cai, B., Xing, Y., Yang, Z., Zhang, W. H. & Qiu, J. High performance hybrid solar cells sensitized by organolead halide perovskites. *Energy Environ. Sci.* **6**, 1480–1485 (2013).

163. Wang, H. *et al.* Band-Bending in Organic Semiconductors: the Role of Alkali-Halide Interlayers. *Adv. Mater.* **26**, 925–930 (2014).

164. Shi, J., Xu, X., Li, D. & Meng, Q. Interfaces in Perovskite Solar Cells. *Small* **11**, 2472–2486 (2015).

165. Zhou, Z., Pang, S., Liu, Z., Xu, H. & Cui, G. Interface engineering for high-performance perovskite hybrid solar cells. *J. Mater. Chem. A* **3**, 19205–19217 (2015).

166. Zhang, X. *et al.* The Voltage Loss in Tin Halide Perovskite Solar Cells: Origins and Perspectives. *Adv. Funct. Mater.* **32**, 2108832 (2022).

167. Wang, Q.-K. *et al.* Energy Level Offsets at Lead Halide Perovskite/Organic Hybrid Interfaces and Their Impacts on Charge Separation. *Adv. Mater. Interfaces* **2**, 1400528 (2015).

168. Shockley, W. & Queisser, H. J. Detailed Balance Limit of Efficiency of p-n Junction Solar Cells. *J. Appl. Phys.* **32**, 510–519 (1961).

169. Herz, L. M. Charge-Carrier Mobilities in Metal Halide Perovskites: Fundamental Mechanisms and Limits. *ACS Energy Lett.* **2**, 1539–1548 (2017).

170. Li, M. *et al.* Advances in Tin(II)-Based Perovskite Solar Cells: From Material Physics to Device Performance. *Small Struct.* **3**, 2100102 (2022).

171. Goyal, A. *et al.* Origin of Pronounced Nonlinear Band Gap Behavior in Lead-Tin Hybrid Perovskite Alloys. *Chem. Mater.* **30**, 3920–3928 (2018).

172. Tao, S. *et al.* Absolute energy level positions in tin- and lead-based halide perovskites. *Nat. Commun.* **10**, 1–10 (2019).

173. Lanzetta, L. *et al.* Degradation mechanism of hybrid tin-based perovskite solar cells and the critical role of tin (IV) iodide. *Nat. Commun. 2021 121* **12**, 1–11 (2021).

174. Li, B. *et al.* Tin-Based Defects and Passivation Strategies in Tin-Related Perovskite Solar Cells. *ACS Energy Lett.* **5**, 3752–3772 (2020).

175. Liu, J. *et al.* Lead-Free Solar Cells based on Tin Halide Perovskite Films with High Coverage and Improved Aggregation. *Angew. Chemie Int. Ed.* **57**, 13221–13225 (2018).

176. Kanemitsu, Y., Wakamiya, A., Nakamura, T., Handa, T. & Murdey, R. Materials chemistry approach for efficient lead-free tin halide perovskite solar cells. *ACS Appl. Electron. Mater.* **2**, 3794–3804 (2020).

177. Wu, T. *et al.* Lead-free tin perovskite solar cells. *Joule* **5**, 863–886 (2021).

178. Gu, F. *et al.* Improving Performance of Lead-Free Formamidinium Tin Triiodide Perovskite Solar Cells by Tin Source Purification. *Sol. RRL* **2**, 1800136 (2018).

179. Roberto Bautista-Quijano, J., Oscar Telschow, Fabian Paulus & Yana Vaynzof. Solvent–antisolvent interactions in metal halide perovskites. *Chem. Commun.* (2023). doi:10.1039/D3CC02090H

180. Solubility of non-electrolytes. By J. H. Hildebrand, Ph.D. 2nd ed. Pp. 203. New York: Reinhold Publishing Corp., London: Chapman & Hall, Ltd., 1936. 22s. 6d. *J. Soc. Chem. Ind.* **55**, 665–665 (1936).

181. Hansen, C. M. & Just, L. Prediction of Environmental Stress Cracking in Plastics with Hansen Solubility Parameters. *Ind. Eng. Chem. Res.* **40**, 21–25 (2000).

182. Hansen, C. M. On predicting environmental stress cracking in polymers. *Polym. Degrad. Stab.* **77**, 43–53 (2002).

183. Weng, M. Effect of optimization methods on Hansen solubility ellipsoids. *J. Appl. Polym. Sci.* **134**, 44621 (2017).

184. Schweizer, T., Kubach, H. & Koch, · Thomas. Investigations to characterize the interactions of light radiation, engine operating media and fluorescence tracers for the use of qualitative light-induced fluorescence in engine systems. *Automot. Engine Technol. 2021 63* **6**, 275–287 (2021).

185. Ishii, H. & Ishii, H. Photoelectron Yield Spectroscopy. *Compend. Surf. Interface Anal.* 457–463 (2018). doi:10.1007/978-981-10-6156-1_75

186. Ishii, H. & Ishii, H. Photoelectron Yield Spectroscopy. *Compend. Surf. Interface Anal.* 457–463 (2018). doi:10.1007/978-981-10-6156-1_75

187. Kronik, L. & Shapira, Y. Surface photovoltage phenomena: theory, experiment, and applications. *Surf. Sci. Rep.* **37**, 1–206 (1999).

188. M.R.I., L. K. G. C. V. O. D. C. L. L. D. F. R. S. V. Contact electricity of metals. *https://doi.org/10.1080/14786449808621172* **46**, 82–120 (2009).

189. Zisman, W. A. A NEW METHOD OF MEASURING CONTACT POTENTIAL DIFFERENCES IN METALS. *Rev. Sci. Instrum.* **3**, 367–370 (1932).

190. Besocke, K. & Berger, S. Piezoelectric driven Kelvin probe for contact potential difference studies. *RScI* **47**, 840–842 (1976).

191. Schroder, D. K. Surface voltage and surface photovoltage: history, theory andapplications. *Meas. Sci. Technol.* **12**, R16 (2001).

192. Kronik, L. & Shapira, Y. Surface photovoltage spectroscopy of semiconductor structures: at the crossroads of physics, chemistry and electrical engineering. *Surf. Interface Anal.* **31**, 954–965 (2001).

193. Cavalcoli, D. & Fazio, M. A. Electronic transitions in low dimensional semiconductor structures measured by surface photovoltage spectroscopy. *Mater. Sci. Semicond. Process.* **92**, 28–38 (2019).

194. Donchev, V. *et al.* Surface photovoltage spectroscopy study of InAs quantum dot in quantum well multilayer structures for infrared photodetectors. *Superlattices Microstruct.* **88**, 711–722 (2015).

195. Donchev, V. Surface photovoltage spectroscopy of semiconductor materials for optoelectronic applications. *Mater. Res. Express* **6**, 103001 (2019).

196. Souto, J. *et al.* Surface photovoltage spectroscopy characterization of AlGaAs/GaAs laser structures. *J. Phys. Conf. Ser.* **792**, 012021 (2017).

197. Donchev, V., Georgiev, S., Leontis, I. & Nassiopoulou, A. G. Effective Removal of Surface Recombination Centers in Silicon Nanowires Fabricated by Metal-Assisted Chemical Etching. *ACS Appl. Energy Mater.* **1**, 3693–3701 (2018).

198. Wang, Q., Phung, N., Di Girolamo, D., Vivo, P. & Abate, A. Enhancement in lifespan of halide perovskite solar cells. *Energy Environ. Sci.* **12**, 865–886 (2019).

199. Mei, A. *et al.* Stabilizing Perovskite Solar Cells to IEC61215:2016 Standards with over 9,000-h

Operational Tracking HIGHLIGHTS Printable PSCs pass IEC qualification tests with a 9,000-h operational tracking MAPbI 3 degrades at grain boundaries and 5-AVA strengthens the boundaries 5-AVA inhibits the MAI loss and crystal reconstruction 5-AVA inhibits irreversible ionic migration Stabilizing Perovskite Solar Cells to IEC61215:2016 Standards with over 9,000-h Operational Tracking. (2020). doi:10.1016/j.joule.2020.09.010

200. Di Girolamo, D. *et al.* Stability and Dark Hysteresis Correlate in NiO-Based Perovskite Solar Cells. *Adv. Energy Mater.* **9**, 1901642 (2019).

201. Deng, W., Liang, X., Kubiak, P. S. & Cameron, P. J. Molecular Interlayers in Hybrid Perovskite Solar Cells. *Adv. Energy Mater.* **8**, 1701544 (2018).

202. Wu, S. *et al.* A chemically inert bismuth interlayer enhances long-term stability of inverted perovskite solar cells. *Nat. Commun.* **10**, (2019).

203. Saliba, M. *et al.* Cesium-containing triple cation perovskite solar cells: improved stability, reproducibility and high efficiency. *Energy Environ. Sci.* **9**, 1989–1997 (2016).

204. Turren-Cruz, S. H., Hagfeldt, A. & Saliba, M. Methylammonium-free, high-performance, and stable perovskite solar cells on a planar architecture. *Science (80-.).* **362**, 449–453 (2018).

205. Shi, L. *et al.* Gas chromatography-mass spectrometry analyses of encapsulated stable perovskite solar cells. *Science (80-.).* **368**, (2020).

206. Hu, X. *et al.* Nacre-inspired crystallization and elastic “brick-and-mortar” structure for a wearable perovskite solar module. *Energy Environ. Sci.* **12**, 979–987 (2019).

207. Castro-Hermosa, S. *et al.* Perovskite Photovoltaics on Roll-To-Roll Coated Ultra-thin Glass as Flexible High-Efficiency Indoor Power Generators. *Cell Reports Phys. Sci.* **1**, 100045 (2020).

208. Batmunkh, M. *et al.* Recent Advances in Perovskite-Based Building-Integrated Photovoltaics. *Adv. Mater.* **32**, 2000631 (2020).

209. Li, J. *et al.* Biological impact of lead from halide perovskites reveals the risk of introducing a safe threshold. *Nat. Commun. 2020 111* **11**, 1–5 (2020).

210. Li, X. *et al.* On-device lead sequestration for perovskite solar cells. *Nat. 2020 5787796* **578**, 555–558 (2020).

211. Nasti, G., Abate, A., Nasti, G. & Abate, A. Tin Halide Perovskite (ASnX3) Solar Cells: A Comprehensive Guide toward the Highest Power Conversion Efficiency. *Adv. Energy Mater.* **10**, 1902467 (2020).

212. Zhou, J. *et al.* Chemo-thermal surface dedoping for high-performance tin perovskite solar cells. *Matter* (2022). doi:10.1016/J.MATT.2021.12.013

213. Li, M. *et al.* Tin Halide Perovskite Films Made of Highly Oriented 2D Crystals Enable More Efficient and Stable Lead-free Perovskite Solar Cells. *ACS Energy Lett.* **5**, 1923–1929 (2020).

214. Meggiolaro, D., Ricciarelli, D., Alasmari, A. A., Alasmary, F. A. S. & De Angelis, F. Tin versus Lead Redox Chemistry Modulates Charge Trapping and Self-Doping in Tin/Lead Iodide Perovskites. *J. Phys. Chem. Lett.* **11**, 3546–3556 (2020).

215. Gupta, S., Cahen, D. & Hodes, G. How SnF2 Impacts the Material Properties of Lead-Free Tin Perovskites. *J. Phys. Chem. C* **122**, 13926–13936 (2018).

216. Saidaminov, M. I. *et al.* Conventional Solvent Oxidizes Sn(II) in Perovskite Inks. *ACS Energy Lett.* **5**, 1153–1155 (2020).

217. Pascual, J. *et al.* Origin of Sn(II) oxidation in tin halide perovskites. *Mater. Adv.* **1**, 1066–1070 (2020).

218. Moine, E., Privat, R., Sirjean, B. & Jaubert, J. N. Estimation of solvation quantities from experimental thermodynamic data: Development of the comprehensive CompSol databank for pure and mixed solutes. *J. Phys. Chem. Ref. Data* **46**, (2017).

219. Cataldo, F. Gutmann donor numbers of phosphoramides Section E-Research paper Eur. *Chem. Bull* **4**, 92–97 (2015).

220. Noel, N. K. *et al.* A low viscosity, low boiling point, clean solvent system for the rapid crystallisation of highly specular perovskite films. *Energy Environ. Sci.* **10**, 145–152 (2017).

221. Saliba, M. *et al.* How to Make over 20% Efficient Perovskite Solar Cells in Regular (n-i-p) and Inverted (p-i-n) Architectures. *Chem. Mater.* **30**, 4193–4201 (2018).

222. Hansen, C. M. Methods of characterization - surfaces. *Hansen Solubility Parameters A Users Handbook, Second Ed.* 113–123 (2007). doi:10.1201/9781420006834/HANSEN-SOLUBILITY-PARAMETERS-CHARLES-HANSEN

223. Wang, J. *et al.* Highly Efficient Perovskite Solar Cells Using Non-Toxic Industry Compatible Solvent System. *Sol. RRL* **1**, 1700091 (2017).

224. Radicchi, E., Mosconi, E., Elisei, F., Nunzi, F. & De Angelis, F. Understanding the Solution Chemistry of Lead Halide Perovskites Precursors. *ACS Appl. Energy Mater.* **2**, 3400–3409 (2019).

225. Koh, T. M. *et al.* Formamidinium tin-based perovskite with low Eg for photovoltaic applications. *J. Mater. Chem. A* **3**, 14996–15000 (2015).

226. Ozaki, M. *et al.* Solvent-coordinated tin halide complexes as purified precursors for tin-based perovskites. *ACS Omega* **2**, 7016–7021 (2017).

227. Zhu, Z. *et al.* Realizing Efficient Lead-Free Formamidinium Tin Triiodide Perovskite Solar Cells via a Sequential Deposition Route. *Adv. Mater.* **30**, 1703800 (2018).

228. Kubicki, D. J. *et al.* Local Structure and Dynamics in Methylammonium, Formamidinium, and Cesium Tin(II) Mixed-Halide Perovskites from 119Sn Solid-State NMR. *J. Am. Chem. Soc.* **142**, 7813–7826 (2020).

229. Van Gompel, W. T. M. *et al.* Degradation of the Formamidinium Cation and the Quantification of the Formamidinium-Methylammonium Ratio in Lead Iodide Hybrid Perovskites by Nuclear Magnetic Resonance Spectroscopy. *J. Phys. Chem. C* **122**, 4117–4124 (2018).

230. Tan, S. *et al.* Surface Reconstruction of Halide Perovskites during Post-treatment. *J. Am. Chem. Soc.* **143**, 6781–6786 (2021).

231. Snaith, H. J. Present status and future prospects of perovskite photovoltaics. *Nat. Mater.* **17**, (2018).

232. Yoo, J. J. *et al.* Efficient perovskite solar cells via improved carrier management. *Nat. 2021 5907847* **590**, 587–593 (2021).

233. Kwak, J. Il, Kim, L. & An, Y. J. Sublethal toxicity of PbI2 in perovskite solar cells to fish embryos (Danio rerio and Oryzias latipes): Deformity and growth inhibition. *Sci. Total Environ.* **771**, (2021).

234. Zhai, Y., Wang, Z., Wang, G., Peijnenburg, W. J. G. M. & Vijver, M. G. The fate and toxicity of

Pb-based perovskite nanoparticles on soil bacterial community: Impacts of pH, humic acid, and divalent cations. *Chemosphere* **249**, 126564 (2020).

235. Wang, G. *et al.* An across-species comparison of the sensitivity of different organisms to Pb-based perovskites used in solar cells. *Sci. Total Environ.* **708**, 135134 (2020).

236. Patsiou, D. *et al.* Exposure to Pb-halide perovskite nanoparticles can deliver bioavailable Pb but does not alter endogenous gut microbiota in zebrafish. *Sci. Total Environ.* **715**, (2020).

237. Bae, S. Y. *et al.* Hazard potential of perovskite solar cell technology for potential implementation of "safe-by-design" approach. *Sci. Reports 2019 91* **9**, 1–9 (2019).

238. Babayigit, A. *et al.* Assessing the toxicity of Pb- and Sn-based perovskite solar cells in model organism Danio rerio. *Sci. Reports 2016 61* **6**, 1–11 (2016).

239. Duan, L. & Uddin, A. Defects and stability of perovskite solar cells: a critical analysis. *Mater. Chem. Front.* **6**, 400–417 (2022).

240. Dey, K., Roose, B. & Stranks, S. D. Optoelectronic Properties of Low-Bandgap Halide Perovskites for Solar Cell Applications. *Adv. Mater.* **33**, (2021).

241. Jiang, X. *et al.* One-Step Synthesis of SnI2·(DMSO)x Adducts for High-Performance Tin Perovskite Solar Cells. *J. Am. Chem. Soc.* **143**, 10970–10976 (2021).

242. Yu, B. Bin *et al.* Heterogeneous 2D/3D Tin-Halides Perovskite Solar Cells with Certified Conversion Efficiency Breaking 14%. *Adv. Mater.* **33**, 2102055 (2021).

243. Liu, X. *et al.* Interface Energy-Level Management toward Efficient Tin Perovskite Solar Cells with Hole-Transport-Layer-Free Structure. *Adv. Funct. Mater.* **31**, 2106560 (2021).

244. Wang, J. *et al.* Controlling the Crystallization Kinetics of Lead-Free Tin Halide Perovskites for High Performance Green Photovoltaics. *Adv. Energy Mater.* **11**, 2102131 (2021).

245. Awais, M., Kirsch, R. L., Yeddu, V. & Saidaminov, M. I. Tin Halide Perovskites Going Forward: Frost Diagrams Offer Hints. *ACS Mater. Lett.* **3**, 299–307 (2021).

246. Pascual, J. *et al.* Lights and Shadows of DMSO as Solvent for Tin Halide Perovskites. *Chem. – A Eur. J.* **28**, e202103919 (2022).

247. Girolamo, D. Di *et al.* Solvents for Processing Stable Tin Halide Perovskites. *ACS Energy Lett.* **6**, 959–968 (2021).

248. Chao, L. *et al.* Solvent Engineering of the Precursor Solution toward Large-Area Production of Perovskite Solar Cells. *Adv. Mater.* **33**, (2021).

249. Habisreutinger, S. N., Noel, N. K., Snaith, H. J. & Nicholas, R. J. Investigating the Role of 4-Tert Butylpyridine in Perovskite Solar Cells. *Adv. Energy Mater.* **7**, 1601079 (2017).

250. Rafiei Rad, R., Azizollah Ganji, B. & Taghavinia, N. 4-tert-butyl pyridine additive for moisture-resistant wide bandgap perovskite solar cells. *Opt. Mater. (Amst).* **123**, 111876 (2022).

251. Matczak, P. N → Sn coordination in the complexes of tin halides with pyridine: A comparison between Sn(II) and Sn(IV). *Appl. Organomet. Chem.* **33**, e4811 (2019).

252. Flatken, M. A. *et al.* Small-angle scattering to reveal the colloidal nature of halide perovskite precursor solutions. *J. Mater. Chem. A* **9**, 13477–13482 (2021).

253. Flatken, M. A. *et al.* Role of the Alkali Metal Cation in the Early Stages of Crystallization of Halide Perovskites. *Chem. Mater.* **34**, 1121–1131 (2022).

254. Niemann, R. G. *et al.* Halogen Effects on Ordering and Bonding of CH3NH3+ in CH3NH3PbX3 (X = Cl, Br, I) Hybrid Perovskites: A Vibrational Spectroscopic Study. *J. Phys. Chem. C* **120**, 2509–2519 (2016).

255. Quarti, C. *et al.* The raman spectrum of the CH3NH3PbI3 hybrid perovskite: Interplay of theory and experiment. *J. Phys. Chem. Lett.* **5**, 279–284 (2014).

256. Pistor, P., Ruiz, A., Cabot, A. & Izquierdo-Roca, V. Advanced Raman Spectroscopy of Methylammonium Lead Iodide: Development of a Non-destructive Characterisation Methodology. *Sci. Reports 2016 61* **6**, 1–8 (2016).

257. Pitaro, M., Tekelenburg, E. K., Shao, S. & Loi, M. A. Tin Halide Perovskites: From Fundamental Properties to Solar Cells. *Adv. Mater.* **34**, (2022).

258. Li, G. *et al.* Highly efficient p-i-n perovskite solar cells that endure temperature variations. *Science (80-.).* **379**, 399–403 (2023).

259. Gao, W., Li, P., Chen, J., Ran, C. & Wu, Z. Interface Engineering in Tin Perovskite Solar Cells. *Adv. Mater. Interfaces* **6**, 1901322 (2019).

260. Chen, N. *et al.* Universal Band Alignment Rule for Perovskite/Organic Heterojunction Interfaces. *ACS Energy Lett.* 1313–1321 (2023). doi:10.1021/ACSENERGYLETT.2C02856

261. Liu, H. *et al.* Pure Tin Halide Perovskite Solar Cells: Focusing on Preparation and Strategies. *Adv. Energy Mater.* 2202209 (2022). doi:10.1002/AENM.202202209

262. Lee, M. *et al.* Indene-C60Bisadduct Electron-Transporting Material with the High LUMO Level Enhances Open-Circuit Voltage and Efficiency of Tin-Based Perovskite Solar Cells. *ACS Appl. Energy Mater.* **3**, 5581–5588 (2020).

263. Chen, Y. *et al.* Mitigating Voc Loss in Tin Perovskite Solar Cells via Simultaneous Suppression of Bulk and Interface Nonradiative Recombination. *ACS Appl. Mater. Interfaces* (2022). doi:10.1021/ACSAMI.2C12129

264. Wu, T. *et al.* Efficient and Stable Tin Perovskite Solar Cells Enabled by Graded Heterostructure of Light-Absorbing Layer. *Sol. RRL* **4**, 2000240 (2020).

265. Li, B. *et al.* Efficient and Stable Tin Perovskite Solar Cells by Pyridine-Functionalized Fullerene with Reduced Interfacial Energy Loss. *Adv. Funct. Mater.* **32**, 2205870 (2022).

266. Li, H. *et al.* Surface Reconstruction for Tin-Based Perovskite Solar Cells. *ACS Energy Lett.* 3889–3899 (2022). doi:10.1021/ACSENERGYLETT.2C01624

267. Li, P. *et al.* Synergistic trifluoroacetamide regulating crystal orientation and energy alignment for tin-based perovskite solar cells. *Org. Electron.* **113**, 106707 (2023).

268. Zhang, Z. *et al.* Sequential Passivation for Lead-Free Tin Perovskite Solar Cells with High Efficiency. *Angew. Chemie* **134**, e202210101 (2022).

269. Rono, N., Merad, A. E., Kibet, J. K., Martincigh, B. S. & Nyamori, V. O. A theoretical investigation of the effect of the hole and electron transport materials on the performance of a lead-free perovskite solar cell based on CH3NH3SnI3. *J. Comput. Electron.* **20**, 993–1005 (2021).

270. Hossain, M. K. *et al.* An extensive study on multiple ETL and HTL layers to design and simulation of high-performance lead-free CsSnCl3-based perovskite solar cells. *Sci. Reports 2023 131* **13**, 1–24 (2023).

271. Roy, P., Raoui, Y. & Khare, A. Design and simulation of efficient tin based perovskite solar cells through optimization of selective layers: Theoretical insights. *Opt. Mater. (Amst).* **125**, 112057 (2022).

272. Abdelaziz, S., Zekry, A., Shaker, A. & Abouelatta, M. Investigating the performance of formamidinium tin-based perovskite solar cell by SCAPS device simulation. *Opt. Mater. (Amst).* **101**, 109738 (2020).

273. Li, G., Xu, M., Chen, Z. & Zou, X. Design and simulation investigations on electron transport layer-free in tin-based p-n homojunction perovskite solar cells. *Mater. Today Commun.* **35**, 106232 (2023).

274. Liang, K. *et al.* Rational design of formamidine tin-based perovskite solar cell with 30% potential efficiency via 1-D device simulation. *Phys. Chem. Chem. Phys.* **25**, 9413–9427 (2023).

275. Lee, Y. J., Wang, J. & Hsu, J. W. P. Surface photovoltage characterization of organic photovoltaic devices. *Appl. Phys. Lett.* **103**, 173302 (2013).

276. Levine, I. *et al.* Charge transfer rates and electron trapping at buried interfaces of perovskite solar cells. *Joule* **5**, 2915–2933 (2021).

277. Cavalcoli, D. & Cavallini, A. Surface photovoltage spectroscopy -method and applications. *Phys. Status Solidi Curr. Top. Solid State Phys.* **7**, 1293–1300 (2010).

278. Jiang, X. *et al.* Tin Halide Perovskite Solar Cells: An Emerging Thin-Film Photovoltaic Technology. *Accounts Mater. Res.* **2**, 210–219 (2021).

279. Peng, L. & Xie, W. Theoretical and experimental investigations on the bulk photovoltaic effect in lead-free perovskites MASnI 3 and FASnI 3. *RSC Adv.* **10**, 14679–14688 (2020).

280. Rusu, M. *et al.* Electronic Structure of the CdS/Cu(In,Ga)Se2Interface of KF- And RbF-Treated Samples by Kelvin Probe and Photoelectron Yield Spectroscopy. *ACS Appl. Mater. Interfaces* **13**, 7745–7755 (2021).

281. Wu, Y. *et al.* General Method to Define the Type of Carrier Transport Materials for Perovskite Solar Cells via Kelvin Probes Microscopy. *ACS Appl. Energy Mater.* **1**, 3984–3991 (2018).

282. Zhu, H. L. *et al.* Room-Temperature Solution-Processed NiOx:PbI2 Nanocomposite Structures for Realizing High-Performance Perovskite Photodetectors. *ACS Nano* **10**, 6808–6815 (2016).

283. Liu, Y., Qi, J., Peng, X. & Cao, Y. Alcohol soluble porphyrin for the cathode buffer layers of fullerene/perovskite planar heterojunction solar cells. *Org. Electron.* **59**, 414–418 (2018).

284. Yang, Z. *et al.* Review on Practical Interface Engineering of Perovskite Solar Cells: From Efficiency to Stability. *Sol. RRL* **4**, 1900257 (2020).

285. Nishimura, K. *et al.* Lead-free tin-halide perovskite solar cells with 13% efficiency. *Nano Energy* **74**, 104858 (2020).

286. Ying, Z. *et al.* Bathocuproine:Ag Complex Functionalized Tunneling Junction for Efficient Monolithic Perovskite/TOPCon Silicon Tandem Solar Cell. *Sol. RRL* **6**, 2200793 (2022).

287. Ying, Z. *et al.* Charge-transfer induced multifunctional BCP:Ag complexes for semi-transparent perovskite solar cells with a record fill factor of 80.1%. *J. Mater. Chem. A* **9**, 12009–12018 (2021).

288. Wang, S. *et al.* Favorable electronic structure for organic solar cells induced by strong interaction at interface. *J. Appl. Phys.* **114**, 183707 (2013).

289. Chen, K. *et al.* Low-dimensional perovskite interlayer for highly efficient lead-free formamidinium tin iodide perovskite solar cells. *Nano Energy* **49**, 411–418 (2018).

290. Shih, C. C. & Wu, C. G. Synergistic Engineering of the Conductivity and Surface Properties of PEDOT:PSS-Based HTLs for Inverted Tin Perovskite Solar Cells to Achieve Efficiency over 10%. *ACS Appl. Mater. Interfaces* **14**, 16125–16135 (2022).

291. Song, D., Narra, S., Li, M. Y., Lin, J. S. & Diau, E. W. G. Interfacial Engineering with a Hole-Selective Self-Assembled Monolayer for Tin Perovskite Solar Cells via a Two-Step Fabrication. *ACS Energy Lett.* **6**, 4179–4186 (2021).

292. Liang, P. W., Chueh, C. C., Williams, S. T. & Jen, A. K. Y. Roles of Fullerene-Based Interlayers in Enhancing the Performance of Organometal Perovskite Thin-Film Solar Cells. *Adv. Energy Mater.* **5**, 1402321 (2015).

293. Kafedjiska, I. *et al.* Disentangling the effect of the hole-transporting layer, the bottom, and the top device on the fill factor in monolithic CIGSe-perovskite tandem solar cells by using spectroscopic and imaging tools. *J. Phys. Energy* **5**, 024014 (2023).

10. APPENDIX

10.1 A1: Supporting Information: Chapter 5

The full list of tested solvents.

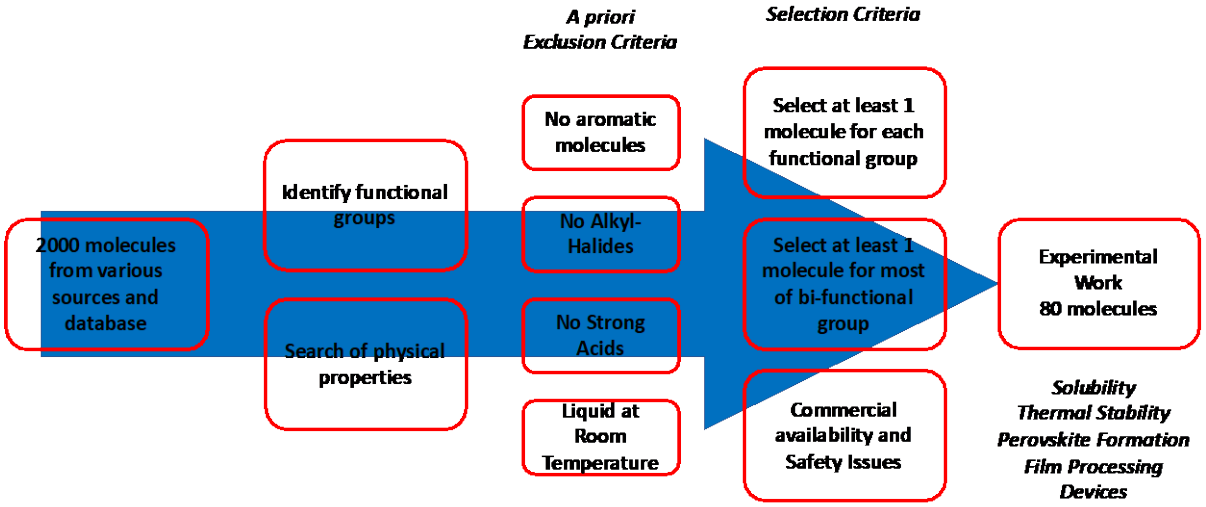

Figure A 1.1: Work scheme of solvents molecules selection, filtration, and testing.

Table A 1.1: Full list of the solvents investigated including the ability of the solvent to form a perovskite solution with a concentration above 1M, in addition to the functional group.

Name	CAS	Sol >1M	Functional group	Fun. group
N-methylformamide (NMF)	123-39-7	1	Amide	
Sulfolane	126-33-0	1	Sulfone	
N-Methylacetamide (NMAC)	79-16-3	1	Amide	
γ-Butyrolactone (GBL)	96-48-0	1	Ester	
2-Methoxyethanol (2ME)	109-86-4	1	Alcohol	Ether
Dimethylsulfoxide (DMSO)	67-68-5	1	Sulfoxide	
Trimethyl phosphate (TMP)	512-56-1	1	Phosphate	
N.N-Dimethylformamide (DMF)	68-12-2	1	Amide	
Tetramethylurea (TMU)	632-22-4	1	Diamide	
2-methoxyethylamine (2MEA)	109-85-3	1	Amine	Ether
1-Methyl-2-pyrrolidinone (NMP)	872-50-4	1	Amide	
N.N-Diethylformamide (DEF)	617-84-5	1	Amide	
Hexamethylphosphoramide (HMPA)	680-31-9	1	Phosphoramide	

3-methyl 2-oxazolidinone (3MOx)	19836-78-3	1	Carbamate	
N.N-Dimethylacetamide (DMAC)	127-19-5	1	Amide	
1.3-Dimethyl-2-imidazolidinone (DMI)	80-73-9	1	Diamide	
(DMPU)	7226-23-5	1	Diamide	
Cyrene	53716-82-8	0	Ether x2	Ketone
1.4-Diisocyanatobutane	4538-37-8	0	Isocyanate x2	
Methyl thioglicolate	2365-48-2	0	Ester	Thiol
Methyl trichloroacetate	96-34-4	0	Ester	Halide
Dimethyltrithiocarbonate	2314-48-9	0	Thiocarbonate	
H2O	7732-18-5	0	Water	
Ethylene glycol	107-21-1	0	Alcohol x2	
MeOH	67-56-1	0	Alcohol	
Triethylamine	121-44-8	0	Amine(3)	
ethanolamine	141-43-5	0	Alcohol	Amine(1)
Acetaldoxime	107-29-9	0	Oxime	
3-Hydroxypropionitrile	109-78-4	0	Alcohol	Nitrile
Dipropylamine	142-84-7	0	Amine(2)	
Propylene carbonate (PC)	108-32-7	0	Carbonate	
Diethyl sulfide	352-93-2	0	Sulfide	
Acetonitrile (ACN)	75-05-8	0	Nitrile	
N.N-Diethylhydroxylamine	3710-84-7	0	Hydroxylamine	
Trimethyl borate	121-43-7	0	Borate	
4-tert-Butylpyridine	3978-81-2	0	Heterocycle	
Propyl disulfide	629-19-6	0	Disulfide	
t-BUTYLISOCYANIDE	7188-38-7	0	Isonitrile	
IPA	67-63-0	0	Alcohol	
Glutaronitrile	544-13-8	0	Nitrile x2	
Thiophene	110-02-1	0	Thiophene	
1-Butanol	71-36-3	0	Alcohol	
Chloroform	67-66-3	0	Halide	
Pyruvic acid	127-17-3	0	Carboxilic Acid	Ketone
Ethylal	462-95-3	0	Acetal	

Methyl trifluoromethanesulfonate	333-27-7	0	Sulfonate	Halide
1-Butanethiol	109-79-5	0	Thiol	
Hydroxyacetone	116-09-6	0	Alcohol	Ketone
Dimethyl carbonate	616-38-6	0	Carbonate	
Ethyl Thiocyanate	542-90-5	0	Thiocyanate	
1.2-Dimethoxyethane	110-71-4	0	Ether x2	
S-Ethyl thioacetate	625-60-5	0	Thiolester	
Butylamine	109-73-9	0	Amine(1)	
2-methoxyethyl Acetate	110-49-6	0	Ether	Ester
Methoxyacetic acid	625-45-6	0	Carboxilic Acid	Ether
Methyl DL-lactate	547-64-8	0	Alcohol	Ester
3-Methoxypropionitrile	110-67-8	0	Ether	Nitrile
Methyl cyanoacetate	105-34-0	0	Ester	Nitrile
Cyclopentanone	120-92-3	0	Ketone	
Ethyl lactate	97-64-3	0	Alcohol	Ester
Tetrahydrofuran	109-99-9	0	Ether	
Acetylacetone	123-54-6	0	Ketone x2	
Isoxazole	288-14-2	0	Azole	
Dimethyl Sulfite	616-42-2	0	Sulfite	
1.3-diaminopropane	109-76-2	0	Amine(1) x2	
N.N-Dimethylthioformamide	758-16-7	0	Thioamide	
Dimethyl Malonate	108-59-8	0	Ester x2	
Ethyl cyanoacetate	105-56-6	0	Ester	Nitrile
1.2-Ethanedithiol	540-63-6	0	Thiol x2	
n-methylpyrrolidone-2-thione	10441-57-3	0	Thioamide	
2-methylpyrazine	109-08-0	0	Heterocycle	
Methyl acetoacetate	105-45-3	0	Ester	Ketone
methyl phenyl sulfoxide	1193-82-4	-1	Sulfoxide	
2-methylthioethanol	5271-38-5	-1	Thioether	Alcohol
Di-n-butyl sulfoxide	2168-93-6	-1	Sulfoxide	
Tetramethylene sulfoxide	1600-44-8	-1	Sulfoxide	

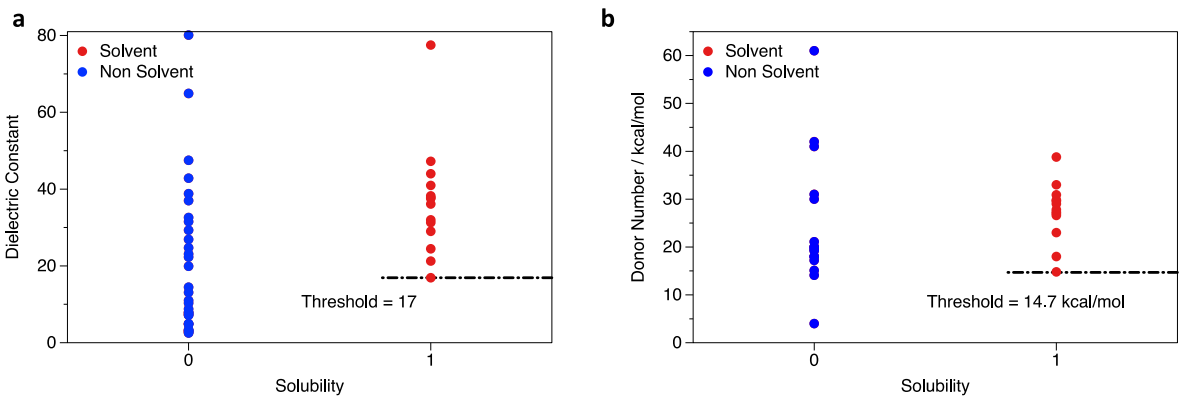

Figure A 1.2: Correlation between solubility and **a)** dielectric constant (bottom graph) and **b)** donor number (D_N in kcal/mol, top graph) of the solvents tested.

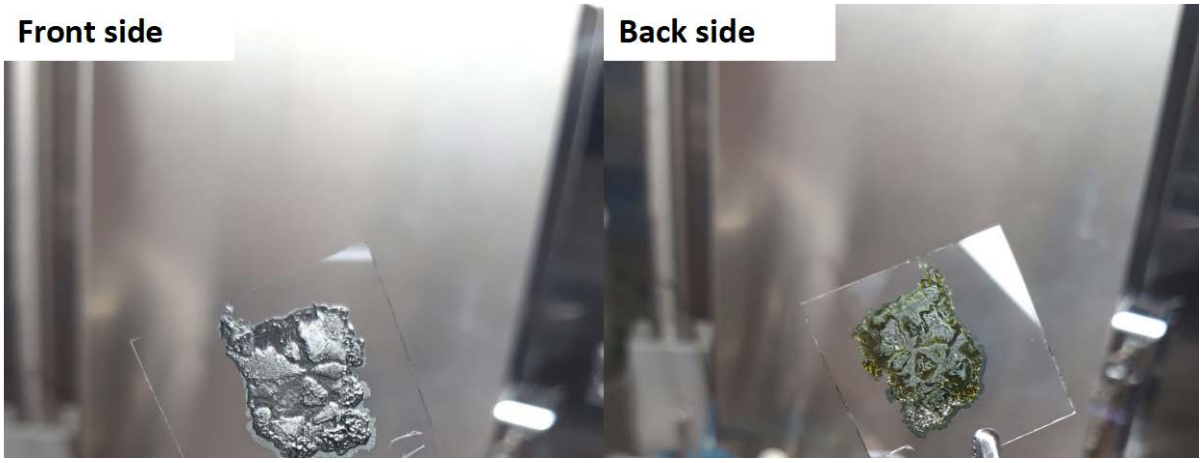

Figure A1.3: Images of drop casted 3MOx after annealing. The yellow residues on the right side could be not completely dried solvent.

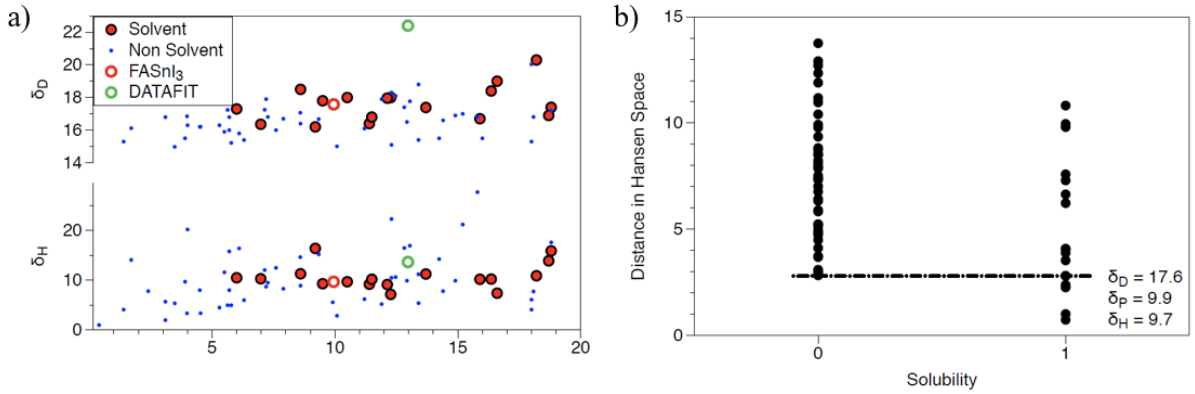

Figure A1.4: a) Hansen parameters of $FASnI_3$ relative to the other solvents. b) the relationship between the distance in Hansen space and the solubility.

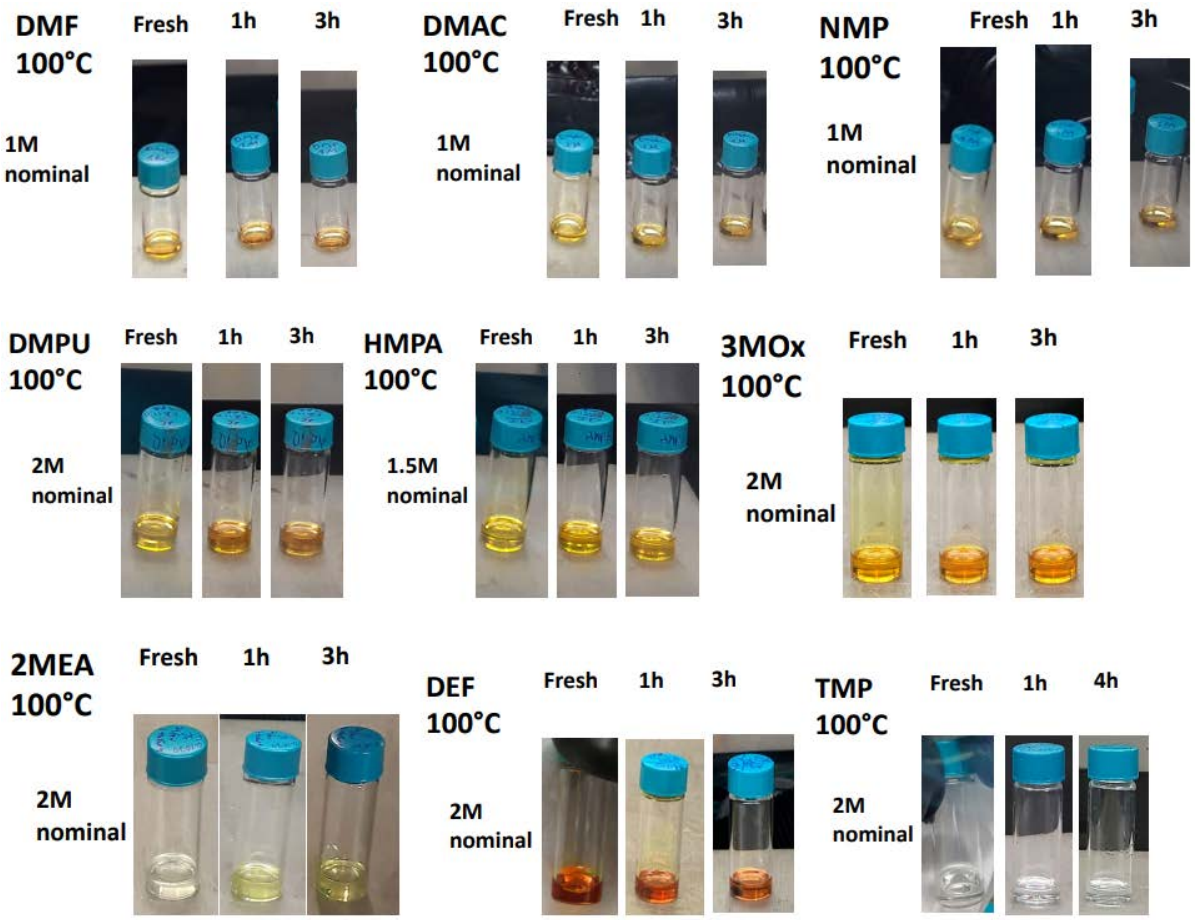

Figure A1.5: Thermal stress of the solutions of $FASnI_3$ at 100°C evaluated by photographs of the solutions.

Figure A1.6: different crystallization forms of different solvents

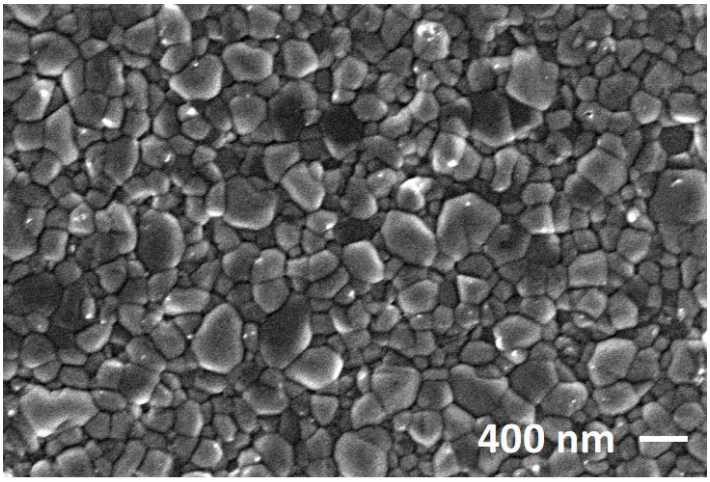

Figure A 1.7: SEM image of $FASnI_3$ deposited from DMF.

10.2 A2 Supporting Information: Chapter 6

Computational details

The geometrical structure of all studied complexes and their molecular constituents (the separated molecules of SnI2, tBP, DMI, DMF, and DMSO) was fully optimized at the DFT level of theory. The BP-D dispersion-corrected density functional was combined with the aug-cc-pVTZ-PP (for the atoms of SnI2) and aug-cc-pVTZ (for the remaining atoms) basis sets. Bulk solvent effects on the geometrical structure and energy were evaluated using the SMD implicit solvation model. Harmonic vibrational frequency calculations were performed at the BP-D/aug-cc-pVTZ(-PP) level to verify that the optimized geometries corresponded to (local) minima on the 3N-6 dimensional potential energy surface. The formation of each complex was characterized by its complexation energy ($E_{complex}$):

$$E_{complex} = E_{int,tot} + E_{def} + \Delta ZPVE$$

where $E_{int,tot}$ is the total interaction between the molecular fragments of the complex, E_{def} is the energy consumed by the geometrical deformation from the separated molecules to the corresponding molecular fragments of the complex, and $\Delta ZPVE$ denotes the difference between the zero-point vibrational energies of the complex and its separated molecular constituents. The $E_{complex}$ energy was calculated at the BP-D/aug-cc-pVTZ(-PP) level. Additionally, the interaction energy (E_{int}) for each SnI2-solvent pair in the complexes was also obtained from single-point SCS-MP2/aug-cc-pVTZ(-PP) calculations. All calculations were carried out using the Gaussian 16 C.01 program.

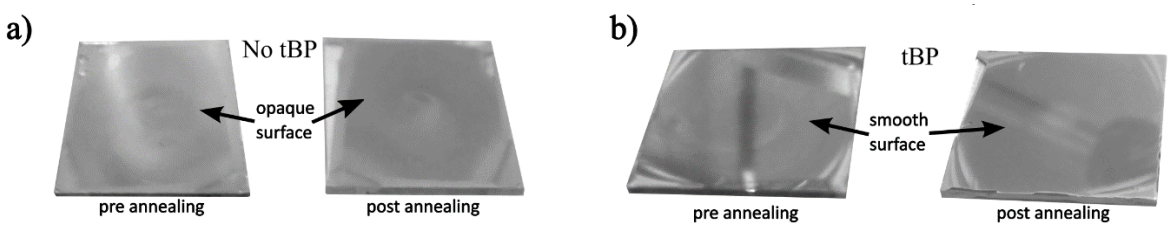

Figure A2.1: opaque and smooth morphologies obtained with a) and without b) tBP.

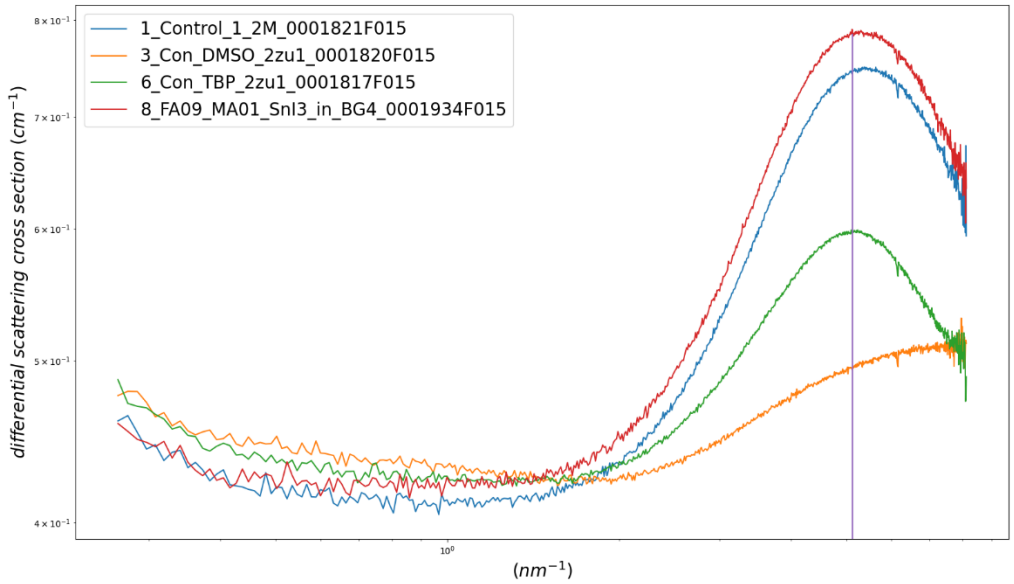

Figure A2.2: Small Angle X-Ray Scattering curves of four distinguished solution samples measured at room temperature are shown. THP (8, red) is shown with respect to the control solution 1, blue. The second pair are THP in TBP and DMSO solutions (curves 6, green and 3, dark yellow). A vertical line is shown as guide for the eyes around the maxima of the scattering curves.

Table A2.1: Geometrical (d, in ppm) and energetic ($E_{complex}$, E_{int}, in kJ mol^{-1}) parameters for the 1:1 and 1:2 complexes in their preferred isomers in DMF solution. E_{int} calculated at the SCS-MP2/aug-cc-pVTZ(-PP) level of theory

Complex	Parameter		
	d	$E_{complex}$	E_{int}
SnI_2:TBP	232.2	-108.2	-121.1
SnI_2:DMSO	222.5	-101.3	-136.0
SnI_2:DMI	223.6	-96.1	-116.0
SnI_2:DMF	225.3	-85.1	-120.0
SnI_2:2TBP	232.8	-163.5	-149.5
SnI_2:2DMSO	244.1	-153.6	-126.3
SnI_2:2DMI	247.2	-147.5	-97.5
SnI_2:2DMF	246.5	-128.0	-109.9

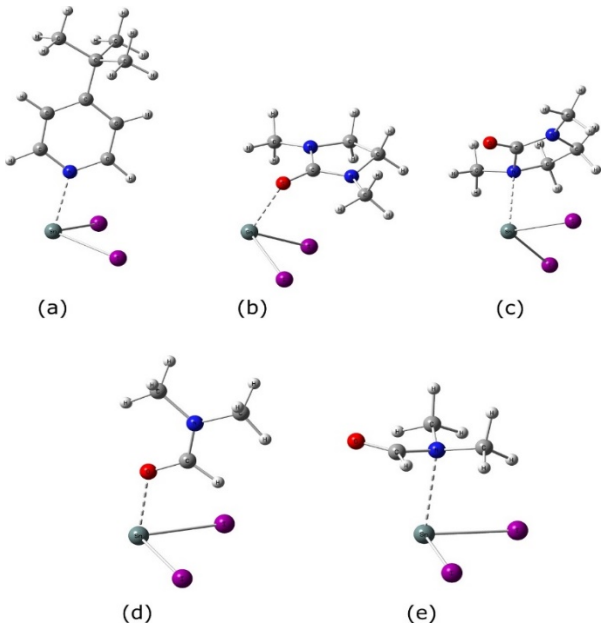

Figure A2.2. The geometries optimized in DMF solution for (a) SnI_2:TBP, (b) SnI_2:DMI formed via the Sn←O coordination bond, (c) SnI_2:DMI via Sn←N, (d) SnI_2:DMF via Sn←O, and (e) SnI_2:DMI via

Sn←N. The colors coding individual elements are the same for all four complexes. The Sn←donor coordination bonds are denoted with a dashed line.

Table A2.3. Geometrical and energetic parameters for three 1:1 complexes in DMF solution. Values of the parameters for the complexes in DMSO solution and in gas phase are given in parentheses and square brackets, respectively. [a]

Parameter	Complex/coordination				
	SnI_2:TBP	SnI_2:DMI		SnI_2:DMF	
	Sn←N	Sn←O	Sn←N	Sn←O	Sn←N
d(Sn←donor)	232.2 (232.1) [239.3]	223.6 (223.6) [229.0]	251.0 (250.9) [257.1]	225.3 (225.2) [232.6]	276.6 (265.8) [280.5]
d(Sn–I)	288.3 (288.4) [282.7]	289.5 (289.6) [284.5]	286.5 (286.5) [282.3]	288.8 (289.0) [283.6]	283.9;284.5 (283.8;285.6) [279.8;280.4]
a(I–Sn–I)	95.7 (95.6) 100.7	95.3 (95.1) [98.9]	96.7 (96.2) [99.7]	95.1 (95.0) [97.4]	97.0 (96.8) [99.5]
$E_{complex}$	-108.2 (-109.4) [-108.7]	-96.1 (-96.3) [-110.5]	-87.0 (-88.2) [-96.3]	-85.1 (-85.0) [-92.5]	-49.8 (-50.3) [-57.4]
$E_{int,tot}$ [b]	-131.9 (-142.3) [-120.9]	-132.0 (-140.4) [-133.6]	-113.7 (-120.7) [-115.2]	-124.0 (-131.2) [-108.0]	-72.5 (-82.9) [-71.5]
$E_{int,tot}$ [c]	-121.1 (-127.9) [-109.1]	-116.0 (-120.9) [-120.4]	-89.5 (-93.9) [-94.6]	-120.0 (-124.2) [-106.5]	-52.2 (-65.1) [-52.7]

[a] Distances (*d*) are given in pm, angles (*a*) in degrees, energies ($E_{complex}$, $E_{int,tot}$) in kJ mol^{-1}.

[b] Energies calculated at the BP-D/aug-cc-pVTZ(-PP) level of theory.

[c] Energies calculated at the SCS-MP2/aug-cc-pVTZ(-PP) level of theory.

Table A2.4. Geometrical parameters for SnI_2 in DMF solution. Values of the parameters for SnI_2 in DMSO solution and in gas phase are given in parentheses and square brackets, respectively. [a]

Parameter	Value
d(Sn–I)	281.4 - (281.4) - [276.2]
a(I–Sn–I)	97.5 - (97.3) - [100.4]

[a] Distance (*d*) is given in pm, angle (*a*) is expressed in degrees.

Table A2.5. Selected parameters of the isomers found for SnI_2:2TBP in DMF solution. [a]

Isomer [b]	Parameter		
	d(Sn←donor)	*a*(I–Sn–I)	$E_{complex}$
N_{eq}→Sn←N_{eq}	232.8	167.3	-163.5
N_{ax}→Sn←N_{ax}	255.2	97.5	-158.7

[a] Distance (*d*) is given in pm, angle (*a*) in degrees, energy ($E_{complex}$) in kJ mol^{-1}.

[b] The equatorial and axial positions occupied by the TBP molecules in the complex are denoted by N_{eq} and N_{ax}, respectively.

Table A2.6. Selected parameters of the isomers found for SnI_2:2DMI in DMF solution. [a]

Isomer [b]	Parameter		
	d(Sn←donor)	*a*(I–Sn–I)	$E_{complex}$
O_{ax}→Sn←O_{ax}	247.2	94.7	-147.5
O_{eq}→Sn←O_{eq}	223.0	164.3	-133.6

[a] Distance (*d*) is given in pm, angle (*a*) in degrees, energy ($E_{complex}$) in kJ mol^{-1}.

[b] The equatorial and axial positions occupied by the DMI molecules in the complex are denoted by the subscripts ‘eq’ and ‘ax’, respectively.

Table A2.7. Selected parameters of the isomers found for SnI_2:2DMF in DMF solution. [a]

Isomer [b]	Parameter		
	d(Sn←donor)	*a*(I–Sn–I)	$E_{complex}$
O_{ax}→Sn←O_{ax}	246.5	95.4	-128.0
O_{ax}→Sn←N_{ax}	227.8;316.4	96.0	-116.2
N_{ax}→Sn←N_{ax}	282.5;283.4	97.1	-86.7
O_{ax}→Sn←N_{eq}	250.7;272.6	92.5	-79.7
N_{ax}→Sn←N_{eq}	339.1;284.2	96.1	-76.8

[a] Distance (*d*) is given in pm, angle (*a*) in degrees, energy ($E_{complex}$) in kJ mol^{-1}.

[b] The equatorial and axial positions occupied by the DMF molecules in the complex are denoted by the subscripts ‘eq’ and ‘ax’, respectively.

Table A2.8. Geometrical and energetic parameters for three 1:2 complexes in their preferred isomers in DMF solution. Values of the parameters for the complexes in DMSO solution and in gas phase are given in parentheses and square brackets, respectively. [a]

Parameter	SnI_2:2TBP	SnI_2:2DMI	SnI_2:2DMF
d(Sn←donor)	232.8 - (232.7) -[257.4]	247.2- (247.3) - [249.4]	246.5 - (246.7) - [249.3]
d(Sn–I)	313.4;314.6 - (313.4;314.6) - [285.6]	292.2 - (292.2) - [289.1]	292.4 - (292.4) - [289.6]
a(I–Sn–I)	167.3 - (167.1) - [99.0]	94.7 - (95.2) - [97.8]	95.4 - (95.3) - [95.8]
$E_{complex}$	-163.5 - (-165.7) - [-170.3]	-147.5 - (-148.3) - [-183.3]	-128.0 - (-128.1) - [-155.2]
$E_{int,tot}$ [b]	-298.2 - (-321.0) - [-183.9]	-184.8 - (-204.2) - [-223.4]	-189.8 - (-205.6) - [-188.0]
E_{int} [b]	-156.3 - (-167.8) - [-110.1]	-114.4 - (-123.7) - [-127.8]	-115.8 - (-123.5) - [-107.5]
$E_{int,tot}$ [c]	-283.3 - (-307.5) - [-164.5]	-147.5 - (-162.9) - [-182.2]	-173.4 - (-185.6) - [-164.5]
E_{int} [c]	-149.5 - (-161.2) - [-102.0]	-97.5 - (-104.1) - [-110.5]	-109.9 - (-115.8) - [-99.4]

[a] Distances (*d*) are given in pm, angles (*a*) in degrees, energies ($E_{complex}$, $E_{int,tot}$) in kJ mol^{-1}.

[b] Energies calculated at the BP-D/aug-cc-pVTZ(-PP) level of theory.

[c] Energies calculated at the SCS-MP2/aug-cc-pVTZ(-PP) level of theory.

10.3 A3 Supporting Information: Chapter 7

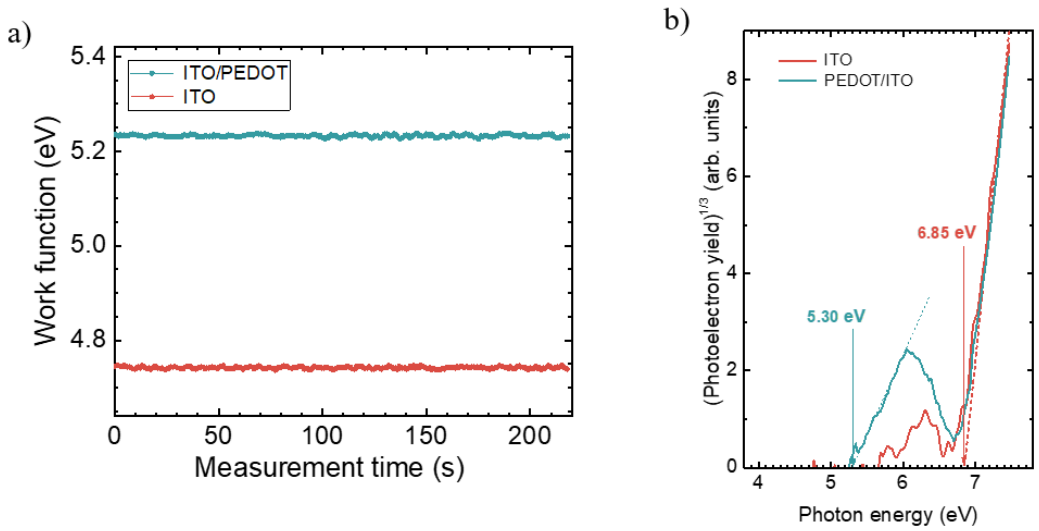

Figure A3.1: Work function (left) and ionization energy (right) measurements of ITO on a glass substrate and PEDOT spincoated over ITO using KP and PYS respectively.

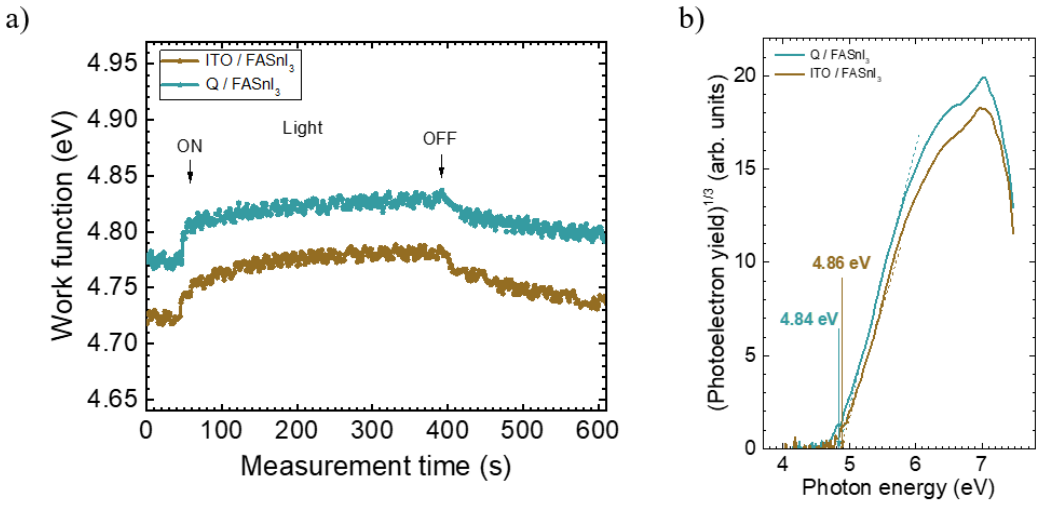

Figure A3.2: The work function (left) and the ionization energy (right) of $FASnI_3$ deposited on top of different substrates Quartz, ITO and PEDOT. This illustrates the effect of the bottom substrate on the energetics of the absorber film and hence the band alignment and charges extraction.

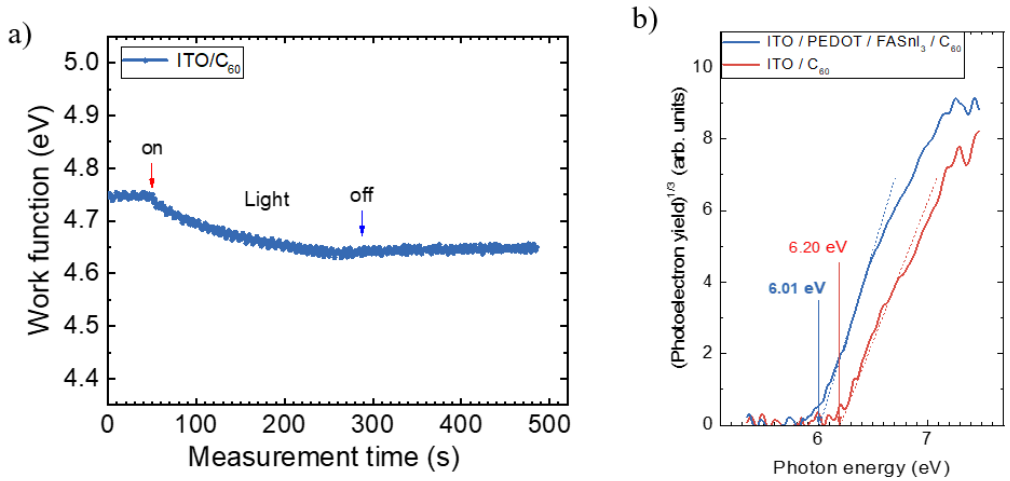

Figure A3.3: work function measurement (left) and ionization energy (right) of C60 deposited on top of ITO.

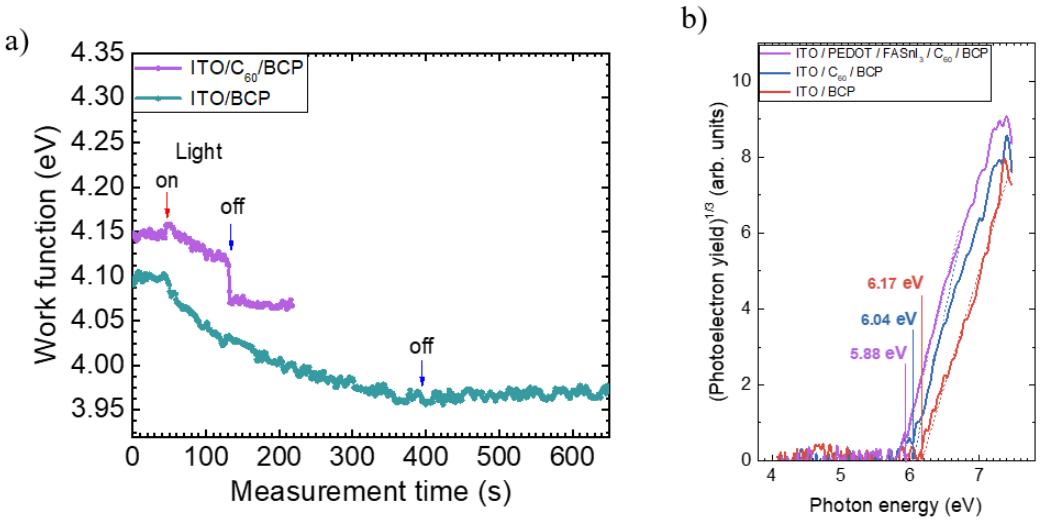

Figure A3.4: The work function (left) and the ionization energy (right) of BCP deposited on top of different substrates ITO and C_{60} and even in a full device stack. This show the major difference in the position of energy bands of BCP when functioned in different stacks.

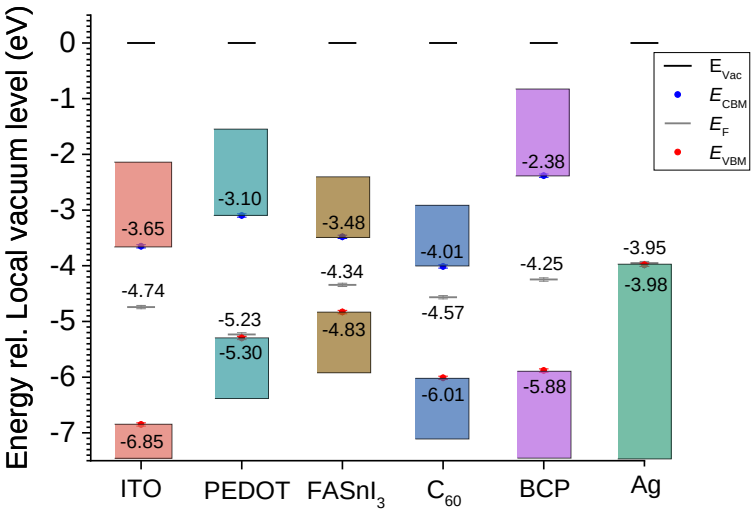

Figure A3.5: The energy band diagram with respect to the Vacuum level (E_v) was plotted based on the values generated by the KP-PYS technique.

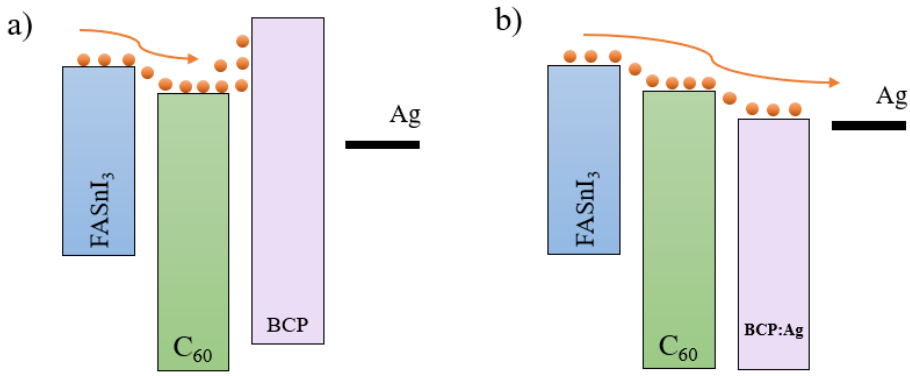

Figure A3.6: Graphical illustration of the electron extraction mechanisms. a) the common understanding of the BCP/Ag interface energetics. b) The energetics of the BCP7Ag interface based on our measurement in which the early evaporated nanometers blend with Ag which forms an intermediate energy level of around 4 eV that enables high cabability of electron extraction.

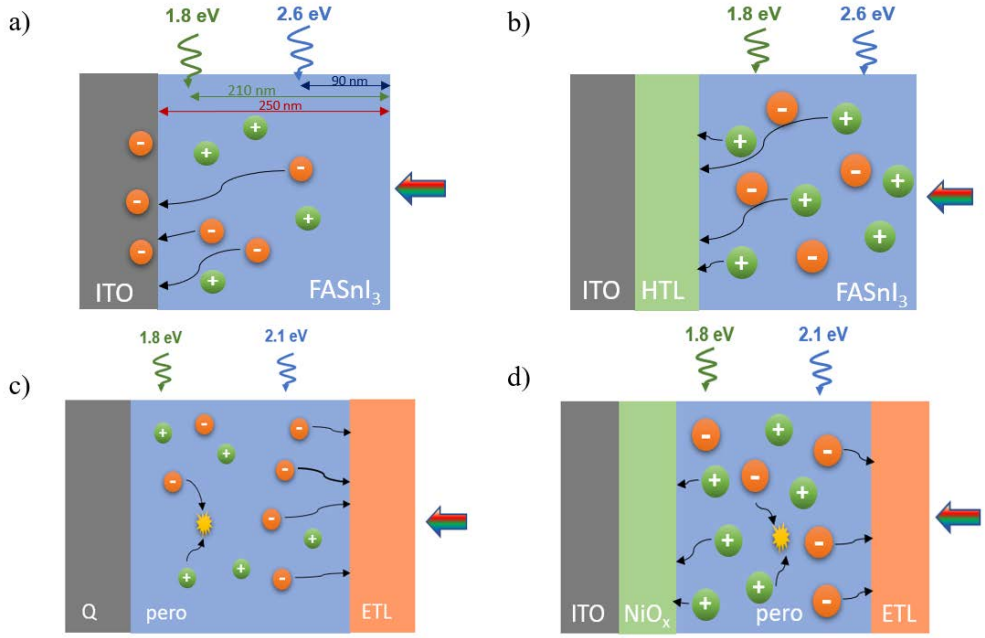

Figure A3.7: Illustrative diagrams of charges extraction dynamics at different excitation energies and device structures. Notably, we used two excitation energies, 688 nm (1.8 eV) which penetrates up to 210 nm, and 486 (2.6 eV) penetrating up to 90 nm into a 250 nm thick $FASnI_3$. a) ITO/$FASnI_3$ interface. b) HTL (PEDOT or NiOx)/$FASnI_3$ interface. c) $FASnI_3$/ETLs (C_{60}, BCPM, and ICPA) interface. d) a full device stack illuminated from the top side.

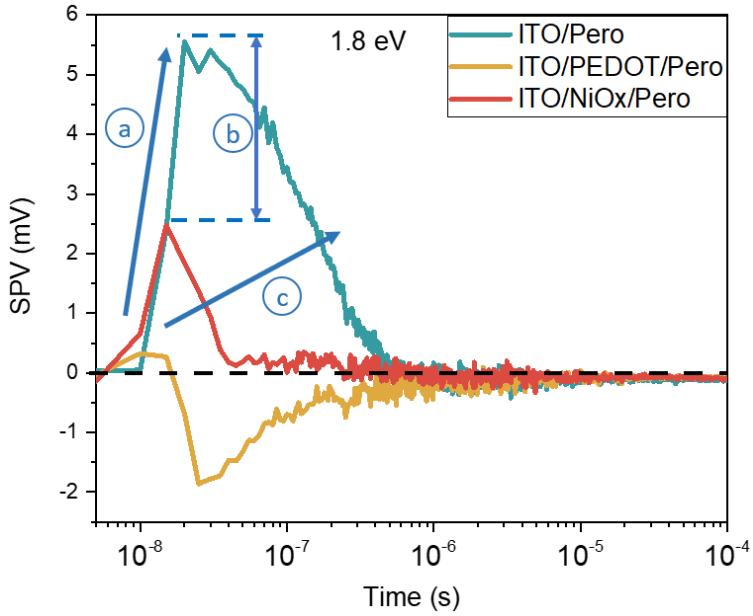

Figure A 3.8: Illustrative explanation of the tr-SPV signal. a) the intial slope corresponds to the charge extraction rate. b) Signal height which indicates the volume of the extracted charges i.e., the higher the sample, the more the extracted charges. c) The plateau time corresponds to the recombination rate, i.e., the wider the plateau, the longer the time and the slower the recombination rate of the extracted charges.

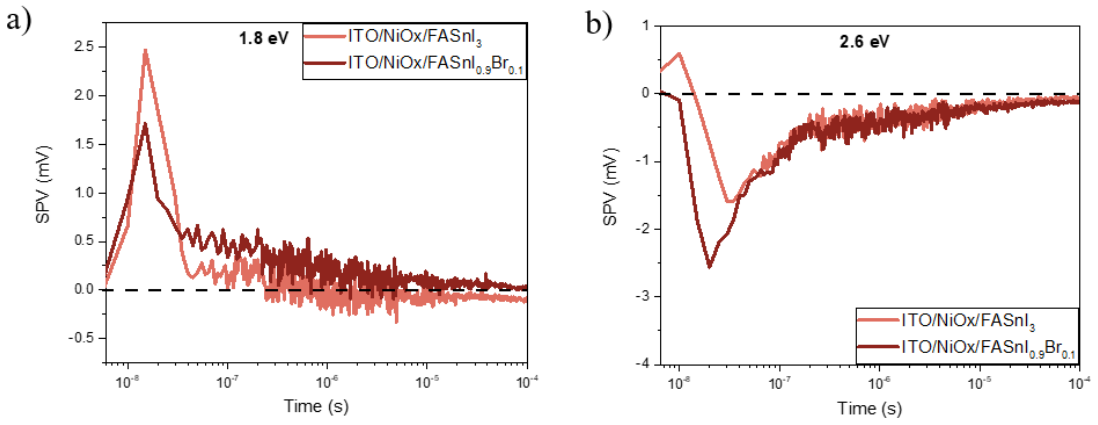

Figure A 3.9: tr-SPV measurements of $FASnI_3$ and $FASnI_{0.9}Br_{0.1}$ deposited on top of NiOx, the addition of 10% $SnBr_2$ deepens the position of HOMO level which enhances band alignment. a) excitation near the interface, we observe a clear reduction in electron trapping when the energy bands are better aligned. b) Excitation in the bulk of the absorber film, we observe a better charge extraction.

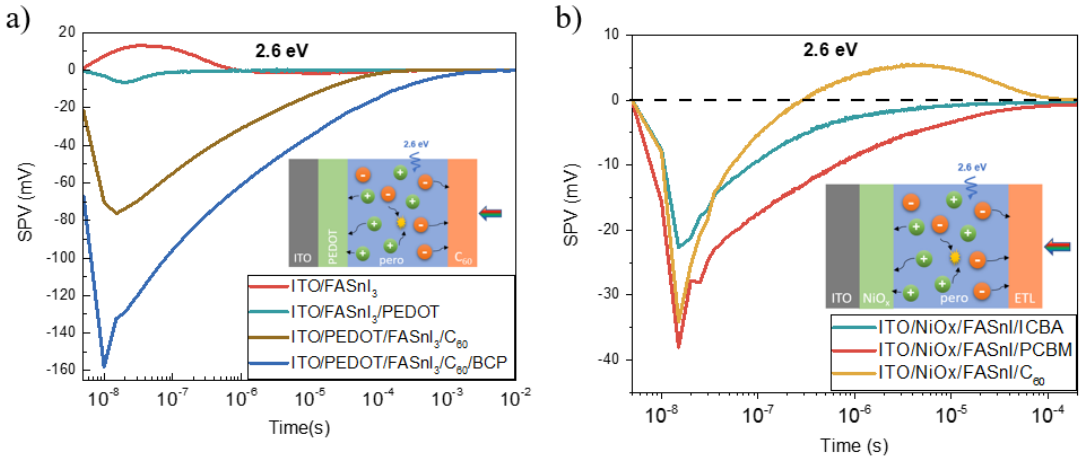

Figure A3.10: tr-SPV measurements of $FASnI_3$ and $FASnI_{0.9}Br_{0.1}$ deposited on top of NiOx, the addition of 10% $SnBr_2$ deepens the position of HOMO level which enhances band alignment. a) excitation near the interface, we observe a clear reduction in electron trapping when the energy bands are better aligned. b) Excitation in the bulk of the absorber film, we observe a better charge extraction.

Wrong inset (change it)

Note A3.1: Electron extraction dynamics in sandwiched $FASnI_3$ between NiOx and different ETLs

To deeply understand electron extract dynamics in tin perovskites, we prepared $FASnI_3$ films sandwitched between ETLs and HTLs together. Such stacks enable us to study the mutual effect between ETLs and HTLs, moreover, its very close to the real operation conditions of the full device stack where electrons and holes are extracted together at the same time. **In Figure SI10**, we prepared the same device stack one based on PEDOT as HTL and the other is based on NiO_x. In the case of PEDOT, we followed the evolution of the tr-SPV signal by measuring the device stack layer by layer, however in the NiO_x case, we measured different ETLs to check their effect on charge extraction when the HTL layer is inserted. By comparing the signal amplitude of the two stacks ITO/PEDOT/$FASnI_3$/C_{60} and ITO/NiO_X/$FASnI_3$/C_{60}, we find that in the PEDOT case, we extract more than double the charges extracted in the case of NiO_x. Furthermore, we observe much slower recombination dynamics in the case of PEDOT (10 ms) compared to NiOx (28 µs). Conclusively, the efficiency of the HTL in extraction holes affects electron extraction significantly, as it decreases holes density in the absorber material and in turn the recombination probability. **Figure SI 10a** shows a big jump in electron extraction after BCP was inserted, which agrees with the KP SPV signal showd in **Figure 1e**, both measurements confirms the vital role of BCP in electron extraction as we illustrated earlier. **Figure SI 10b** shows the electron extraction with NiOx and different ETLs, it has almost the same trend without HTL as shown in **Figures 3 c-d**. However, C_{60} shows even faster recombination dynamics leading to a positive pump which has a miximum amplitude of around 6 mV at 5 µs. This could be attributed to the electrons trapping at the $FASnI_3$/NiOx layer, which retards the charges recombination across the $FASnI_3$ film at the beginning, then leaves holes as the majority of charges in the perovskite film, which is recorded in the measurement as a positive signal then electrons are slowly released and recombine with holes. In addition, this positive signal appears only with C_{60} compared to other ETLs due to its higher charge mobility. As a result, C_{60} releases electrons faster than PCBM and ICBA, i.e., extracted electrons in C_{60} are released and recombined before the trapped electrons in the NiOx are released, as illustrated in **Figure SI 11**.

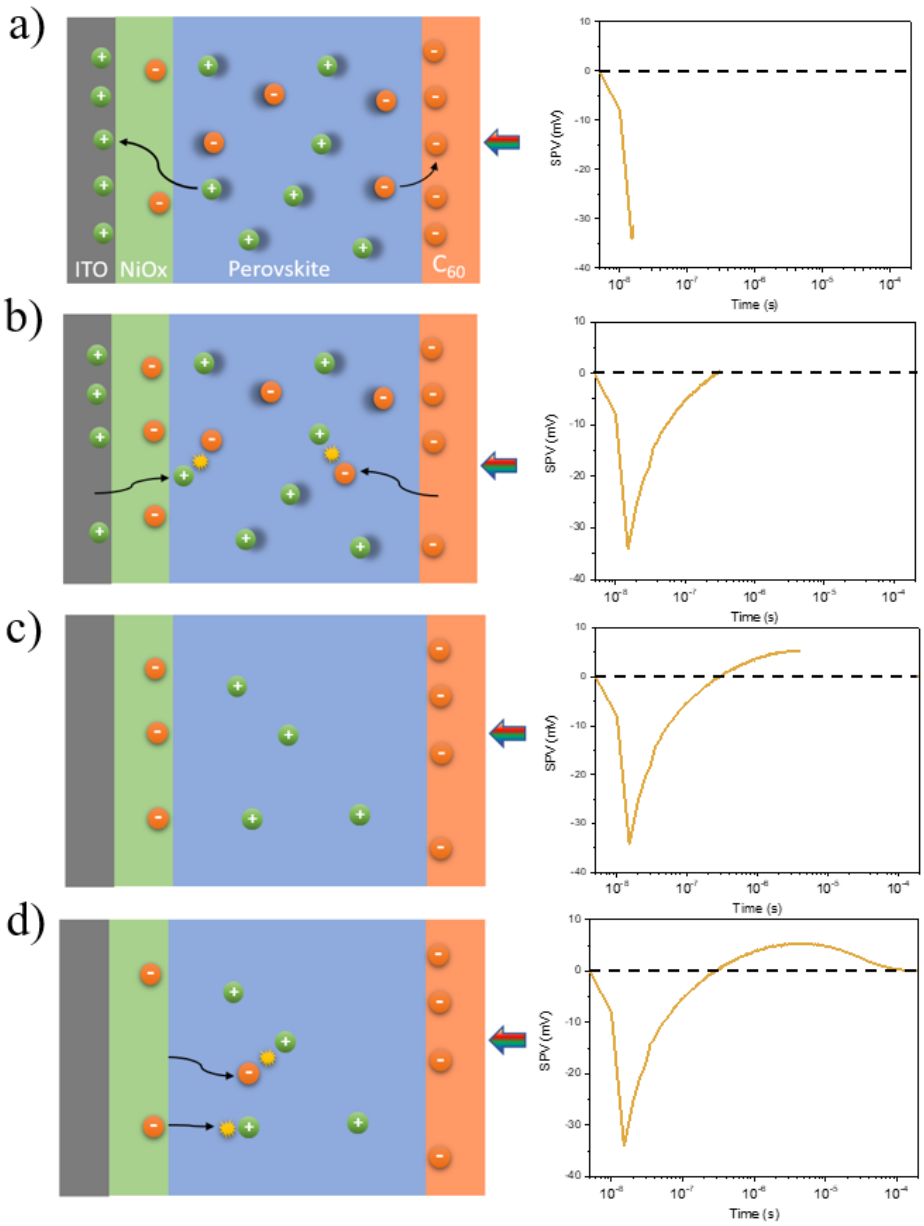

Figure A3.11: Graphical illustrations of the charge carrier dynamics of the device stack NiOx/$FASnI_3$/C_{60}. a) electrons are trapped at the NiOx/$FASnI_3$ interface up on excitation. b) Holes are travelling to recombine in the bulk of the absorber material. c) Holes are the majority in the bulk of the absorber because electrons are trapped in the NiOx which leads to the appearance of the positive SPV signal. d) Finally, trapped electrons are released and recombine with holes.

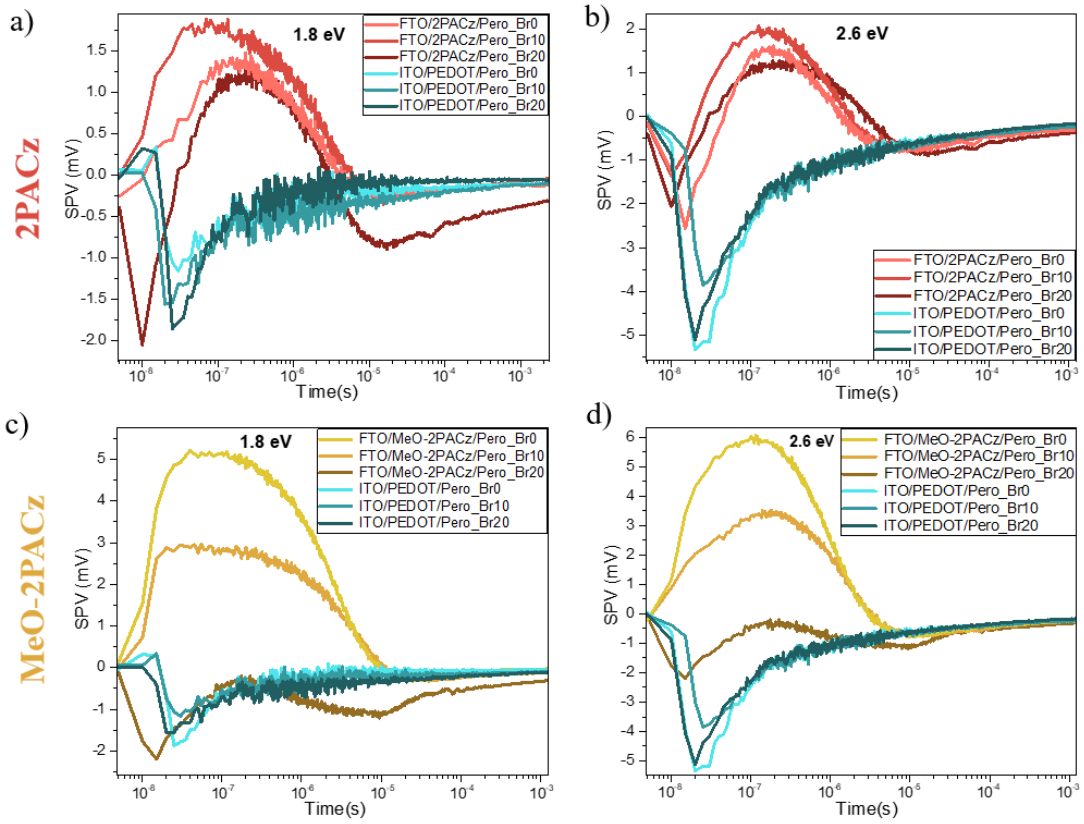

Figure A3.12: tr-SPV signals of $FASnI_3$ deposited on top of MeO-2PACz and 2PACz compared to PEDOT. a and c) excitation using 688 nm laser pulse (1.8 eV) which penetrates deep in the film and excites electrons near from the buried interface. b and d) Excitation using 486 nm laser pulse (2.6 eV) which excites electrons in the bulk of the perovskite film.

10.4 A7 Publications and Conference Contributions

Peer-reviewed publications

1- Aktas, E., Rajamanickam, N., Pascual, J., Hu, S., Aldamasy, M. H., Di Girolamo, D., … Abate, A. (2022). Challenges and strategies toward long-term stability of lead-free tin-based perovskite solar cells. Communications Materials 2022.
2- Aldamasy, M., Iqbal, Z., Li, G., Pascual, J., Alharthi, F., Abate, A., & Li, M. (2021). Challenges in tin perovskite solar cells. Physical Chemistry Chemical Physics.
3- Chen, G., Li, P., Xue, T., Su, Aldamasy,M., Zhang, Y., … Song, Y. (2021). Design of Low Bandgap CsPb1−xSnxI2Br Perovskite Solar Cells with Excellent Phase Stability. Small.
4- Dai, T., Cao, Q., Yang, L., Aldamasy, M. H., Li, M., Liang, Q., … Xu, G. (2021). crystals Strategies for High-Performance Large-Area Perovskite Solar Cells toward Commercialization.
5- Di Girolamo, D., Blundo, E., Folpini, G., Ponti, C., Li, G., Aldamasy, M. H., … Abate, A. (2022). Energy Distribution in Tin Halide Perovskite. Solar RRL.
6- Di Girolamo, D., Pascual, J., Aldamasy, M. H., Iqbal, Z., Li, G., Radicchi, E., … Abate, A. (2021). Solvents for Processing Stable Tin Halide Perovskites. ACS Energy Letters.
7- Girolamo, D. Di, Pascual, J., Aldamasy, M. H., Iqbal, Z., Li, G., Radicchi, E., … Abate, A. (2021). Solvents for Processing Stable Tin Halide Perovskites. ACS Energy Letters, 6(3), 959–968.
8- Jacobsson, T. J., Hultqvist, A., García-Fernández, A., Anand, A., Al-Ashouri, A., Hagfeldt, A., …Aldamasy, M., Unger, E. (2021b). An open-access database and analysis tool for perovskite solar cells based on the FAIR data principles. Nature Energy 2021.
9- Jorge Pascual, Giuseppe Nasti, H. Aldamasy, M., A. Smith, J., Marion Flatken, Nga Phung, … Antonio Abate. (2020). Origin of Sn(ii) oxidation in tin halide perovskites. Materials Advances.
10- Li, G., Su, Z., Canil, L., Hughes, D., Aldamasy, M. H., Dagar, J., … Abate, A. (2023). Highly efficient p-i-n perovskite solar cells that endure temperature variations. Science.
11- Li, G., Su, Z., Li, M., Yang, F., Aldamasy, M. H., Pascual, J., … Abate, A. (2021). Ionic Liquid Stabilizing High-Efficiency Tin Halide Perovskite Solar Cells. Advanced Energy Materials.
12- Li, M., Li, M., Aldamasy, M., … Abate, A. (2020a). Tin Halide Perovskite Films Made of Highly Oriented 2D Crystals Enable More Efficient and Stable Lead-free Perovskite Solar Cells. ACS Energy Letters.
13- Mahmoud Aldamasy, Zafar Iqbal, Guixiang Li, Jorge Pascual, Fahad Alharthi, Antonio Abate, & Meng Li. (2021). Challenges in tin perovskite solar cells. Physical Chemistry Chemical Physics.
14- Nasti, G., Aldamasy, M. H., Flatken, M. A., Musto, P., Matczak, P., Dallmann, A., … Abate, A. (2022). Pyridine Controlled Tin Perovskite Crystallization. ACS Energy Letters.
15- Niu, Y.-C., Yang, L.-F., Aldamasy, M. H., Li, M., Lan, W.-J., Xu, Q., … Yang, Y.-G. (2021). Efficient application of carbon-based nanomaterials for high-performance perovskite solar cells. Rare Metals 2021.
16- Pascual, J., Di Girolamo, D., Flatken, M. A., Aldamasy, M. H., Li, G., Li, M., & Abate, A. (2022b). Lights and Shadows of DMSO as Solvent for Tin Halide Perovskites. Chemistry – A European Journal.

17- Pascual, J., Flatken, M., Félix, R., Li, G., Turren-Cruz, S.-H., Aldamasy, M. H., … Abate, A. (2021). Fluoride Chemistry in Tin Halide Perovskites. Angewandte Chemie International Edition.
18- Pascual, J., Nasti, G., Aldamasy, M. H., Smith, J. A., Flatken, M., Phung, N., … Abate, A. (2020). Origin of Sn(II) oxidation in tin halide perovskites. Materials Advances, 1(5), 1066–1070.
19- Yan, J., Li, H., Aldamasy, M. H., Frasca, C., Abate, A., Zhao, K., & Hu, Y. (2023). Advances in the Synthesis of Halide Perovskite Single Crystals for Optoelectronic Applications. Chemistry of Materials.
20- Yang, J., He, T., Li, M., Li, Guixiang., Aldamasy, M., Xu, J., … Abate, A. (2022). π-Conjugated Carbazole Cations Enable Wet-Stable Quasi-2D Perovskite Photovoltaics. ACS Energy Letters.
21- Zhang, Z., Liu, H., Tang, Y., Aldamasy, M. H., Yang, F., Yang, J., … Li, Z. (2022). Organic compound passivation for perovskite solar cells with improving stability and photoelectric performance. Solar Energy.

A8 Declaration of Originality

I here declare that this dissertation is from the author´s original works, except the parts which give rightful references to other people´s works, and that this dissertation has not been submitted to any other university in Germany or abroad.

Potsdam, August 2023

Mahmoud Hussein

A9 Acknowledgments